ADVANCES IN GEOPHYSICS, VOL. 51, CHAPTER 3

PHENOMENOLOGY OF TSUNAMIS: STATISTICAL PROPERTIES FROM GENERATION TO RUNUP

ERIC L. GEIST [1]

ABSTRACT

Observations related to tsunami generation, propagation, and runup are reviewed and described in a phenomenological framework. In the three coastal regimes considered (near-field broadside, near-field oblique, and far field), the observed maximum wave amplitude is associated with different parts of the tsunami wavefield. The maximum amplitude in the near-field broadside regime is most often associated with the direct arrival from the source, whereas in the near-field oblique regime, the maximum amplitude is most often associated with the propagation of edge waves. In the far field, the maximum amplitude is most often caused by the interaction of the tsunami coda that develops during basin-wide propagation and the nearshore response, including the excitation of edge waves, shelf modes, and resonance. Statistical distributions that describe tsunami observations are also reviewed, both in terms of spatial distributions, such as coseismic slip on the fault plane and near-field runup, and temporal distributions, such as wave amplitudes in the far field. In each case, fundamental theories of tsunami physics are heuristically used to explain the observations.

KEYWORDS: Tsunami, Earthquake, Landslide, Phenomenology, Statistical, Runup, Tide gage.

1. INTRODUCTION

Major tsunamis are often accompanied by some aspect of unexpected behavior, relative to a simple deterministic understanding of tsunami physics. Typically, the unexpected behavior is related to the amplitude, runup, and timing of the largest wave when a tsunami strikes the coast. Kanamori (1972) first classified earthquakes that result in tsunamis with greater than expected overall severity relative to earthquake magnitude as "tsunami earthquakes", examining specifically the highly destructive tsunamis emanating from the 1896 Sanriku and 1946 Aleutian earthquakes. Other examples of tsunami earthquakes that generated unexpectedly severe and devastating tsunamis relative to the magnitude of the generating earthquake include the 1992 Nicaragua event (Kanamori and Kikuchi, 1993) and the 1994 and 2006 Java events (Abercrombie *et al.*, 2001; Polet and Thio, 2003; Ammon *et al.*, 2006). It has been argued that a portion of the 2004 Sumatra-Andaman earthquake also had behavior similar to tsunami earthquakes (Seno and Hirata, 2007). Not only can the overall severity be unexpectedly large, but the runup along isolated portions of the coast can be unexpectedly large relative to the overall runup associated with the tsunami. Such a case occurred with

[1] Author thanks e-mail: egeist@usgs.gov

ISSN: 0065-2687
DOI: 10.1016/S0065-2687(09)05108-5

the 1993 Hokkaido tsunami having $M_w = 7.6$ (Mendoza and Fukuyama, 1996), in which a maximum runup value of 31.7 m was measured at a small valley that opens to a pocket beach (Shuto and Matsutomi, 1995), owing to local focusing of the wave by the nearshore bathymetry. Local high runup values can also be associated with strong variability in the source processes, as in the case for runup along the western Aceh coastline associated with the 2004 Sumatra-Andaman earthquake (Hirata *et al.*, 2006; Fujii and Satake, 2007). Another type of unexpected behavior when the coastal hydrodynamic response is not taken into account is a delay in the expected timing of the maximum runup arrival. Crescent City, California is particularly prone to large tsunami arrivals occurring hours after the first arrival (Dengler *et al.*, 2009). Earlier than expected tsunami arrivals have also been reported, as is the case for the 1983 Japan Sea tsunami (Shuto *et al.*, 1995).

In an attempt to understand tsunamis better in terms of their observed behavior, I examine the link between geophysical phenomena that generate tsunamis and the ensuing tsunami waveforms from a phenomenological perspective (cf. Kanamori and Brodsky (2004)). The focus is on providing a review of tsunami observations, from generation through open-ocean propagation and runup. For the tsunami source, these observations include parameters, such as heterogeneous coseismic slip on the fault plane, that directly influence the initial conditions for tsunami propagation. I review the historical development of stochastic slip models that encompass much of the variability associated with the complex dynamics of fault rupture and that are constrained by the inversion of seismograms. For tsunami observations in the near field, I examine the relationship between source heterogeneity and spatial distribution of broadside runup and wave characteristics at oblique propagation paths. In addition, the timing of the maximum amplitude arrival is examined, both broadside and at oblique propagation paths from the source (Fig. 1). In the far field, I examine the statistics of wave amplitude as recorded by deep-ocean bottom pressure gages and coastal tide gages, that yield information on the origin of the stochastic nature of the tsunami wavefield. In each case, the description of tsunami event observations is heuristically guided by a review of analytic theory for the purpose of understanding various aspects of tsunami physics, ranging from the dynamic rupture of faults to nearshore wave behavior. Significant observations and their underlying physics are presented in this paper as several working hypotheses.

In accordance with the phenomenological objective of this study, results from numerical models are minimally used. The reason for this is to avoid the problem of needing high-resolution bathymetric and topographic data to accurately simulate complex hydrodynamics (e.g. nonlinearity, turbulence, rotational flow, etc.) in the nearshore region. The problem is most obvious when trying to simulate an entire tide gage record of a tsunami, where late arrivals may originate from coastline irregularities distant from the tide gage station. Because of the difficulty in collecting high-resolution nearshore bathymetry (especially in the surf zone) over long stretches of coastline, there are very few cases where late tsunami arrivals can be accurately predicted using numerical methods. Indeed, many of the late arrivals that make up the coda (i.e. the part of a tsunami time series that follows the first arrival) of a transoceanic tsunami originate from the fine-scale details of wave reflection from distant bathymetric features (e.g. see Koshimura *et al.* (2008); Kowalik *et al.* (2008)). Many of the same issues surrounding resolution in numerical ocean and coastal circulation models discussed by Greenberg *et al.* (2007) also apply to tsunami propagation models.

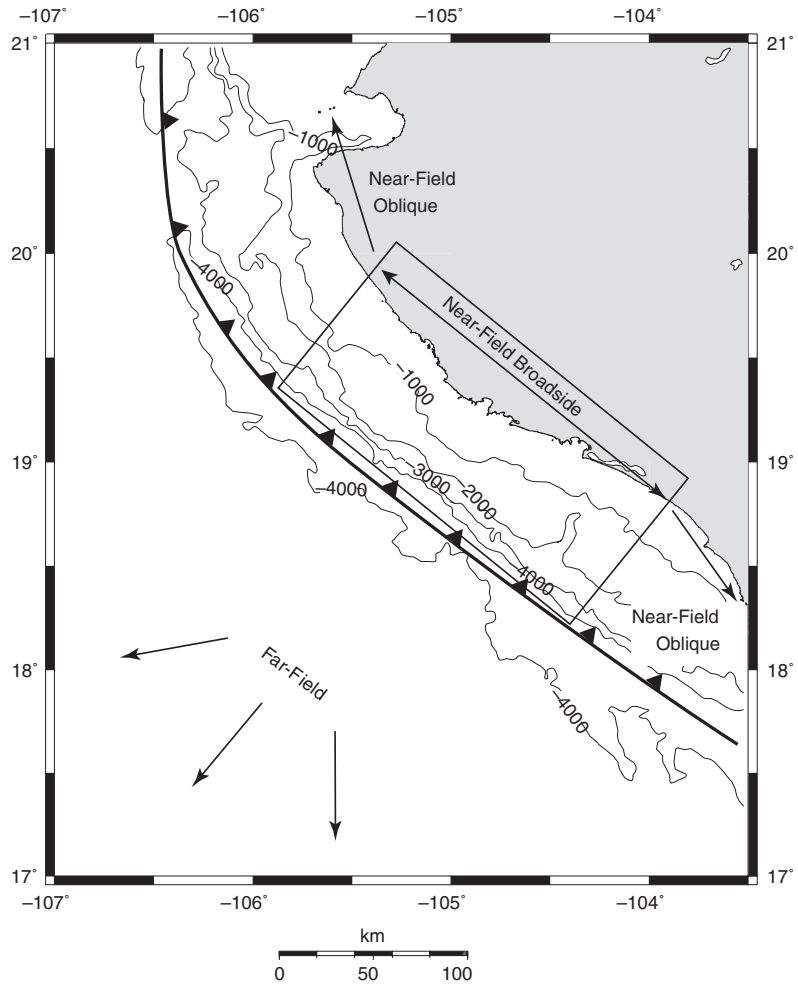

FIG. 1. Mapview of three different regimes for describing tsunami observations relative to projection of inter-plate thrust earthquake (solid rectangle): near-field broadside, near-field oblique, and far field (transoceanic).

2. GENERAL DESCRIPTION OF TSUNAMI GENERATION PHYSICS

Tsunamis are gravity waves initially induced by elevation changes in the water column commonly caused by various submarine geologic processes. The efficiency of solid-earth dynamic processes in transferring potential energy into the water column during tsunami generation is dependent on the time scale of geologic movements relative to the phase speed of long waves in the ocean. For the purpose of comparing rapid earthquake displacements with relatively slower landslide displacements, it is useful to mention the experimental and computational results of Hammack (1973). For the "impulsive"

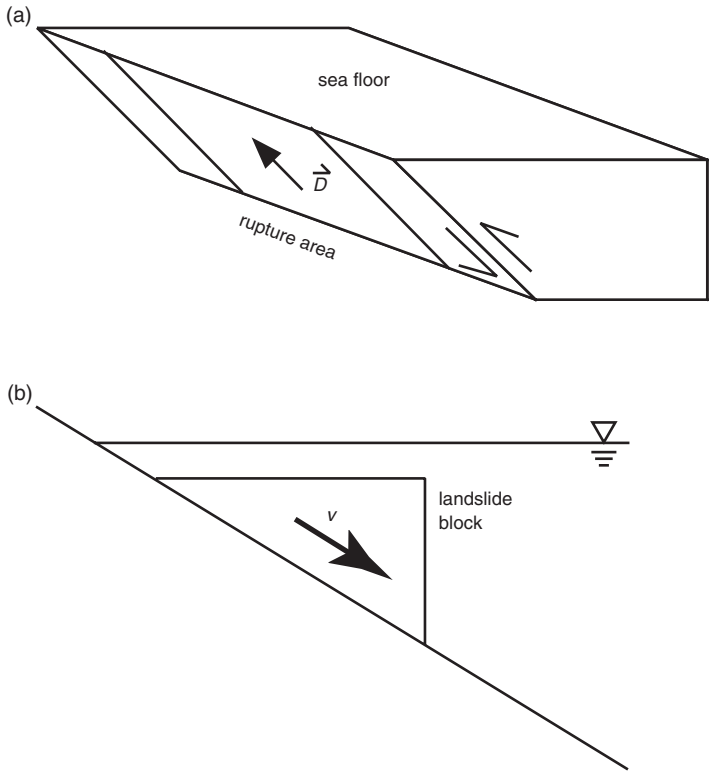

FIG. 2. Simple characterization of earthquake and landslide sources commonly used in past tsunami studies. (a) Uniform-slip vector ($\vec{D}$) within a rectangular rupture area along a planar fault. (b) Simple landslide block sliding down a constant slope with constant velocity (v).

seafloor displacement case, the leading wave profile away from the source region retains the shape of the seafloor displacement, but is reduced in amplitude by $1/2$ to account for the bidirectional propagation in a 1D analysis. In contrast, for the "creeping" case, defined by Hammack (1973) as having a rate of seafloor displacement much less than the tsunami phase speed, the wave profile reflects the time history of seafloor movement rather than the overall displacement of the seafloor. To the extent that these impulsive and creeping cases can be equated to earthquake and landslide movements, spatial and temporal variations, respectively, play a dominant role in the variability of the tsunami waveform.

It is helpful to first review conventional tsunami source models used in deterministic analyses. For both seismogenic and landslide sources, the unexpected behavior of tsunamis is in reference to these deterministic models that do not accurately capture the complex details of tsunami generation physics. In the case of seismogenic tsunamis, the uniform-slip dislocation model is conventionally used, particularly in hazard assessments (Fig. 2a). This model is advantageous in that the geometric and kinematic parameters

scale with seismic moment m_0 : $m_0 = \bar{\mu}\bar{D}_s\Sigma$, where $\bar{\mu}$ is the average shear modulus of rocks surrounding the rupture and $\bar{D}_s$ is the average static slip. Σ is the static rupture area (typically rectangular in shape) that is either estimated from scaling relations (e.g. see Geller (1976); Wells and Coppersmith (1994)) or from the spatial distribution of aftershocks following the earthquake. What is unaccounted for in simple tsunami generation models (and what is described below in Section 2.1) is the marked heterogeneity in the slip distribution, geometric complexities of the rupture zone, and heterogeneity in elastic moduli of rocks deforming in response to earthquake rupture.

For landslides, the conventional source model is that of a rigid block sliding down an inclined plane (Fig. 2b). This type of "wavemaker" description is convenient to implement in laboratory wave tanks for the study of various wave properties and effects on built structures. This description is also useful for benchmark comparisons of high-order numerical simulations to the wave tank measurements. Realistic landslides, however, are much more complex and diverse than the rigid block model. Various continuum (rheological and mixture theory) and granular descriptions reviewed in Section 2.2 have been used to numerically simulate landslide dynamics. Unfortunately, there are fewer data that can be used to determine the appropriate dynamic models and constitutive parameters for a given type of landslide compared with the amount of data available to develop earthquake physics models, though sample case studies are discussed in Section 3.2.

2.1. Earthquake Tsunami Generation

Tsunamigenic earthquakes typically occur at subduction zones, where two conditions related to the inter-plate thrust separating the subducting and overriding plate conspire to generate most of the world's damaging tsunamis. First, thrust motion results in higher amounts of vertical seafloor deformation in comparison to other fault mechanisms (e.g. strike slip). In particular, the dip of most inter-plate thrust faults is near the optimal dip for maximizing tsunami runup, according to the wave parameters used in runup laws (Geist, 1999). Second, the shallow dip of the inter-plate thrust fault greatly increases the possible rupture width through the seismogenic zone relative to vertical faults, for example. As a result, most of the world's largest magnitude earthquakes occur on inter-plate thrusts.

Earthquakes occurring on other faults at subduction zones have also generated devastating tsunamis in the near field (Satake and Tanioka, 1999). These include splay faults off the inter-plate thrust, thrust and reverse faults in the back arc (e.g. Sea of Japan), normal faults in the outer rise of the subducting plate caused by bending stresses (e.g. offshore Sanriku, Japan and Kuril Islands), intra-arc dip-slip faults (e.g. Mona Passage offshore Puerto Rico), and deeper earthquakes occurring within the subducting slab (Tanioka *et al.*, 1995). Several studies have indicated connectivity among these fault types, in terms of the evolution of stress during the seismic cycle (Dmowska *et al.*, 1988; Taylor *et al.*, 1998). For example, it has been observed that normal faulting earthquakes in the outer rise can occur after large inter-plate thrust earthquakes, owing to stress-transfer effects (Dmowska *et al.*, 1988; Polet and Thio, 2003). In addition, geometric complexity among these faults is often overlooked and can give rise to compound earthquake ruptures that may be difficult to classify among the fault descriptions described above (Baba *et al.*, 2005).

In the past, it was thought that the trench-normal convergence rate was an indicator of subduction zones capable of large magnitude earthquakes (Ruff and Kanamori, 1983), and hence, large transoceanic tsunamis. However, the occurrence of the 2004 Sumatra-Andaman earthquake clearly indicates that large, tsunamigenic earthquakes can occur along inter-plate thrusts that accommodate highly oblique relative plate motion with low rates of convergence. Because the rate of trench-normal convergence along oblique subduction zones is very low, the mean return times of large earthquakes in these zones are large, resulting in temporal under-sampling in the historical record (McCaffrey, 1994; Kreemer *et al.*, 2002; Bird and Kagan, 2004; Geist *et al.*, 2009b).

Vertical displacement of the seafloor associated with earthquakes is directly related to slip dynamics along the fault plane, starting from a rupture initiation point (i.e. the hypocenter) and expanding over a finite area of the fault until rupture is arrested. Earthquake rupture propagation is described by the constitutive relationship that relates shear stress (τ) to slip rate ($\dot{D}$). The evolution of slip is governed by a friction law that is dependent on the effective normal stress (σ_e), that includes pore pressure effects, and a state variable (θ), commonly known as the rate- and state-friction law (Dieterich, 1979; Rice, 1983; Ruina, 1983):

$$\tau = \sigma_e \left[\mu_0 + A \ln \left(\frac{\dot{D}}{D^*} \right) + B \ln \left(\frac{\theta}{\theta^*} \right) \right], \tag{1}$$

where μ_0 is the nominal coefficient of friction and A and B are additional constitutive parameters. Earthquake rupture occurs when friction is weakening with respect to slip rate, such that $B > A$. This defines a regime of unstable sliding, in contrast to stable, aseismic sliding. The state variable represents the time evolution of stationary contacts (Dieterich, 2007) according to

$$\frac{\mathrm{d}\theta}{\mathrm{d}t} = 1 - \frac{\theta \dot{D}}{d_c} \tag{2}$$

(Beeler *et al.*, 1994), where d_c is the critical slip-weakening distance (of μm scale) (see also Linker and Dieterich (1992)). The physics describing earthquake rupture therefore span many orders of magnitude in space (10^{-6} m for rupture nucleation to 10^{9} m for the largest rupture length) as well as time (10^{-3} s for the breakdown leading to fault slip to 10^{10} s for the interseismic period).

The frictional stability conditions associated with the initiation of tsunami earthquakes at shallow depth are difficult to reconcile with the conventional understanding described above. A subset of tsunami earthquakes termed "slow tsunami earthquakes" by Polet and Kanamori (2000) nucleate at shallow depths along the inter-plate thrust (or subsidiary faults) and rupture up-dip to the oceanic trench. "Slow" refers to the rupture velocity and is a function of the shear modulus, which decreases substantially with depth in subduction zones (Bilek and Lay, 1999, 2000). (Other tsunami earthquakes may be attributable to the effect that triggered submarine mass movements have on the total tsunami wavefield (Kanamori and Kikuchi, 1993).) The outstanding issue associated with slow tsunami earthquakes is how very shallow rupture can occur where velocity strengthening frictional conditions ($B < A$, Eq. (1)) should exist. Tanioka *et al.* (1997)

and Bilek and Lay (2002) suggest that the occurrence of slow tsunami earthquakes is related to the rough topography of the downgoing plate, which may provide nucleation points for tsunami earthquakes. Seno (2002) also suggests that the conditions necessary for slow tsunami earthquakes to occur may be a transient phenomena related to the evolution of fluid pressure in or around the fault zone (cf. Taylor (1998)).

There has been a concerted effort over the past decade or so to simulate earthquake slip dynamics according to the rate- and state-friction law, although most of the work to date has focused on continental fault zones rather than inter-plate thrusts. Most of the results reveal a rich complexity in earthquake slip dynamics depending on the constitutive parameters, discretization, pre-stress distribution and fault geometry. For example, Dieterich (1995) demonstrates that for increasing values of A, slip complexity increases with multiple subevents of high slip separated by zones of little to no slip. Among earthquake mechanics models, self-healing rupture pulses are frequently distinguished from a crack-like mode of rupture (Ben-Zion and Rice, 1997; Zheng and Rice, 1998; Nielsen and Carlson, 2000). For more details regarding earthquake friction laws, fault rheology, earthquake dynamics, and fault slip, the reader is referred to topical reviews by Scholz (1998), Dieterich (2007), Rice and Cocco (2007), and Fukuyama (2009).

Elastic deformation of the rocks surrounding the fault occurs in response to the rupture process. The dynamic displacements at the Earth's surface are described by elastic wave theory (e.g. see Aki and Richards (1980)). Because shear stress vanishes at the solid-fluid interface, it is the vertical component of dynamic displacements at the seafloor that is transmitted through the water column. These displacements primarily occur as oceanic Rayleigh waves that propagate along the Earth's surface. Whereas the restoring force of tsunamis is gravity, the restoring force for Rayleigh waves is elasticity (Okal, 1988; Dahlen and Tromp, 1998; Novikova *et al.*, 2002). Ohmachi *et al.* (2001) have simulated oceanic Rayleigh waves and tsunamis using a coupled model of dynamic displacements and showed that the maximum water heights are significantly greater above the source region, but approximately the same in the far field, in comparison to static displacements. Because oceanic Rayleigh waves are coupled with the overlying water column of the ocean, they propagate at phase and group speeds for elastic Rayleigh waves in the solid earth. Furthermore, because the solid earth and ocean are coupled during Rayleigh wave propagation, no runup occurs for these waves. In contrast, tsunamis are "free" (i.e. mostly uncoupled) gravity waves in the water column that propagate at phase and group speeds according to the long-wave hydrodynamic theory. Directly above the source region, however, wave heights may be significantly augmented by dynamic displacements.

Thus, tsunami generation relates more to the "static" displacement of the seafloor in response to earthquake rupture in contrast to seismic ground motion that depends on the time evolution of rupture. Static in this sense means final displacement in a reference frame prior to rupture nucleation. This can be also interpreted as "permanent" deformation (as in the formation of fault scarps, for example) on the time scale of tsunami propagation (but not necessarily on the time scale of the earthquake cycle). In seismology, the static displacement field can be derived from standard formulas for dynamic displacements with $t \to \infty$ (pg. 84, Aki and Richards (1980)).

Static elastic displacement at a point on the seafloor $\mathbf{r}(x, y)$ is the result of elastic deformation in response to coseismic slip $D(\xi, y)$ integrated across the entire fault plane

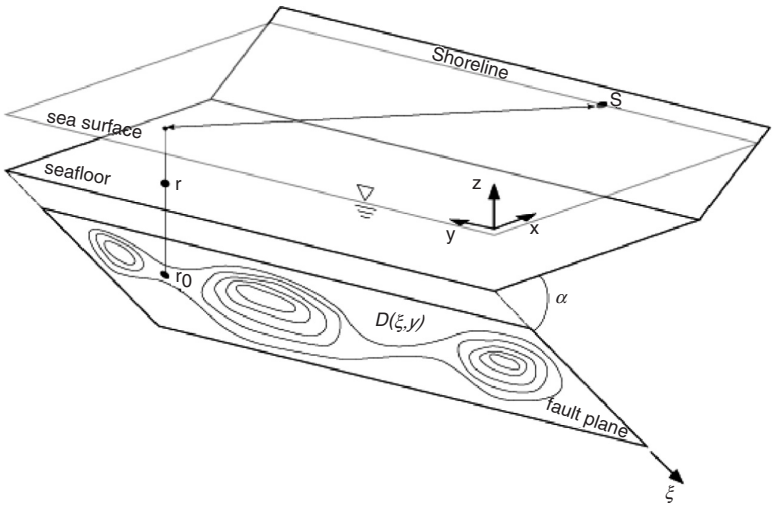

FIG. 3. Schematic perspective view of the tsunami problem. Slip on fault plane $D(\xi, y)$ results in coseismic displacement at a point on the seafloor $u_m(\mathbf{r})$. This in turn results in an initial disturbance at the sea surface that propagates to the shoreline as the tsunami observed at point **s.**

(Fig. 3). The three components of displacement ($m = 1, 2, 3$) at $\mathbf{r}$ can therefore be expressed as a function of slip at a point on the fault $\mathbf{r}_0$ (Rybicki, 1986)

$$u_m(\mathbf{r}) = \iint_{\Sigma} D_i(\mathbf{r}_0) v_j(\mathbf{r}_0) U_m^{ij}(\mathbf{r}, \mathbf{r}_o) \mathrm{d}\Sigma \tag{3}$$

where $\nu(\mathbf{r}_0)$ is the surface normal of a fault plane with arbitrary geometry and Σ is the area of the fault plane. For an isotropic medium, the six Green's functions are given by

$$U_m^{ij} = U_m^{ji} = \lambda \delta_{ij} G_m^{n,n} + \mu [G_m^{i,j} + G_m^{j,i}], \tag{4}$$

where λ is Lamé's first constant and δ_{ij} is the Kronecker delta. The static elastic Green's function has known analytic solutions only for a few simple slip distributions and fault geometries (e.g. see Singh *et al.* (1994)). Because Eqs (3) and (4) are based on the static approximation, temporal changes in slip and seafloor deformation during rupture propagation and slip evolution are not accounted for. Often parameters such as rupture propagation speed and rise time are used in a simple kinematic framework as in the Haskell rupture model (Haskell, 1964), particularly for very long ruptures such as the 2004 Sumatra-Andaman earthquake (Hirata *et al.*, 2006; Fujii and Satake, 2007). Recently, dynamic rupture propagation models have been employed that provide a physically consistent framework to predict the spatial and temporal heterogeneity of slip (e.g. see Wendt *et al.* (2009)).

2.2. Landslide Tsunami Generation

Generation of tsunamis by submarine landslides is a complex process that occurs through distinct temporal phases: failure, post-failure dynamics (e.g. debris flow), and turbulent boundary layer flow (i.e. turbidity currents). Because most tsunamigenic landslides are triggered by earthquakes, one has to consider inertial displacements of the uppermost compliant layer in response to strong-ground motion. Given that the conditions are met for failure to occur, it is likely that a shear dislocation develops at the base of the landslide and propagates in all directions to form the eventual head scarp (up slope) and initial sliding plane (down slope) (Martel, 2004; Petley *et al.*, 2005). Our primary concern for tsunami generation is the dynamics of the failed mass, which is described below. During the latter stages of mass movement failure, turbidity currents most often form. Because this process is characterized primarily by turbulent boundary layer flow and involves relatively smaller changes in seafloor displacement, it is usually not influential in the tsunami generation process.

Many and diverse types of landslides have been classified according to their physics and subaerial observational evidence. The most well known classification scheme is that of Varnes (1978). Since then, there has been a concerted effort to develop a detailed taxonomy of landslides, particularly of the flow type (Hungr *et al.*, 2001). The basic types of mass movements include slow-moving earth flows (sometimes termed landslides or slides in a specific connotation of the terms), topples, spreads, falls, and fast-moving flows (Locat and Lee, 2002). The concern for tsunami generation is primarily fast-moving submarine debris avalanches and debris flows. A recent classification of debris flows proposed by Coussot and Meunier (1996) is based on two criteria directly related to the mechanical properties of debris flows: solid/water fraction and material type (cohesive versus granular). This classification is seen as an important foundation for understanding the complex dynamics of debris flows that are governed by non-Newtonian rheologies.

In understanding the physics of debris flows, two approaches have primarily been considered: viscoplastic fluid and mixture (or granular) theory. Viscoplastic fluid models have been used to describe submarine muddy debris flows, whereas mixture theory has been used primarily to describe subaerial granular or two-phase flows. The latter has recently been incorporated into a coupled model for tsunami generation (Fernández-Nieto *et al.*, 2008). In adapting subaerial landslide dynamic models for the submarine environment, the main effect of having water as the ambient fluid, rather than air, is a reduction in gravitational forcing, owing to buoyancy.

Because most tsunamigenic mass movements along continental slopes involve predominantly fine-grained sediment, the viscoplastic fluid model for muddy debris flows is a central model for tsunami generation. A clay content of only 10% or more is needed for debris flows to be adequately modeled by viscoplastic rheology (Coussot and Meunier, 1996; Coussot *et al.*, 1998). The longitudinal momentum equation for laminar flow is given by

$$\rho_m \left(\frac{\partial u_x}{\partial t} + u_x \frac{\partial u_x}{\partial x} + u_z \frac{\partial u_x}{\partial z} \right) = \rho_m g \sin\theta - \frac{\partial p}{\partial x} + \frac{\partial \tau}{\partial z}, \tag{5}$$

where u_x and u_z are the velocity components in the x (down slope) and z directions respectively, ρ_m is the density of the mud flow, $p(x, z, t)$ is the pressure (assumed to be

hydrostatic), θ is the slope angle, and $\tau(x, z, t)$ is the shear stress in the mud flow (Jiang and Leblond, 1993; Imran *et al.*, 2001). The continuity equation for this system is

$$\frac{\partial u_x}{\partial x} + \frac{\partial u_z}{\partial z} = 0. \tag{6}$$

Various nonlinear constitutive relations have been used to relate shear strain rate to shear stress for muddy debris flows (Coussot, 1997). These include Bingham plastic, Herschel-Bulkley, and bilinear rheologies. The Bingham plastic fluid is characterized by a finite yield stress (τ_y) such that,

$$\mu\gamma = \begin{cases} 0 & \text{if } |\tau| < \tau_y \\ \tau - \tau_y \text{sgn}(\gamma) & \text{if } |\tau| \geq \tau_y, \end{cases} \tag{7}$$

where μ is dynamic viscosity and γ is the strain rate ($\gamma = \frac{\partial u}{\partial z}$). The Herschel-Bulkley rheology is a power-law rheology (i.e. non-Newtonian):

$$K\gamma^n = \begin{cases} 0 & \text{if } |\tau| < \tau_y \\ \tau - \tau_y \text{sgn}(\gamma) & \text{if } |\tau| \geq \tau_y, \end{cases} \tag{8}$$

where n and K are material-specific constants. When $n = 1$, the Herschel-Bulkley rheology is equivalent to the Bingham plastic rheology. The bilinear rheology (Locat, 1997) involves two viscous regimes of flow described by dynamic viscosities at low and high strain rates (μ_l and μ_h, respectively where $\mu_h < \mu_l$):

$$\tau = \left[\tau_{ya} + \mu_h |\gamma| - \frac{\tau_{ya}\gamma_0}{|\gamma| + \gamma_0} \right] \text{sgn}(\gamma), \tag{9}$$

where τ_{ya} is the apparent yield stress relative to the high strain rate regime and γ_0 is the reference strain rate given by

$$\gamma_0 = \frac{\tau_{ya}}{\mu_l - \mu_h}. \tag{10}$$

For these nonlinear rheologies, the no-slip boundary condition along the base of the debris flow results in two flow zones: a shear zone at the base of the flow where the shear stress is greater than the yield stress and a plug zone above where the yield stress is not exceeded. The boundary between the two zones is termed the yield interface. In formulating a solution to the momentum equations, the horizontal and vertical velocities and the horizontal velocity gradient are constrained to be continuous across the yield interface (Jiang and Leblond, 1993).

To model granular mass movements that have a smaller proportion of fine sediment and water, mixture theory that was developed for subaerial debris avalanches (Iverson and Denlinger, 2001) has been adapted in a few cases for the submarine environment (Fernández-Nieto *et al.*, 2008). For a two-phase solid/fluid mixture in which the fluid

velocities and accelerations differ negligibly from those of the solids, the momentum equation is

$$\rho_m \left(\frac{\partial \mathbf{v_s}}{\partial t} + \mathbf{v_s} \bullet \nabla \mathbf{v_s} \right) = \rho_m \mathbf{g} - \nabla \bullet (\mathbf{T_s} + \mathbf{T_f}) \,, \tag{11}$$

where $\mathbf{T}_s$ and $\mathbf{T}_f$ are the stress tensors for the solid and fluid phases, respectively, and the density of the mass movement is calculated from the volume fractions (V_s and V_f) of each phase $\rho_m = \rho_s V_s + \rho_f V_f$. The constitutive theory used is intergranular Coulomb friction, modified by pore pressure and Newtonian viscous fluid stresses. For high enough pore pressures, internal friction is greatly reduced and the mass behaves viscously. It has been argued that mixture theory has limited application in the submarine environment because pore pressure diffusion is likely to be minimal and because a finite yield strength is needed to explain the thickness and mid-slope termination of many submarine debris avalanches (Coussot and Meunier, 1996; Elverhøi *et al.*, 2005). However, mixture theory may be applicable in specific geologic environments such as carbonate and volcanic-dominated islands, away from continental sources of clay.

2.3. Tsunami Propagation

Large-scale changes in ocean surface elevation induced by earthquakes, landslides, and other geologic phenomena present quasi-initial conditions for tsunami propagation. The relevant non-dimensional wave parameters are

$$\varepsilon = \frac{a_0}{h_0}, \quad \mu = \frac{h_0}{\ell_0}, \quad \delta = \frac{\Delta h}{h_0}, \tag{12}$$

where a_0 is the characteristic wave amplitude, h_0 the characteristic water depth, ℓ_0 the characteristic wavelength, and Δh is the change in seafloor depth. When the dispersion parameter μ is small ($\ll 1$), the shallow-water wave equations are appropriate to describe tsunami propagation. These equations include the continuity equation

$$\frac{\partial(\eta + h)}{\partial t} + \nabla \bullet [\mathbf{v}(\eta + h)] = 0 \tag{13}$$

and the momentum equation

$$\frac{\partial \mathbf{v}}{\partial t} + (\mathbf{v} \bullet \nabla)\mathbf{v} + g \nabla \eta = 0, \tag{14}$$

where h is the water depth (a function of time owing to source dynamics), η is the wave elevation, and $\mathbf{v}$ is the depth-averaged horizontal vector velocity field. When dispersion cannot be neglected, wave components are separated such that different frequencies propagate at different speeds (i.e. frequency-dependent phase speed). For small ε, the nonlinear convective inertia term $(\mathbf{v} \bullet \nabla)\,\mathbf{v}$ in Eq. (14) above can be ignored, resulting in the linear long-wave equations. Conventionally, the linear form is valid in deep water

until the water approaches the shore (i.e. $\varepsilon \rightarrow 1$). However, as noted by Lynett and Liu (2002), nonlinear effects are present in the source region for landslide tsunami generation where seafloor displacement can be of the same order as the water depth. The reader is referred to other publications that comprehensively describe the physics of tsunami waves (Carrier, 1971; Mei, 1989; Madsen and Schäffer, 1998; Liu, 2008; Lynett, 2008).

For earthquakes, the initial tsunami amplitudes in the source region are typically less than those for tsunamigenic landslides. However, landslide-generated tsunamis have much smaller source dimensions and are more affected by frequency dispersion, leading to a greater attenuation of the initial wave amplitude in the far field. Therefore, whereas seismogenic tsunamis can have destructive influences at far-field distances, the impact of landslide-generated tsunamis is limited to the near field.

A particular aspect of tsunamis that is critical in analyzing the data that follow is the coastal response of tsunamis, including the excitation of edge waves and runup. Edge waves are a particular type of coastal wave trapped by refraction that propagate parallel to the coastline. In combination with scattering and resonance resulting from propagation along an irregular coastline, edge waves create a complex waveform in which the offshore amplitude, runup, and timing of the largest wave are difficult to predict.

The theoretical understanding of edge waves is based on simple shelf and slope geometries. Edge waves occur in distinct modes (n), with the fundamental mode ($n = 0$), also known as the Stokes mode, which is the most commonly observed. For a semi-infinite sloping beach of slope β, the dispersion relation is (Ursell, 1952; Liu *et al.*, 1998)

$$\omega_n^2 = g k_n \sin(2n+1)\beta, \quad (2n+1)\beta < \pi/2. \tag{15}$$

Snodgrass *et al.* (1962) developed the propagation characteristics of edge waves along a flat shelf and distinguished between the discrete edge wave modes and leaky modes that occupy a continuous spectrum. Ishii and Abe (1980) considered a more complex case of edge waves along a stepped continental margin profile with an intervening linear slope and compared their results (dispersion relation and amplitude of the fundamental-mode edge wave) with those from the vertical step profile. The amplitude of edge wave modes for a semi-infinite sloping beach is based on Laguerre polynomials of order n ($L_n(x)$) and is of the form (González *et al.*, 1995)

$$\eta_n(x, y) = A e^{i(k_n y - \omega_n t)} e^{-k_n x} L_n(x). \tag{16}$$

The cross-shore wave profiles for the first few edge modes are shown in Fig. 4. For the more general case, the amplitude function is a solution to the confluent hypergeometric equation (Kummer's equation) (Ishii and Abe, 1980; Mei, 1989).

Runup describes the evolution of tsunami waves as they progress up a beach slope. Analytically, it is a particularly difficult hydrodynamic problem to solve, owing to nonlinearity near the runup front (Liu *et al.*, 1991) and moving boundary conditions (Kennedy *et al.*, 2000; Lynett *et al.*, 2002). Carrier and Greenspan (1958) provided a general solution to the problem, using a hodograph coordinate transformation that results in a linear form of the wave equation. A later study (Carrier, 1995) looked specifically at tsunami runup of both the broadside and edge waves from a near-field source. Analytic runup laws have been derived for specific waveforms, such as solitary

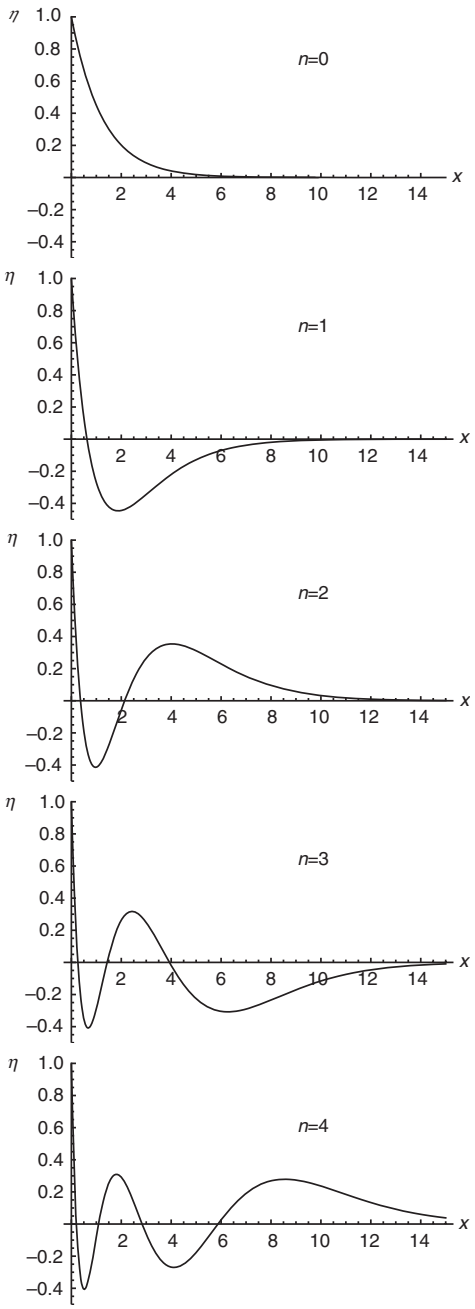

FIG. 4. Cross-shore wave profiles of the first five edge wave modes for a semi-infinite sloping beach (Eq. (16)).

waves (Synolakis, 1987) and *N* waves (Tadepalli and Synolakis, 1994). Recently, Madsen *et al.* (2008) has examined solitary wave theory in detail as it applies to tsunamis. Recent studies have also generalized the Carrier and Greenspan transform to include arbitrary incident waveforms (Carrier *et al.*, 2003; Tinti and Tonini, 2005). Using runup theory to explain field observations is complicated by variable offshore topographies (Kanoglu and Synolakis, 1998). Specific methods have also been developed to handle turbulence that may be highly significant for large tsunamis (most notable observed for the 2004 Indian Ocean tsunami), both in the form of bottom boundary layer flow (parameterized by bottom friction) and for cases where the tsunami breaks offshore and develops into a bore (Yeh, 1991; Chen *et al.*, 2000; Kennedy *et al.*, 2000; Lynett *et al.*, 2002). A recent review of tsunami runup and inundation is given by Yeh (2008) and Lynett (2008).

3. Near-field Regimes: Broadside and Oblique

In this section, I examine the phenomenology of tsunami events in the near field. First, source observations that directly relate to tsunami generation are reviewed. The focus here will be on the spatial distribution of coseismic slip along the fault plane for seismogenic tsunamis, deduced from inversions of seismic, geodetic, and tsunami data that have a primary effect at near-field distances. I then examine how source variations affect the near-field tsunami, both in coastal regimes broadside from and oblique to the rupture zone. In this respect, the approach can be considered as a stochastic initial boundary value problem as defined by Leblond and Mysak (1978) in which the spatial distribution of the wave forcing function is random, as are the propagation characteristics along the coast. In the broadside regime, I examine how spatial distributions in runup are causally related to spatial distributions of slip on the fault. In the near-field oblique regime, I examine the importance that edge wave propagation has in explaining tsunami observations.

3.1. Source Observations—Earthquakes

Data used to determine kinematic rupture processes for tsunamigenic, subduction zone earthquakes primarily include waveforms recorded by strong motion and broadband seismic instruments. Inverse methods can be performed on this data to determine the slip history during rupture. Seismic inversion methods include inverting body waves (Kikuchi and Kanamori, 1991), surface waves (Ihmlé, 1996a) and wavelet methods to simultaneously invert seismic and geodetic data (Ji *et al.*, 2002). The inversion of seismic data requires assumptions of fault geometry and other fixed parameters such as crustal structure (Beresnev, 2003). The fault orientation is often available from seismicity studies, centroid moment tensor inversion (e.g. see Tsai *et al.* (2005)) or from focal mechanism determination (e.g. first motions), although for the latter, it is difficult to constrain the dip of shallow-angle faults, such as inter-plate thrusts, owing to the steep take-off angle of teleseismic *P* waves (Michael and Geller, 1984). Rupture length and width are often estimated from the aftershock distribution. Other difficulties arise because of the heterogeneous velocity structure associated with subduction zones (Engdahl *et al.*, 1982; Kisslinger, 1993). Despite these limitations, there is a great

deal of information available from seismic inversions on the slip distribution of past tsunamigenic earthquakes.

Geodetic measurements and tsunami waveforms provide additional data to resolve the static slip distribution of earthquakes. The availability of high-precision GPS data greatly increases the amount of data one can use to determine slip distribution, although earlier leveling data is valuable for historic earthquakes as well. Care must be taken in processing geodetic data to account for after-slip and post-seismic earth responses (Heki and Tamura, 1997; Miyazaki *et al.*, 2004; Hashimoto *et al.*, 2006; Pollitz *et al.*, 2008). The direct arrival of tsunami waveforms also provides valuable data to invert for slip distribution (e.g. see Fujii and Satake (2007); Piatanesi and Lorito (2007)). As will be discussed in Section 4.1, the direct unobstructed part of the tsunami waveform that is analyzed in tsunami inversions is quite stable during propagation and not subject to random processes that, for example, dictate maximum tsunami amplitude that can occur later in the tsunami coda.

Seismic and geodetic inversions resolve slip best toward shore, where the observation stations are located, whereas tsunami inversions resolve slip best in deeper water (i.e. at shallow depths below the seafloor for inter-plate thrust earthquakes) (Sagiya and Thatcher, 1999). Therefore joint inversions of the aforementioned data sets are particularly useful to fully resolve slip throughout the rupture zone of large earthquakes (e.g. see Johnson *et al.* (1996); Thio *et al.* (2004); Ichinose *et al.* (2007); Rhie *et al.* (2007)). However, to avoid any apparent circular reasoning in this paper involving slip that could be determined from the tsunami data I am describing, I focus primarily on slip distributions determined from seismic waveform inversions.

Observed slip distributions are spatially complex and are considered self-affine, to the extent provided by the resolution of the inverted data. This characteristic of coseismic slip is a result of rupture dynamics, either through fractal pre-stress conditions, or from fault roughness (cf. Andrews (1980); Power and Tullis (1991); Oglesby and Day (2002)). Several different statistical models have been developed to describe these observations. The slip distribution model initially developed by Andrews (1980) and further discussed by Herrero and Bernard (1994) is characterized by a power-law decay in the wavenumber spectrum beyond a corner wavenumber k_c:

$$D(k) = C\frac{\Delta\sigma}{\mu}\frac{L}{k^2} k > k_c \tag{17}$$

where $\Delta\sigma$ is the mean stress drop, μ the shear modulus, L the rupture dimension and C a constant. It has been shown that the wavenumber decay exponent can be linked to the spectral decay of far-field seismic displacement amplitudes in the frequency domain (Hanks, 1979; Frankel, 1991; Hisada, 2000, 2001). Therefore there are two different types of observations that can be used to constrain the stochastic slip model: seismic displacement spectrum and seismic inversions. For the former, there have been several studies that define the spectrum of inter-plate thrust earthquakes (e.g. see Hartzell and Heaton (1985)). Interestingly, given the unique behavior of slow tsunami earthquakes in many other respects, Polet and Kanamori (2000) find similar spectral decay exponents as for typical inter-plate thrust earthquakes that rupture at deeper focal depths.

Seismic inversion results have been used to determine spectral decay of slip for the more general case of $D(k) \propto 1/k^{\nu+1}$ for a 2D fault, where ν controls the long-range correlation or "roughness" of the slip distribution. Tsai (1997a) estimated optimal values of ν for six different onshore earthquakes (most of them with two different published inversion solutions using different methodologies). Mai and Beroza (2002) refined the statistical estimation by considering slip distribution from the standpoint of several different spectral decay laws, including the fractal model (Eq. (20)), Gaussian, exponential, and von Kármán autocorrelation functions. They found that the von Kármán autocorrelation function provides the best fit, though slip distributions are also well described by the fractal distribution. The von Kármán autocorrelation function used by Mai and Beroza (2002) includes different correlation lengths in the strike and the dip direction (a_x and a_z, respectively), such that

$$D(k) \propto \frac{a_x a_z}{\left(1 + k^2\right)^{\nu+1}}. \tag{18}$$

(The autocorrelation function is related to the power spectrum via the Fourier transform according to the Wiener-Khintchine theorem, e.g. see Andrews (1980).) In comparing the slip distribution models to seismic inversion results, Mai and Beroza (2002) found a scale-invariant value for the spectral decay exponent that is greater than 2.

Lavallée *et al.* (2006) considered the possibility that slip fluctuates more than the standard stochastic model described above. The stochastic slip distribution model is fully defined by the wavenumber spectrum ($D(k)$ above) and a random function $R(x)$, such that

$$D(x) = D_0 F^{-1}\left[R_s(k) D(k)\right], \tag{19}$$

where $F^{-1}[\bullet]$ is the inverse Fourier transform, $R_s(k)$ is the Fourier transform of $R(x)$ and D_0 is a constant (Liu-Zeng *et al.*, 2005). Typically, $R(x)$ is specified by a Gaussian distribution with zero mean. As indicated by Lavallée *et al.* (2006), $D(k)$ specifies the long-range correlation of the slip function whereas $R(x)$ specifies its variability.

Lavallée and Archuleta (2003) first noted the variability of slip associated with the 1979 Imperial Valley earthquake from inversion of near-field strong motion data (Archuleta, 1984) and indicated that a distribution family more general than the Gaussian should be considered to encompass this high variability. The Lévy α-stable distribution is considered in which the characteristic function for the probability distribution is given by (Samorodnitsky and Taqqu, 1994)

$$j(k) = \begin{cases} \exp\left\{ik\mu - c^{\alpha}|k|^{\alpha}\left[1 - i\beta\,\mathrm{sgn}(k)\tan\dfrac{\pi\alpha}{2}\right]\right\} & \text{if } \alpha \neq 1 \\ \exp\left\{ik\mu - c|k|\left[1 - i\beta\dfrac{2}{\pi}\mathrm{sgn}(k)\ln|k|\right]\right\} & \text{if } \alpha = 1 \end{cases}, \tag{20}$$

where α is a stability parameter ($0 < \alpha \leq 2$), μ a shift parameter (real number), β a skewness parameter ($-1 \leq \beta \leq 1$), and c a scale parameter ($c \geq 0$). For $\alpha = 2$, this becomes the characteristic function for the Gaussian distribution with mean

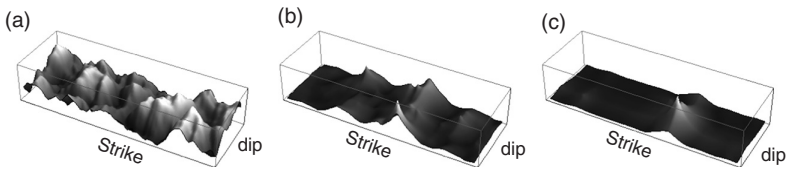

FIG. 5. Example of stochastic slip distributions using three different distributions for $R(x)$: (a) Gaussian; (b) Cauchy; (c) Lévy. The power spectrum $D(k)$ is the same in each case.

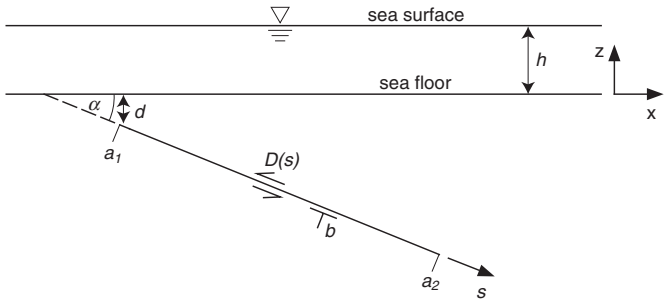

FIG. 6. Schematic and coordinate system for calculating elastic displacement from an edge dislocation on an inclined fault.

μ and variance $2c^2$. Examples of distributions with heavier density tails include the Cauchy distribution ($\alpha = 1$ and $\beta = 0$) and the Lévy distribution ($\alpha = 1/2$ and $\beta = 1$). Figure 5 compares different slip distributions using the same wavenumber spectrum but different distributions for $R(x)$ (Gaussian, Cauchy, and Lévy). The heavy-tail distributions (Fig. 5b, c) produce more extreme values of slip, relative to the average slip within the rupture zone. Lavellée et al. (2006) estimated distribution parameters (α, μ, β, and c) and the wavenumber decay exponent ($\nu + 1$) for several earthquakes, including the predominantly dip-slip 1994 Northridge event. Most earthquakes analyzed have α-values less than 2, and therefore have heavy tails.

Although there are very few direct observations of static displacement of the seafloor, displacement can be computed from the dislocation theory if a statistical description of coseismic slip is known, such as that described above. The general form of the coseismic displacement equation (Eqs (3) and (4)) is applied for cases that result in tsunami generation. For tsunami applications, the focus is on the vertical component of displacement, although horizontal displacement can be calculated in a similar fashion. In addition, inclined dip-slip faults such as the inter-plate thrust of subduction zones are of primary interest. Surface displacement for an edge dislocation on an inclined fault with Burger's vector b as shown in Fig. 6 has been derived by several authors (e.g. see Dmowska and Kostrov (1973); Freund and Barnett (1976); Rudnicki and Wu (1995)). Freund and Barnett's (1976) expression using the geometric parameters shown in

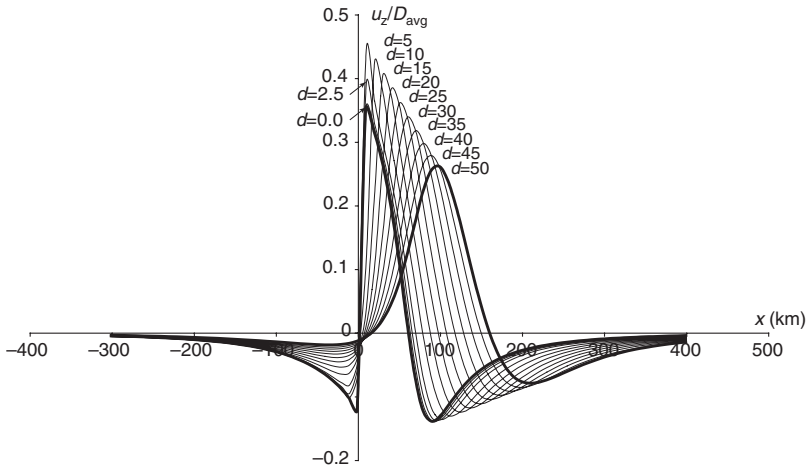

FIG. 7. Vertical displacement profiles from a crack along the inclined fault plane specified in Fig. 6 as a function of depth d to the top of rupture (in km). Bold lines represent end-member cases ($d = 0$ km and 50 km). Vertical uplift u_z is normalized with respect to average slip D_{avg}. Rupture width = 80 km, length = 200 km, and dip (α) = 30°.

Fig. 6 is

$$u_z(x, s) = bU_z(x, s), \tag{21}$$

where

$$U_z(x, s) = \frac{xs \sin^2 x}{\pi(x^2 + s^2 - 2xs \cos\alpha)} + \frac{\sin\alpha}{\pi} \tan^{-1}\left(\frac{x - s\cos\alpha}{s \sin\alpha}\right). \tag{22}$$

For a crack of finite width and distributed slip (i.e. dislocation density), expressions for displacement at the seafloor are obtained by integrating Burger's vector solutions (see Dmowska and Rice (1986) for a summary). The integral form for vertical displacement given by Freund and Barnett (1976) is

$$u_z(x, 0) = \int_{a_1}^{a_2} U_z(x, s) D'(s) \mathrm{d}s. \tag{23}$$

Variation in vertical displacement profiles as a function of source depth is shown in Fig. 7. These results show that for a given slip distribution, the vertical displacement is characterized by a two-sided displacement field in the strike-normal (wave profile) direction: uplift in the up-dip direction and subsidence in the down-dip direction. This transformation from one-sided slip (i.e. positivity constraint) to two-sided vertical displacement is linked to the slip gradient term $D'(s)$ in Eq. (23) above. As the depth to slip on the fault becomes shallower (i.e. toward the seafloor), the vertical displacement profile becomes sharper. When slip on the fault breaks through to the seafloor, a scarp

is formed (that is correspondingly attenuated in the water column). The conditions for which this would occur are discussed by Rudnicki and Wu (1995). In general though, the static elastic Green's function in essence acts as a low-pass spatial filter of the slip distribution in calculating seafloor displacements (cf. Figure 11 in Geist and Dmowska (1999)). Green's function also effectively transforms the one-sided slip functions to a two-sided displacement profile in the dip direction (uplift and subsidence).

Within the water column, the tsunami Green's function derived by Kajiura (1963) relates seafloor displacement to ocean surface elevation. In effect, short wavelengths of the seafloor displacement field are filtered through the water column by a factor of $1/\cosh(kh)$. For most earthquakes, this does not result in a significant attenuation from seafloor displacement to generation of the initial tsunami wavefield. However, fault scarps and anomalously short-wavelength components of the displacement field will be filtered out in deep water during tsunami generation. 3D simulations of tsunami generation by Saito and Furumura (2009b,c) indicate that horizontal deformation wavelengths of the seafloor must be at least 10 times the water depth for the surface height to mimic vertical seafloor displacement (within approximately 10%).

For inter-plate thrust earthquakes, it is important to recognize the strong structural heterogeneity in rock types and elastic properties. Sediment that is accumulated on the downgoing plate is accreted onto and underplated beneath the overriding plate. Typically the inter-plate thrust of a subduction separates high modulus igneous rocks below from low modulus sedimentary rocks above, though the fault may not be exactly co-located with the contact between rock types. Ma and Kusznir (1994) and Savage (1998) investigated the effect that horizontal elastic layering has on surface displacements through the derivation of analytic solutions to the governing equations. For more complex cases, finite-element models have also been widely used to account for elastic heterogeneity in the calculation of surface displacement fields (e.g. see Yoshioka *et al.* (1989); Cattin *et al.* (1999); Masterlark *et al.* (2001); Masterlark (2003); Zhao *et al.* (2004); Sato *et al.* (2007)). For example, the effect of elastic heterogeneity has been investigated for potential tsunamigenic earthquakes ($M_w = 6.5$) on the Seattle fault (Fig. 8a, b), which trends up-dip from high rigidity basement rocks into low rigidity sedimentary rocks of the Seattle basin (Geist and Yoshioka, 2004). Figure 8c shows a comparison of the vertical displacement field using an elastic half-space and using elastic constants specific to basement and sedimentary basin rocks.

There are very few measurements of seafloor deformation arising from earthquake rupture for testing the aforementioned models. One exceptional record, however, is the measurement of vertical displacement by a bottom pressure recorder that is part of a cabled deep-sea observatory (Hirata *et al.*, 2002) during the 2003 Tokachi-Oki earthquake (Baba *et al.*, 2006b; Mikada *et al.*, 2006; Nosov and Kolesov, 2007). Rapid vertical displacement of the seafloor excited low-frequency elastic oscillations in the water column that dominated the pressure observations (Nosov and Kolesov, 2007). Measured coseismic displacement, after filtering out the water-column oscillations, was consistent with the elastic displacement models of the event (Mikada *et al.*, 2006), using a slip distribution inverted from the observed seismograms of the earthquake (Yamanaka and Kikuchi, 2003; Yagi, 2004). Other than this notable example, observations of both coseismic slip (from seismic inversions) and vertical displacement at the Earth's surface for a single event are only available for onshore earthquakes and not for submarine events.

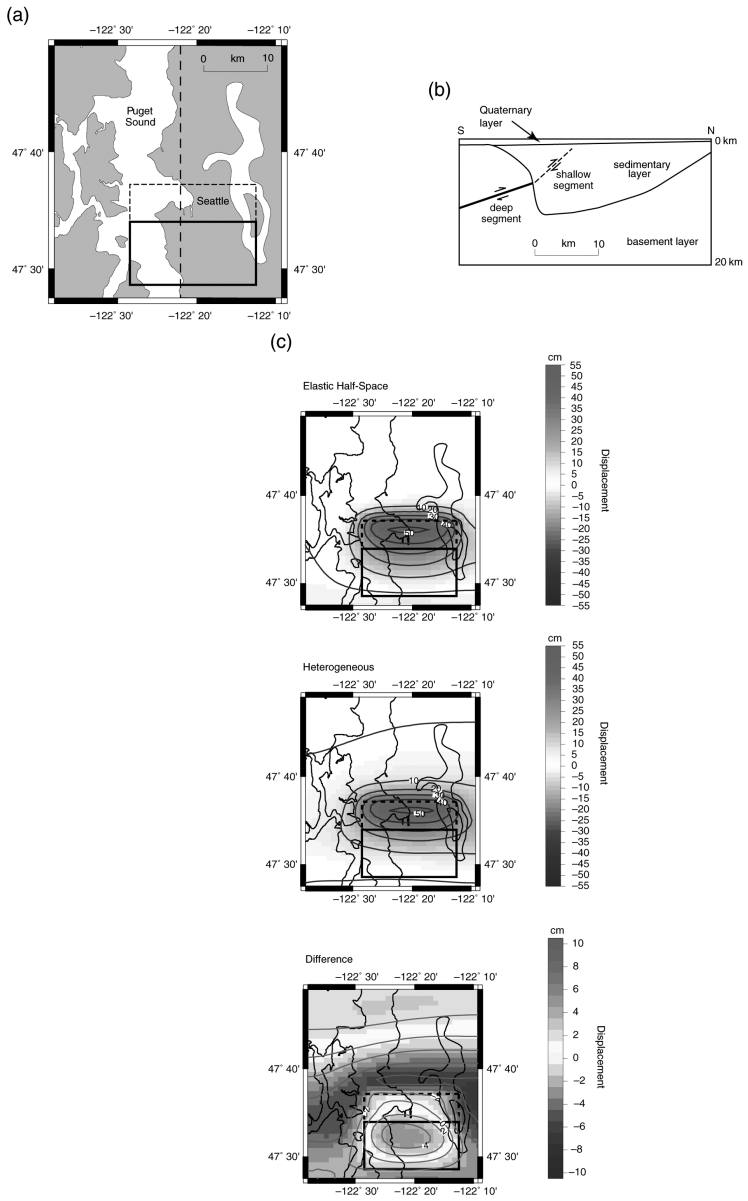

FIG. 8. (a) Mapview of Puget Sound with projection of deep (bold rectangle) and shallow (dashed rectangle) segments of the Seattle fault. (b) Cross section showing the structure of Seattle sedimentary basin. Slip on the Seattle fault extends from basement rocks up-dip into the Seattle basin. (c) Comparison of vertical displacement fields from a homogeneous elastic structure (half-space) and elastic heterogeneity arising from the structure of the Seattle basin (Geist and Yoshioka, 2004). Difference between the two displacement fields shown at the bottom.

The lack of seafloor displacement measurements precludes a direct determination of whether rupture can occur along splay faults that are synthetic to the inter-plate thrust. The possibility of splay fault rupture has been proposed to explain a greater than expected near-field tsunami for a given amount of slip (e.g. see Fukao (1979); Cummins and Kaneda (2000)). Splay faults in the hanging wall of inter-plate thrusts have been imaged by seismic-reflection profiles for specific subduction zones, typically in the accretionary wedge (e.g. see Park *et al.* (2002); Moore *et al.* (2007); Sibuet *et al.* (2007)). Because seismic waveforms cannot routinely detect branching rupture paths for inter-plate thrust earthquakes, most of our knowledge as to whether splay fault rupture can occur comes from an understanding of fault mechanics. Several recent studies indicate that splay fault rupture can only occur under specific pre-stress conditions and branch angles (Poliakov *et al.*, 2002; Kame *et al.*, 2003; Bhat *et al.*, 2007; Templeton *et al.*, 2009). In addition, barriers to inter-plate rupture in the strike direction may create the necessary conditions for rupture to jump to a splay fault segment (Wendt *et al.*, 2009). Our primary observational evidence of splay fault rupture is from the inversion of near-field tsunami waveforms (Baba *et al.*, 2006a).

3.2. Source Observations—Landslides

Unfortunately, there is no routine instrumental monitoring of submarine landslides analogous to seismograms such that one could directly infer the dynamics and kinematics of landslide movement. There have been some studies of seismic waves generated by energetic landslides (both submarine and subaerial) that are worth noting. Landslides can be distinguished from earthquakes on seismograms by a depletion of high-frequency energy (e.g. see La Rocca *et al.* (2004)) and are represented by a horizontal point force at the surface (Dahlen, 1993), rather than a double-couple system of forces used to represent an earthquake mechanism. Recently, an unusual seismic recording of an event in the Gulf of Mexico may be ascribed to a submarine landslide according to these characteristics (Nettles, 2007). Furthermore, Brodsky *et al.* (2003) demonstrated that the basal friction of landslides can be estimated from a given source-time function (Kanamori *et al.*, 1984), concluding that basal friction does not appear to significantly vary for the three subaerial volcanogenic landslides they analyzed.

To some extent, tide gage records can be used to constrain the location and constitutive parameters of the landslide (as described in Section 2.2), although there are very few confirmed instrumental recordings of landslide tsunamis. One example is the 1929 Grand Banks tsunami that possibly had a landslide-generation component. The triggering earthquake and geomorphology of the submarine failure have been described in several studies (e.g. see Hughes Clarke (1990); Bent (1995); Piper *et al.* (1999)). From these descriptions and using simplified assumptions of uniform thickness and Newtonian viscosity, Fine *et al.* (2005) were able to show that the tsunami resulting from the landslide is consistent with travel-time observations for the initial wave and the amplitude as recorded at the Halifax, Nova Scotia tide gage station (see also Trifunac *et al.* (2002)). Another example is the landslide in Monterey Canyon triggered by the onshore 1989 Loma Prieta earthquake that generated a tsunami recorded by the nearby Monterey tide gage station (Ma *et al.*, 1991). The timing of the direct arrival and the waveform characteristics as observed on the tide gage record are used to determine the approximate location of the landslide (near the canyon head) and a low yield stress using the bilinear

constitutive relation (Eqs (9) and (10)), respectively (Geist *et al.*, 2009a). Both the 1929 Grand Banks and 1989 Monterey Canyon debris flows were accompanied by vigorous turbidity currents in their aftermath.

3.3. Tsunami Observations—Near-field Broadside Regime

I turn now to the effect that spatially heterogeneous slip and displacement of the seafloor that was discussed in Section 3.1 has on near-field tsunami runup. In this section, earthquakes are primarily examined, based on the availability of instrumental source data and associated statistical models. It should be noted, at minimum, that seismically triggered submarine landslides can cause anomalous fluctuations in near-field runup, beyond what is expected from earthquake sources, although it has been exceedingly difficult in the past to make a direct connection from a landslide observed in seafloor mapping to a measurable tsunami. In the examples presented below, it is unlikely that there were landslide components to the tsunami.

In the near-field broadside regime, the focus will be on tsunami arrivals using tide gage measurements and tsunami severity related to runup measurements. Tide gage measurements are routine and temporally resolved, whereas runup measurements taken during post-tsunami field surveys are indicative of only the maximum flow depth or runup throughout the inundation of multiple waves arrivals (Farreras, 2000). Runup measurements consist of a variety of water-level measurements made within the inundation zone, including flow depths relative to the local topographic elevation and runup at the point of maximum inundation relative to sea level at the time of the tsunami. Vertical measurements are made from flow indicators or marks left by the tsunami (e.g. vegetation discoloration from salt water and bark stripped from trees). Measurements are made relative to a horizontal datum and must be corrected for the tidal height at the time of the tsunami (Baptista *et al.*, 1993). There is inherent uncertainty in these measurements, owing to misidentification of water marks and tsunami catalogs that do not distinguish runup from flow depths (Borrero, 2001).

The near-field tsunami runup problem is divided into two coastal regimes: broadside runup (i.e. directly across from the rupture zone at strike-normal azimuths) and oblique runup (Fig. 1). This is a logical division inspired by the theoretical work on near-field wave characteristics by Carrier (1995). In that study, he provided an elegant solution to the broadside and oblique runup problem that is expanded from the canonical hodograph transformation of Carrier and Greenspan (1958).

Several working hypotheses are presented below for the near-field broadside regime and throughout the rest of this study for the other two regimes based on both observed tsunami records and our current understanding of tsunami physics.

HYPOTHESIS 1. *For reasonably regular coasts, maximum offshore tsunami amplitude is most often associated with the first arrival, a non-trapped phase.*

This hypothesis is surprisingly difficult to test for several reasons: (1) many near-field tide gage stations become inoperable during significant tsunamis, (2) the definition of the near-field broadside regime is dependent on the length of rupture and spatially restricts which tide gage stations can be used for a test, and (3) there is a difficulty in defining what broadside is for very irregular coasts. An example is shown in Fig. 9a where the Corinto

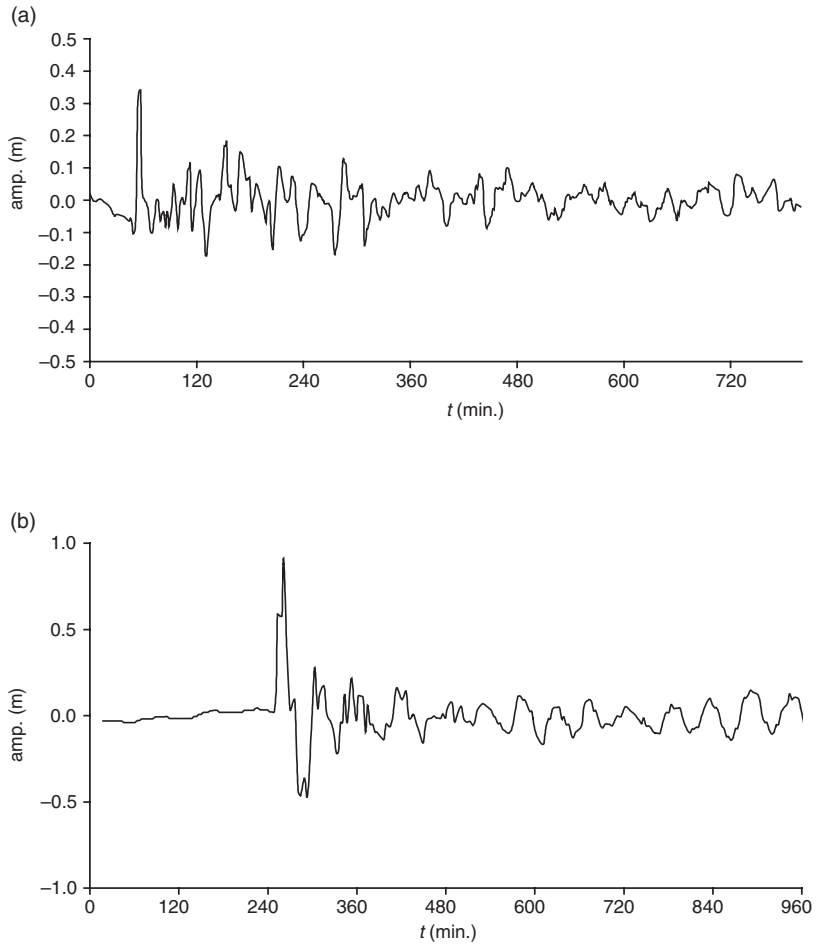

FIG. 9. Examples of near-field and regional tide gage records that are broadside from the rupture zone: (a) Corinto (Nicaragua) record of the 1992 Nicaragua tsunami; (b) Gan (Maldives) record of the 2004 Indian Ocean tsunami.

tide gage station recorded the tsunami from the 1992 Nicaragua tsunami earthquake (Baptista *et al.*, 1993). (The nearby Puerto Sandino tide gage station became inoperable during this tsunami.) The Corinto station clearly shows that the maximum amplitude is associated with the first or direct arrival.

In addition, a few regional tide gage recordings are available for the 2004 Indian Ocean tsunami (Rabinovich and Thomson, 2007) that are in line with the primary beaming pattern from the source region (Geist *et al.*, 2007) and hence could be considered as broadside recordings. For example, the Gan tide gage record from the Maldives shown in Fig. 9b also shows that the maximum amplitude is associated with the first arrival. In general, many island stations have a much less resonant response than continental stations (Watanabe, 1972).

Many Japanese tide gage stations recorded the tsunami from the 2003 Tokachi-Oki earthquake (Hirata *et al.*, 2004), showing the transition of behavior from the near-field broadside to near-field oblique regimes (Fig. 10). The broadside stations include Shoya (which became inoperable) and Tokachikou (which went off scale, interpolated by a dashed line). The Kushiro, Akkeshi, and Krittapu stations are near the source region, but away from the main region of uplift located near the epicenter (star). From the available data, it does appear that the maximum amplitude is associated with the first arrival. While this hypothesis works well for simple coasts, it may not hold for highly irregular coastlines where the maximum amplitude is associated with a later phase (not the direct arrival), as evident from broadside tide gage records from the 1964 Gulf of Alaska tsunami (Lander, 1996).

Analytic studies of runup dynamics provide an understanding of how the offshore waveform relates to runup at the point of maximum inundation. Carrier (1995) uses a Gaussian initial tsunami waveform to show the evolution of tsunami runup with time. Broadside from the source region, the wave history predicted by analytic theory is characterized by a solitary runup/drawdown phase associated with the first arrival of the wave. The exact wave history (i.e. wavelength and amplitude) depends on how far the source region is from shore. Carrier *et al.* (2003) expands the broadside analysis for other waveforms that correspond more to vertical displacement fields associated with elastic dislocations from earthquakes as well as landslide movements. Results from these studies are consistent with Hypothesis 1, although they inherently assume a wave profile that is homogeneous along strike. Therefore, results from actual earthquakes may be restricted to regions broadside from high slip patches on the fault (e.g. see Fig. 10).

HYPOTHESIS 2. *Strike-parallel distribution of maximum amplitude and runup is significantly affected by fault slip heterogeneity.*

In this case, a causal link is proposed between slip heterogeneity and variations in runup distribution (cf. Geist (2002)). As with Hypothesis 1, testing is difficult in regions with irregular shorelines or events along island arcs, for example, which results in scattering and excitation of trapped modes. Again, the 1992 Nicaragua tsunami earthquake provides a good case study, in that there are two distinct slip patches separated by a significant distance, and the coastline and offshore bathymetry are relatively uniform (Fig. 11). The moment distribution is determined from the inversion of seismic surface waves by Ihmlé (1996a,b). The slip distribution is directly related to the moment distribution, assuming a depth-dependent shear modulus (Geist and Bilek, 2001). The runup distribution shown in Fig. 11 is from two separate post-tsunami field surveys (Abe *et al.*, 1993; Baptista *et al.*, 1993). Regions of high runup are directly correlated in a strike-parallel sense with regions of high slip. However, there is significant runup in the intervening regions (broadside from regions of very low slip) caused by the constructive interference of spreading waves from the two regions of high slip (Geist and Dmowska, 1999).

The 1952 and 2003 Tokachi-Oki tsunamis provide another test for Hypothesis 2. In this case, the moment magnitude ($M_w = 8.1$ and $M_w = 8.0$, respectively) and epicenter for the two earthquakes are very similar (Fig. 12). Therefore, difference in the runup distribution can be ascribed primarily to difference in the slip distribution between the

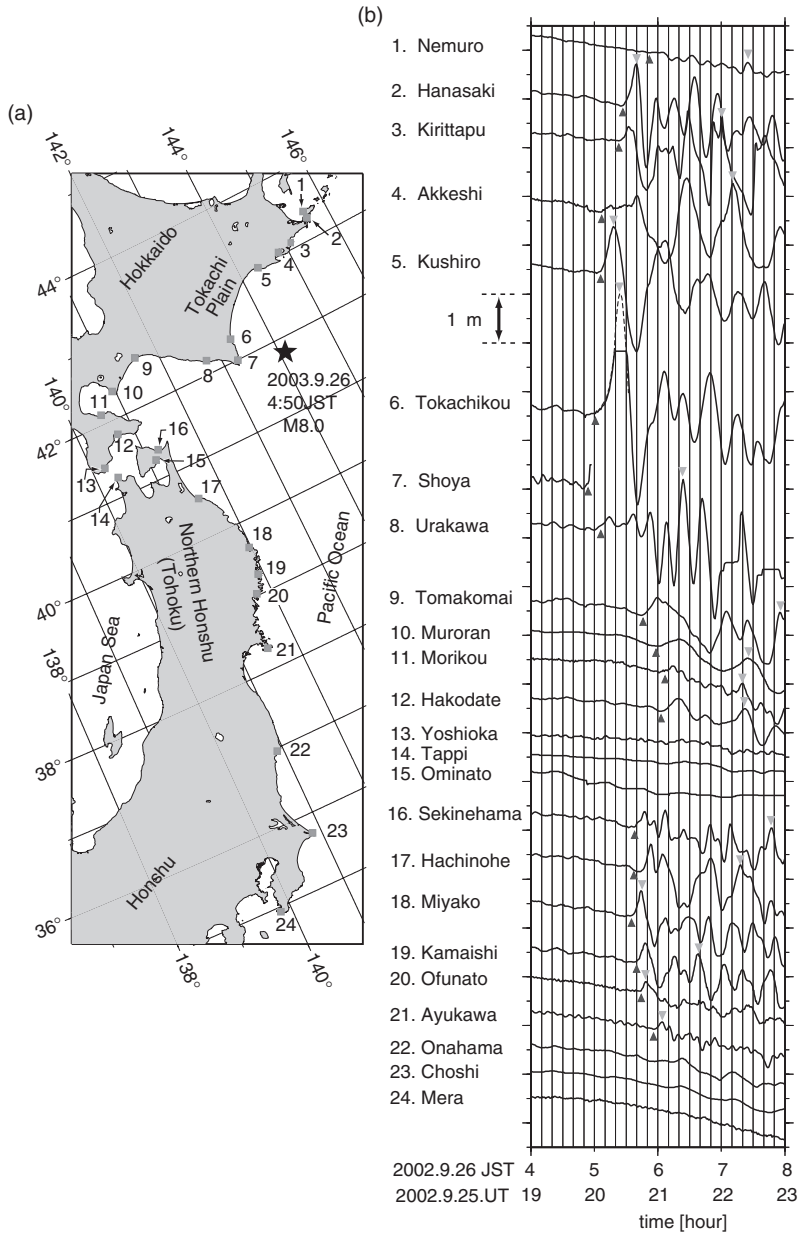

FIG. 10. Near-field Japanese tide gage records of tsunami from the 2003 Tokachi-Oki earthquake (modified from Hirata *et al.* (2004)). (a) Station location map. Star indicates the location of the earthquake epicenter. (b) Tide gage records (including tidal component); dashed where interpolated. Upward triangle marks the first arrival time; downward triangle marks the time of maximum peak amplitude.

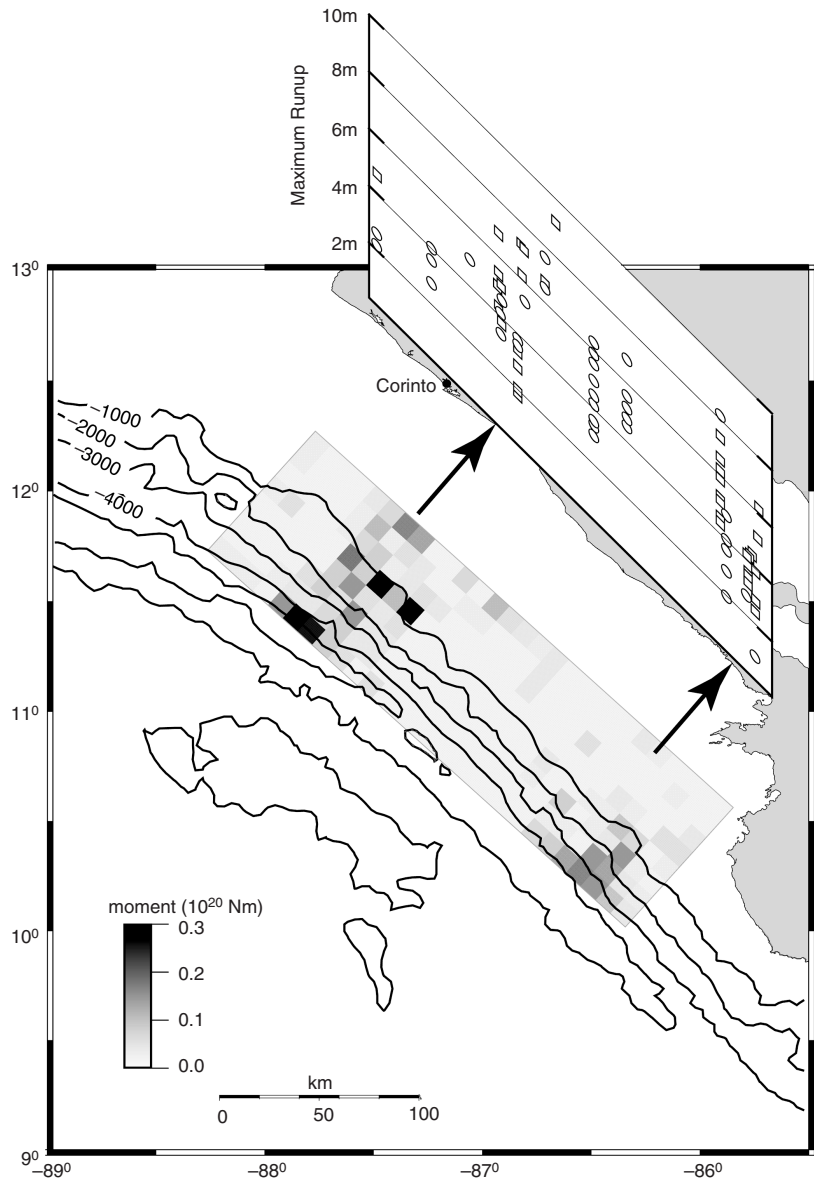

FIG. 11. Correlation of along-strike rupture complexity and along-shore runup for the case of the 1992 Nicaragua tsunami earthquake. Moment distribution from inversion of seismic surface waves (Ihmlé, 1996a,b). Runup distribution from field surveys: Abe *et al.* (1993) (open circles); Baptista *et al.* (1993) (open squares). Bathymetric contour interval: 1000 m.

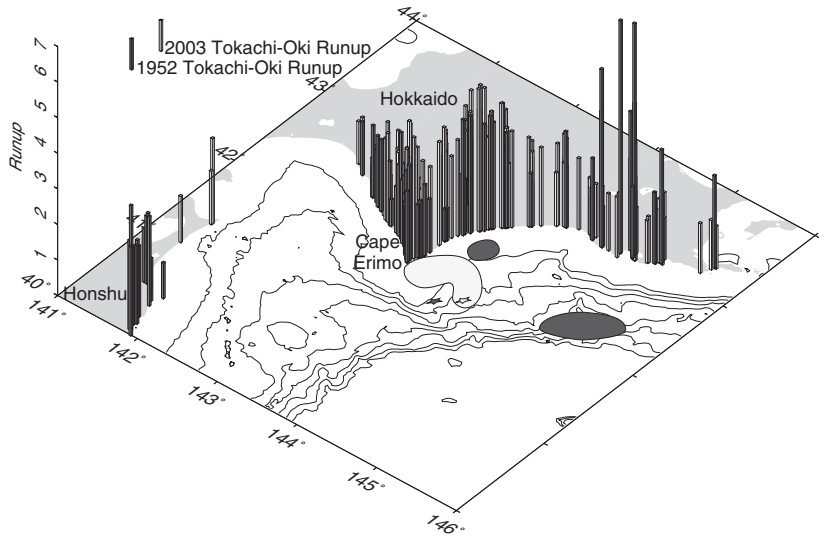

FIG. 12. Runup distribution from tsunami generated by the 1952 (shaded bars) and 2003 (open bars) Tokachi-Oki earthquakes (Tanioka *et al.*, 2004). Epicenters are indicated by shaded and open stars, respectively. Regions of high slip are shown schematically for each earthquake (shaded—1952; open—2003) (cf. Hirata *et al.* (2003); Yamanaka and Kikuchi (2003)). Bathymetric contour interval: 500 m.

two events. For each case, there are spatially dense runup measurements taken from post-tsunami surveys (Tanioka *et al.*, 2004). The slip distribution for the 1952 earthquake occurred in two regions away from the epicenter: one small region near the Hokkaido coast and another larger region beneath deep water broadside from the NE Hokkaido coast (Hirata *et al.*, 2003). The slip distribution for the 2003 earthquake occurred near the epicenter, toward Cape Erimo and primarily beneath shallow water (Yamanaka and Kikuchi, 2003). As with the 1992 Nicaragua tsunami, regions of high runup are correlated along shore with regions of high slip along strike (Fig. 12).

More quantitative descriptions of runup observations are provided by statistical models. Existing statistical models for the spatial distribution of runup (R) are based on the log-normal distribution. In particular, Choi *et al.* (2002) examined measured runup values in the near-field (not distinguishing between broadside and oblique regimes) for 11 tsunamis in the Pacific from 1992 and 1998 and found that all of the events, except for one, can be fit by a log-normal distribution with a density distribution

$$f(R) = \frac{1}{R\sigma\sqrt{2\pi}} \mathrm{e}^{-\frac{(\ln(R)-\mu)^2}{2\sigma^2}}, \tag{24}$$

where μ and σ are the mean and the standard deviation of $\ln(R)$, respectively. The exception is the 1996 Sulawesi tsunami that is best fit by a power-law distribution. In a follow-up study, Choi *et al.* (2006) examined the runup distributions associated with the 2004 Indian Ocean tsunami in eight different regions and again concluded that a log-normal distribution is the optimal statistical model.

Although one-point statistical models, such as the log-normal model described above, adequately fit the observed data, one would expect that there should be a characteristic length-scale of broadside runup that is proportional to the fault rupture length (along strike). Okal and Synolakis (2004) attempted to fit the maximum runup distribution parallel to the near-field shoreline (y-axis) for 9 tsunamis (spanning the years 1946-2002) with the following shape function:

$$R(y) = \frac{b}{[(y-c)/a]^2 + 1}, \tag{25}$$

where a, b, and c are adjustable parameters. They found that the aspect ratio $I_2 = b/a$ scales with the size of the earthquake and that I_2 for runup associated with near-field landslide tsunamis is distinctly different from that for seismogenic tsunamis. The logical next step of developing empirical two-point statistical models of tsunami runup is difficult, owing to the uncertainty and non-uniformity of maximum runup measurements in the field. Alternatively, deriving statistical runup models from two-point slip models described in Section 3.1 is equally difficult, owing to the complexity imposed by wave propagation and the runup process itself (i.e. "site response"). An analogous connection between statistical slip models and seismic ground motions, with its inherent seismic propagation and site response complexities, has been investigated by many researchers (e.g. see Tsai (1997b); Berge *et al.* (1998); Somerville *et al.* (1999); Guatteri *et al.* (2004)). Presently, therefore, the optimal model for runup distribution may indeed be the log-normal distribution discussed by Choi *et al.* (2002), especially when considering the complexity of wave propagation and response in the near-field regime and the possibility of triggered landslide tsunamis contributing to the total tsunami wavefield.

HYPOTHESIS 3. *Broadside runup increases where high coseismic slip is located beneath deep water.*

Near-field broadside runup is not only dependent on the magnitude of vertical seafloor displacement derived from slip on the fault, but also the water depth where this displacement occurs. As a tsunami propagates from deep water to shallow water, the amplitude increases according to Green's law derived from ray theory or the conservation of energy flux:

$$A \propto b^{-1/2} h^{-1/4}, \tag{26}$$

where b is the distance between rays and h is the water depth. Typically, the variation in b is negligible so that Green's law is reduced to $A \propto h^{-1/4}$. Although the quarter exponent suggests a weak dependence with depth, ocean depths where tsunamis are generated (from shelf to trench) can vary by at least two orders of magnitude, making the shoaling amplification effect significant. In addition, the wavelength shortens and leading wave steepness increases during shoaling, as discussed by Mei (1989). The wavelength, height and steepness, in addition to leading polarity, are all important factors in determining runup (e.g. see Pelinovsky and Mazova (1992); Tadepalli and Synolakis (1994); Carrier *et al.* (2003); Tinti and Tonini (2005)). For a given amount of slip on the up-dip portion of

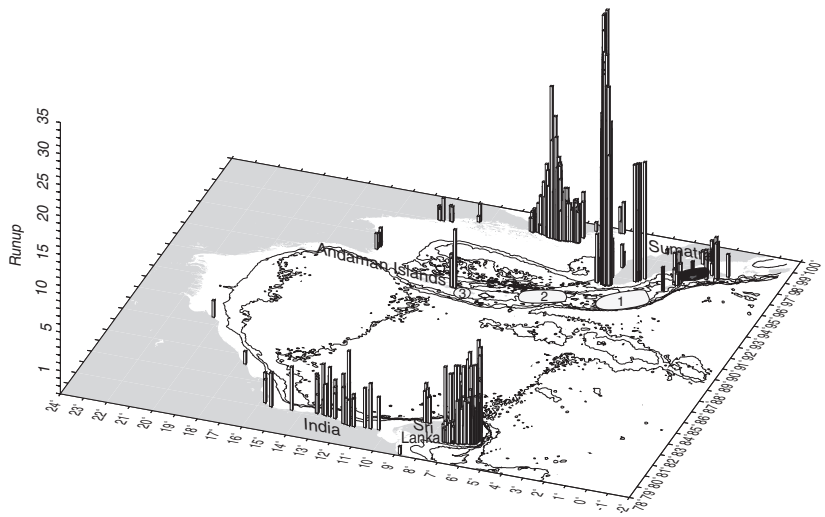

FIG. 13. Runup distribution from tsunamis generated by the 2004 Sumatra-Andaman (open bars) and 2005 Nias (black bars) earthquakes. Epicenters are indicated by open and shaded stars, respectively. Regions of high slip are shown schematically for each earthquake (open—2004; black—2005) (cf. Ammon *et al.* (2005); Banerjee *et al.* (2007); Chlieh *et al.* (2007); Rhie *et al.* (2007)). Bathymetric contour interval: 1000 m.

the inter-plate thrust, the amplitude and wavenumber of the initial tsunami wave profile will first be higher compared to the same amount of slip on a down-dip portion of the thrust, owing to the effects of the elastic response in the solid earth (see Fig. 7). This difference will then be accentuated during propagation toward shore through the effects of Green's law in the ocean.

This effect can be observed by again examining the comparison between the 1952 and 2003 Tokachi-Oki earthquakes (Fig. 12). The overall maximum runup of the 1952 earthquake is located broadside from a region of high slip beneath deep water. The region of high slip associated with the 2003 earthquake is in shallower water and does not result in maximum runup as large as in 1952, even though the seismic moments for the two earthquakes are very similar.

Another illustrative example is the tsunami runup from the $M_w = 9.2$ 2004 Sumatra-Andaman earthquake (Fig. 13). The slip pattern during this 1200-1600 km long rupture (Ishii *et al.*, 2005; Meltzner *et al.*, 2006; Subarya *et al.*, 2006) was complex and highly variable (cf. Ammon *et al.* (2005); Banerjee *et al.* (2007); Chlieh *et al.* (2007); Rhie *et al.* (2007)). High slip occurred in primarily three regions (numbered from south to north in the direction of rupture propagation; see Fig. 13). Slip was highest in region 1 and there are suggestions that slip was concentrated on the shallow portion of the inter-plate thrust beneath deep water (Bilek, 2007; Rhie *et al.*, 2007; Seno and Hirata, 2007). Correspondingly, tsunami runup was highest broadside from region 1 (i.e. in NW Sumatra and Sri Lanka). High slip in region 2 is broadside from high tsunami runup across the Andaman Sea in Thailand (e.g. Phuket). Slip in region 3 is difficult to resolve

(Ammon *et al.*, 2005), but is possibly correlated with the runup observed on the Andaman Islands.

The effect of regions of high slip located in deep water has also been discussed in comparing the tsunamis from the 2004 Sumatra-Andaman earthquake and the $M_w = 8.7$ March 28, 2005 Nias earthquake as described by Geist *et al.* (2006). The maximum runup from the 2004 earthquake was over 30 m, whereas the maximum runup from the 2005 earthquake was approximately 4 m. Although the difference can partly be ascribed to the overall higher seismic moment for the 2004 earthquake, the high slip region broadside from the area of maximum runup possibly occurred in deeper water near the trench in 2004 as mentioned above, whereas high slip occurred either beneath shallow water or on land (Nias and Sumatra Islands) in 2005 (Fig. 13).

3.4. Tsunami Observations—Near-field Oblique Regime

For the near-field oblique case (Fig. 1), observations indicate that the maximum tsunami arrival is often related to edge waves. Two hypotheses can be formulated from the available data and our understanding of tsunami physics.

HYPOTHESIS 4. *Maximum amplitude and runup are most often derived from late arrivals resulting from the interaction of trapped phases (i.e. edge waves).*

A good case study that tests this hypothesis is the tsunami generated from the 1983 $M_w = 7.7$ Nihonkai-Chubu (Sea of Japan) earthquake (Abe and Ishii, 1987). Because edge waves are scattered by longshore irregularities, it is often difficult to track the propagation of edge wave phases in tide gage records. However, Abe and Ishii (1987) show a smooth section of the western Honshu coastline, approximately 160 km long, in which the arrival time of the maximum amplitude is closely aligned with the predicted group velocity of edge waves. Another near-field oblique example that is consistent with this hypothesis is the tsunami record at the Crescent City tide gage station following the 1992 $M_w = 7.2$ Cape Mendocino earthquake (González *et al.*, 1995).

An Airy phase exists at a minimum in the group velocity for edge waves and has been observed in Japan from the tsunami generated by the 1952 $M = 9.0$ Kamchatka earthquake (Ishii and Abe, 1980; Golovachev *et al.*, 1992). The Airy phase is particularly pronounced owing to interference effects, as is commonly observed with Airy phases associated with solid-earth seismic waves (Lay and Wallace, 1995). A minimum in the group velocity for fundamental mode edge waves is predicted from the step bathymetry model (Ishii and Abe, 1980). Although there is an exponential decay associated with scattering of edge waves, including the Airy phase, from an irregular coastline, the e-folding distance can be particularly long for continents. For the NE Japan margin, the e-folding distance is estimated to be over 400 km (Fuller and Mysak, 1977).

The oblique stations of the 2003 Tokachi-Oki earthquake also provide a test to this hypothesis (Fig. 10). For most of the oblique stations such as Urakawa (station 8), the largest wave arrives significantly later than the first arrival (Tanioka *et al.*, 2004). Note, however, the direct propagation path from the earthquake to Miyako (station 18, Fig. 10). The largest wave in this case is the first arrival. As the tsunami proceeds southward down the Honshu coastline, edge waves appear to be dominant relative to the first arrival.

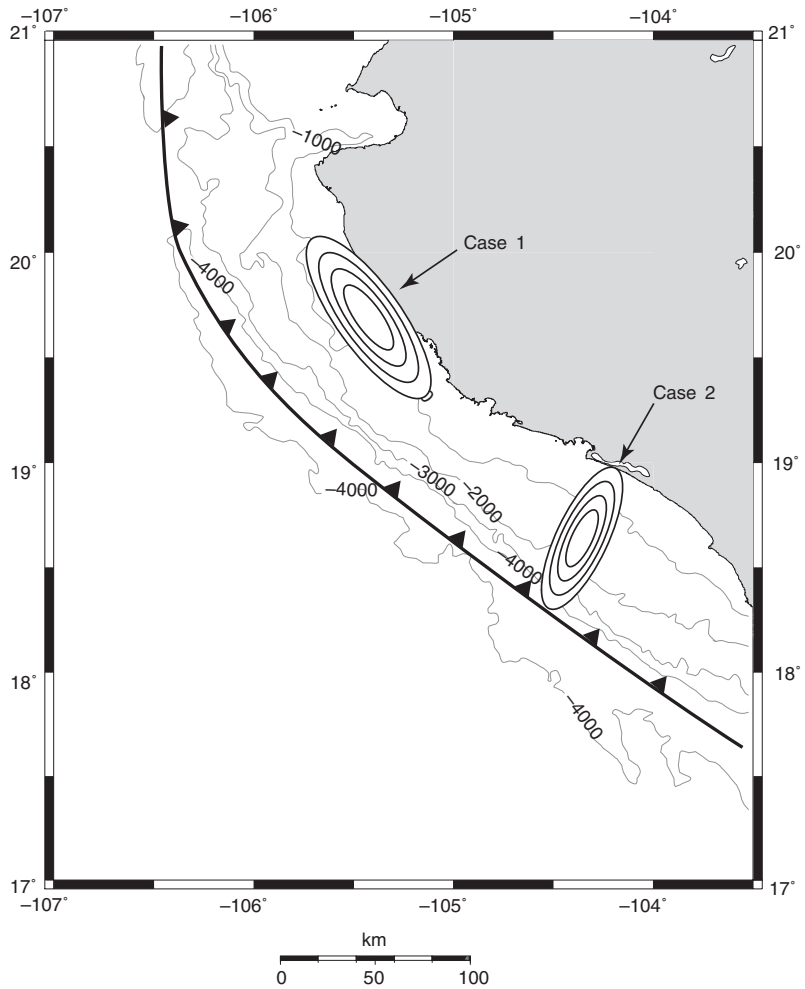

FIG. 14. Two cases of edge wave excitation examined by Fujima *et al.* (2000) for an initial vertical disturbance near the coastline. Case 1: elliptical disturbance oriented parallel to the coastline (e.g. earthquake). Case 2: elliptical disturbance oriented normal (e.g. landslide).

HYPOTHESIS 5. *There exists a causal (but complex) relationship between fault slip heterogeneity and near-field oblique tsunami amplitude.*

Because edge waves frequently scatter and resonate during propagation in the near-field oblique regime, it is difficult to directly trace the influence that source heterogeneity has on edge wave characteristics. The analytic investigation of edge waves propagating along a linear coastline with uniform slope by Fujima *et al.* (2000) is heuristically useful in this regard (Fig. 14). They examine what effect the orientation of the initial tsunami

wavefield (as specified by the long axis of an elliptical disturbance) has on edge wave characteristics. For the case where the initial disturbance is located near the coast with the long axis oriented parallel to the coast, the fundamental mode edge wave ($n = 0$, Fig. 4) dominates (see also Liu *et al.* (1998)). This case is apropos for typical inter-plate thrust earthquakes, in which the vertical displacement field spans across and is oriented subparallel with the coastlines (e.g. see Fig. 15). Details of the displacement field which include localized areas of uplift and subsidence appear to have a significant effect on the types of edge waves excited, with higher-mode edge waves associated with components of the displacement field located farther offshore (Kajiura, 1972; Fujima *et al.*, 2000). Kajiura (1972) also demonstrated that edge wave excitation increases with a decrease in the along-strike length of components of the vertical displacement field. A complex displacement field as shown in Fig. 15 is likely to generate many edge wave phases at fundamental and higher modes.

In the second case examined by Fujima *et al.* (2000), the near-coast displacement is oriented with the long axis normal to the coastline (Fig. 14). In this case, the excited edge wave is dominated by the first-order mode ($n = 1$; see Fig. 4) and is much more irregular than for the first case examined by Fujima *et al.* (2000). This case is apropos for nearshore landslides. Lynett and Liu (2005) reached similar model-based conclusions specific to landslide tsunamis. Both Fujima *et al.* (2000) and Lynett and Liu (2005) noted the possibility that the maximum amplitude associated with the near-field oblique wave can be greater than that for the near-field broadside wave. For an initial disturbance located far offshore (e.g. as with slow tsunami earthquakes located near the trench), little edge wave energy is excited for the ideal case of a uniform coastline (Kajiura, 1972; Fujima *et al.*, 2000). However, slight perturbations at the coast can also excite edge waves (Guza and Davis, 1974; Fuller and Mysak, 1977).

4. Far-field Regime

In this section, time-series statistics from deep-ocean and shore-based measurements are examined in the far field. The dominant aspect of the far-field tsunami is the tsunami coda evident in time-series records. Whereas the leading wave from the source tends to retain its initial waveform, the maximum tsunami amplitude at the coast most often occurs during the arrival of the coda. It is difficult to accurately model the tsunami coda, both in the open ocean and at the coast, using numerical models. The coda observed in the deep ocean and at the coast can be described from a phenomenological perspective, focusing on the amplitude and timing of the largest observed wave. Tsunami bottom pressure recorder (BPR) and tide gage data from the recent November 2006 and January 2007 Kuril Islands earthquakes are used as an example. Figure 16 shows the locations of the earthquakes and the stations where tsunami time-series data are discussed. The data shown in Fig. 16 also include a seismic surface wave arrival (under-sampled at a sampling rate of 1 minute) that precedes the tsunami direct arrival and the tsunami coda. The seismic surface wave is stronger for the January 2007 outer-rise normal faulting earthquake compared to the November 2006 inter-plate thrust earthquake because of differences in the seismic radiation patterns.

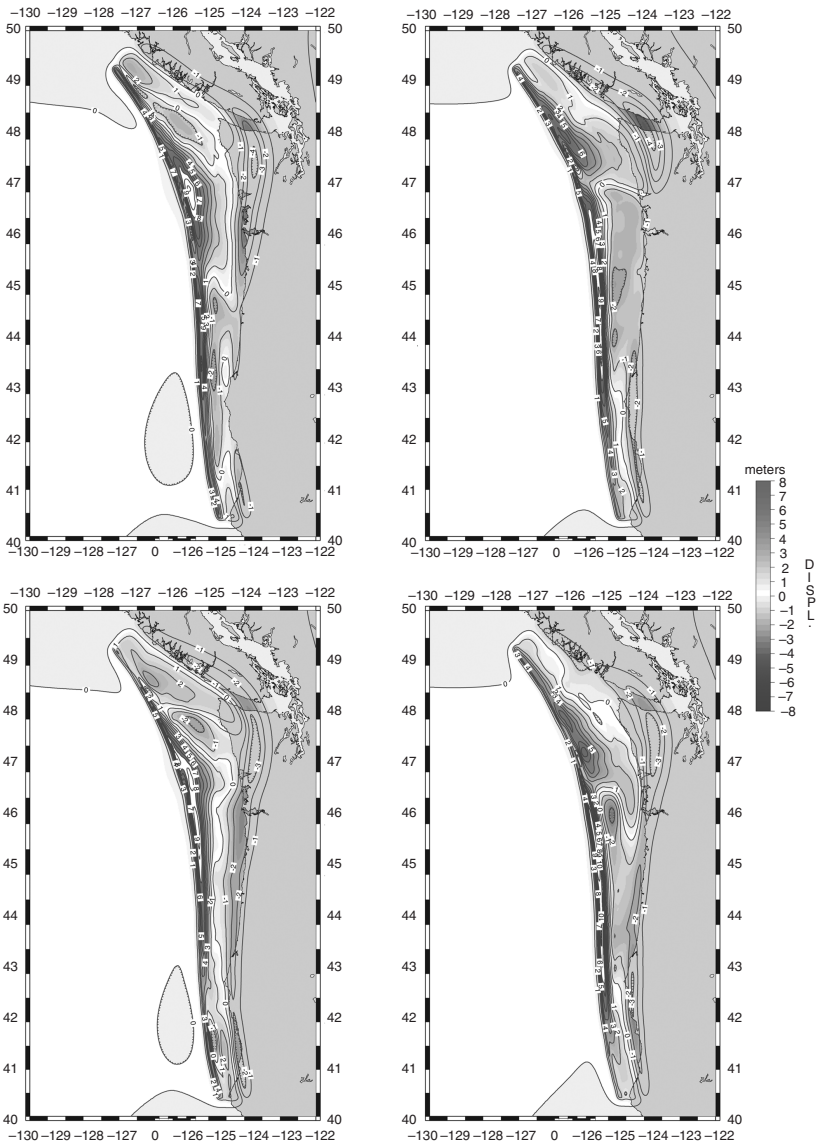

FIG. 15. Four examples of possible vertical coseismic displacement fields from slip on the Cascadia inter-plate thrust, showing a predominantly subparallel orientation of the axis of displacement with the coastline. Displacement is calculated using the static elastic displacement equations (Eqs (3) and (4)) with fractal slip (Eq. (17)) and a non-planar fault geometry (Flück *et al.*, 1997).

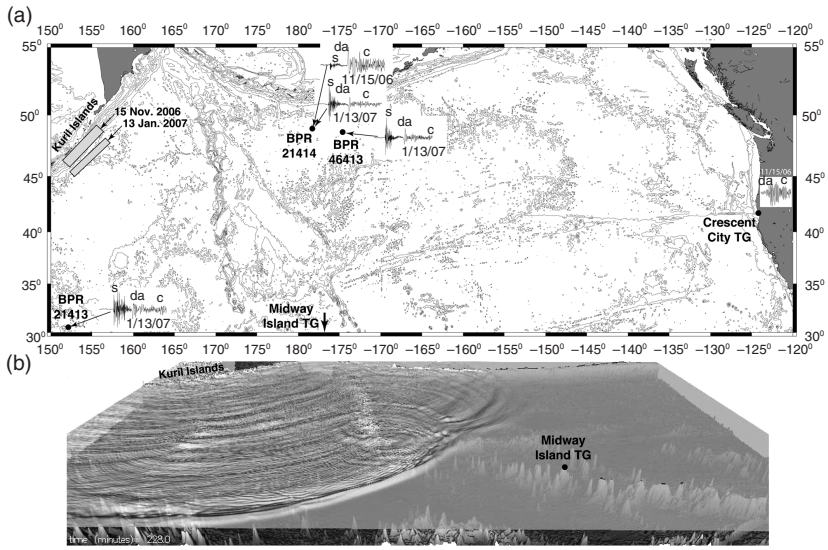

FIG. 16. (a) North Pacific map showing 15 November 2006 and 13 January 2007 Kuril earthquakes (light gray rectangles) and time-series data locations (filled circles). BPR: bottom pressure recorder. TG: tide gage. Sample detided time series indicated for both tsunamis. Arrivals: s-seismic surface waves (under-sampled), da-tsunami direct arrival, and c-tsunami coda. Bathymetric contour interval: 1 km. (b) Snapshot at 228 min. of computed tsunami wavefield from the 2006 Kuril earthquake. Perspective view to the north.

4.1. Open-ocean Propagation

HYPOTHESIS 6. *The deep-ocean far-field tsunami wavefield includes a well-developed coda caused by frequency dispersion, scattering, reflected, and refracted arrivals.*

During propagation, the tsunami wavefield gradually evolves, owing to the effects of dispersion and of reflection, scattering, and focusing from changes in bathymetry. As an example of this complexity, a snapshot of the numerically simulated tsunami wavefield in the north Pacific from the November 2006 earthquake is shown in Fig. 16b. In this section, I first examine the coda recorded from BPR time-series measurements both in terms of its amplitude distribution and its spectral content. I then review possible origins for the coda, including dispersion and scattering.

The evolution of far-field, deep-ocean waveforms has been discussed since the advent of bottom pressure recorders, particularly with regard to the effects of dispersion (e.g. see González and Kulikov (1993)). The recent 2006 and 2007 Kuril tsunamis are useful case studies since there are several available observation points along unobstructed ray paths (Fig. 16). Time series of tsunami water-level elevations (converted from pressure measurements) at these observation points are plotted in Fig. 17. It is apparent in these time series that the direct arrival phase is stable, while the coda of the time series is highly variable. The direct arrival phase, in accordance with the principle of causality, follows a least-time ray path. The coda, in contrast, is described by the combined effects of dispersion and scattering as described below.

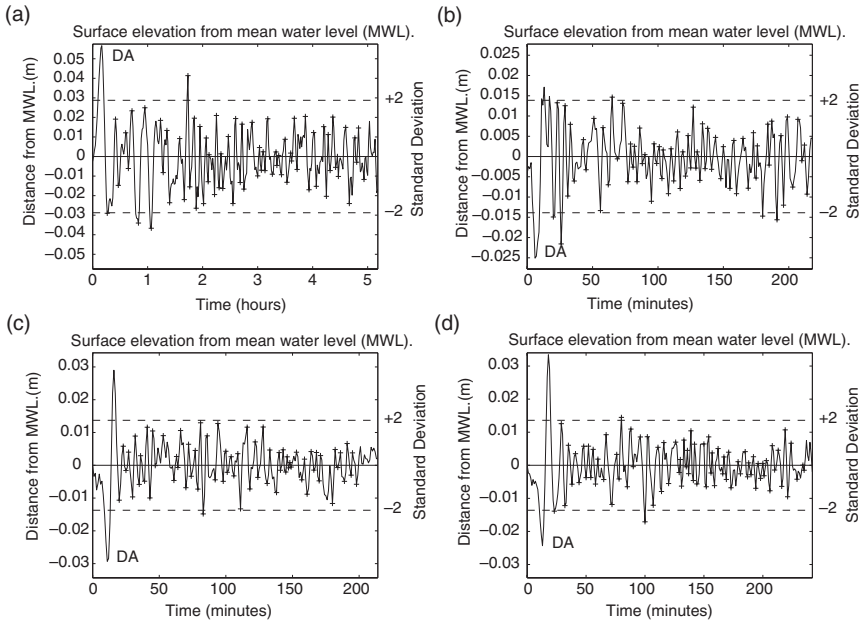

FIG. 17. Time series of tsunami bottom pressure measurements from locations indicated in Fig. 16, showing the direct arrival (DA) and the ensuing tsunami coda. Location of crest and trough amplitudes is indicated by + symbol. (a) 15 November 2006 Kuril tsunami, station 46413. (b) 13 January 2007 Kuril tsunami, station 21413. (c) 13 January 2007 Kuril tsunami, station 21414. (d) 13 January 2007 Kuril tsunami, station 46413.

The coda is typically characterized by an exponentially decaying wave envelope. Much of the analysis and theory of the seismic coda can be directly adapted to analyze the tsunami coda: a review of past research related to the seismic coda is discussed in Volume 50 of Advances in Geophysics. The envelope of tsunami amplitudes is assumed to follow an exponential decay (Mofjeld *et al.*, 2000a):

$$A_c = A_0 \sigma \exp\left[-\left(t - t_0\right)/\tau\right], \tag{27}$$

where A_0 is a constant coefficient, σ is the initial standard deviation of A_c, and τ is the e-folding decay constant. This expression is analogous to a frequency-independent (cf. van Dorn (1984)) form of energy density for the seismic coda (Aki and Chouet, 1975)), where τ is analogous to the seismic attenuation factor Q. To be consistent with the physics of the origin of the coda, I define it as commencing immediately after the first arrival, whereas Mofjeld *et al.* (2000a) chose $t_0 = 4$ hours for tsunami forecasting objectives. To estimate the coda envelope, I compute a running root mean square of the water-level elevation η (Nishigami, 1991; Nishigami and Matsumoto, 2008) and find the best-fit exponential curve. Alternatively, Mofjeld *et al.* (2000a) provided a probabilistic definition of the tsunami coda envelope based on a cumulative binomial distribution.

The initial statistical model of water-level elevations (η) within the coda is that of a time-varying Gaussian distribution (Takahara and Yomogida, 1992). The

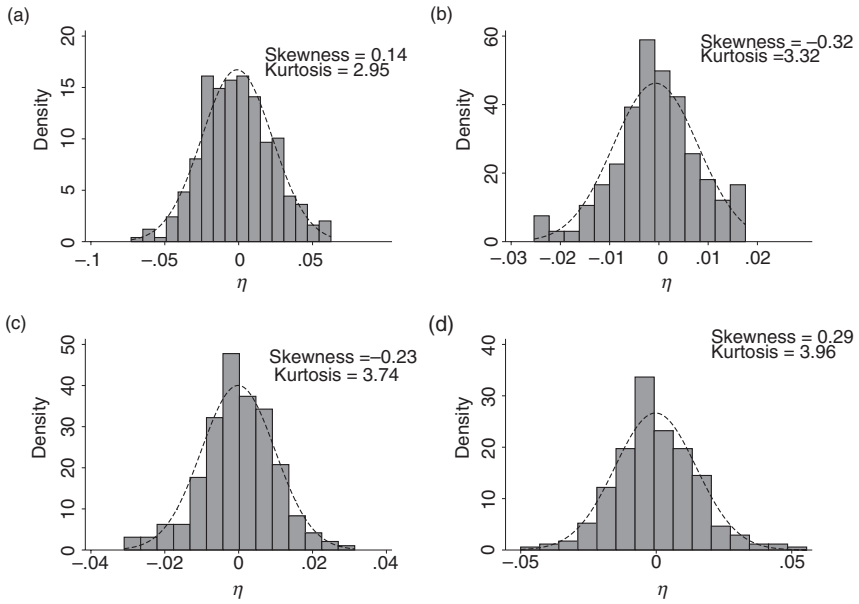

FIG. 18. Empirical density distribution of tsunami coda waves from data plotted in Fig. 17. Dashed line indicates the Gaussian distribution model.

stationary Gaussian distribution is also the canonical model for deep-water waves in a fully developed random sea (e.g. see Longuet-Higgins (1952)), though Gaussian transformations (Rychlik *et al.*, 1997) and second-order statistical models have been proposed that more accurately reflect real wind-generated waves in the ocean (e.g. see Hogben (1990); Huang *et al.* (1990); Jha and Winterstein (2000); Prevosto *et al.* (2000); Muraleedharan *et al.* (2007)). To determine whether tsunami coda waves conform to a Gaussian distribution, the detided data are first corrected for the exponential envelope decay (Eq. (27)) to simulate a stationary wave sequence, and an empirical density function is then determined (Fig. 18). The Shapiro-Wilk test for normality (Shapiro and Wilk, 1965; Stephens, 1974) indicates that Gaussian null hypothesis cannot be rejected for two of the stations (Fig. 18a and c) but can be rejected at 95% confidence for the other two stations (Fig. 18b and d).

The distribution of amplitudes corresponding to the Gaussian distribution is a Rayleigh distribution (Rayleigh, 1880). Longuet-Higgins (1952) derived this correspondence for the case of a narrow band of frequencies for ocean waves. Spectra for deep-ocean tsunami waves are shown in Fig. 19, indicating the frequency band where the tsunami energy occurs. The Rayleigh density distribution is typically given in terms of the crest-to-trough wave height (H):

$$f(H) = \frac{2H}{H_{rms}^2} \exp\left(-\frac{H^2}{H_{rms}^2}\right), \tag{28}$$

where H_{rms} is the root-mean-square wave height. For amplitudes, the distribution can be

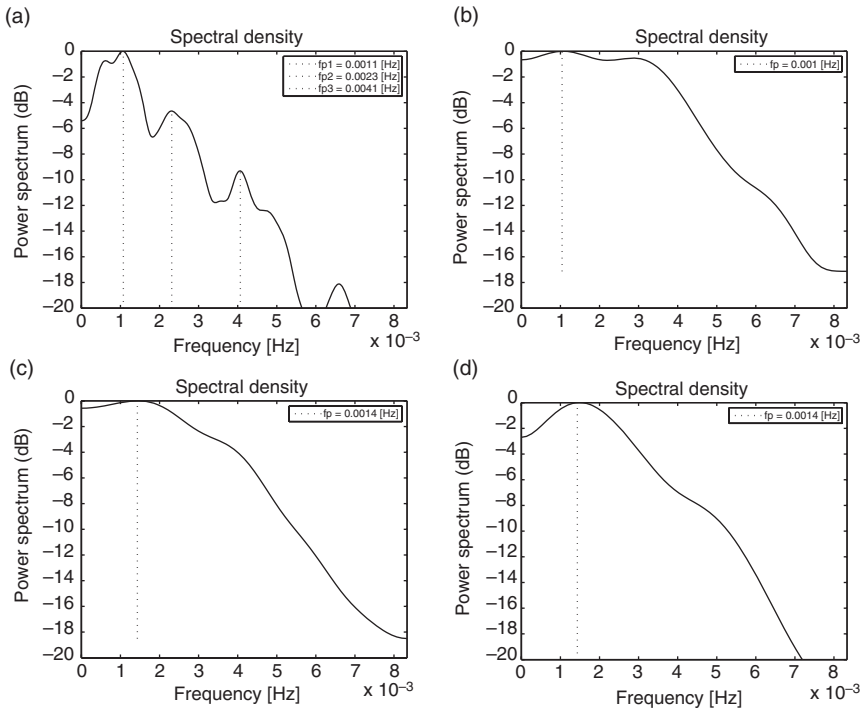

FIG. 19. Spectra of tsunami coda waves from data plotted in Fig. 17.

written as (Massel, 1996):

$$f(A) = \frac{A}{\sigma_\eta^2} \exp\left(-\frac{A^2}{2\sigma_\eta^2}\right), \tag{29}$$

where σ_η^2 is the variance of the water-level elevation time series. For a stochastic time series, definitions of wave amplitude and wave height are not necessarily straightforward. Amplitude can be defined as $A = \frac{1}{2}H$ (Longuet-Higgins, 1952) or the crest (trough) amplitude $A_c(A_t)$ can be defined as the global maximum (minimum) between successive downcrossings (Rychlik and Leadbetter, 1997) as shown in Fig. 17. In this case, $H = A_c - A_t$. For transient waves such as tsunamis, the crossings refer to the ambient, mean sea level prior to the onset of the tsunami. It should be noted that multiple local maxima and minima, defined by turning points, can exist between successive downcrossings. Statistics of these smaller oscillations are mainly of interest for fatigue analysis in wave engineering (Rychlik and Leadbetter, 1997). Shown in Fig. 20 is the empirical cumulative distribution of wave height in comparison to the corresponding Rayleigh distribution. Including the direct arrival wave height can result in a poorer fit when it is much greater than the tsunami coda wave heights (e.g. see Fig. 20d).

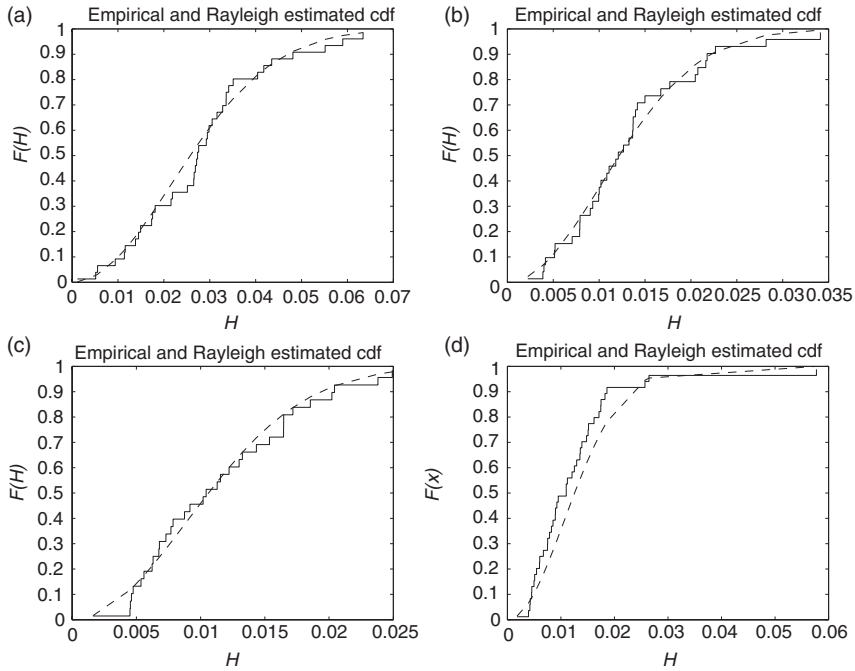

FIG. 20. Empirical cumulative distribution (solid line) of wave height (H) from data shown in Fig. 17. Dashed line indicates the Rayleigh cumulative distribution model.

Given the statistical properties of deep-ocean tsunami coda waves described above, it is instructive to examine analytic functions of dispersion and scattering derived by several authors, as described below. Analytic theory shows the evolution of the leading wave of the tsunami over large distances and the development of the dispersive coda. The first cycle of the leading wave is generally stable, allowing source characteristics to be inferred from the inversion of far-field measurements (e.g. see Fujii and Satake (2008)). To develop analytic expressions of the evolving tsunami waveform, several prescribed expressions of initial, static seafloor displacement have been considered. These are displayed in Fig. 21 along with an example from elastic displacement theory (Eqs (3) and (4)) and a spatially heterogeneous source.

In one dimension and for a constant water depth, the evolution of a linear dispersive wave from a monopole initial disturbance can be derived using the stationary-phase approximation (Jeffreys and Jeffreys, 1956; Stoker, 1957). The equation for the leading part of the wave is derived by Wu (1981) and Mei (1989) as:

$$\eta(x,t) = \frac{m}{2\rho}\,(\gamma t)^{-1/3}\,Ai\left[\frac{x-ct}{(\gamma t)^{1/3}}\right], \tag{30}$$

where m is the excess mass of the initial wave, $c = (gh)^{1/2}$, $\gamma = \frac{1}{2}ch^2$ and Ai is the Airy function. Carrier (1971) provided a specific expression for the case of a Gaussian initial

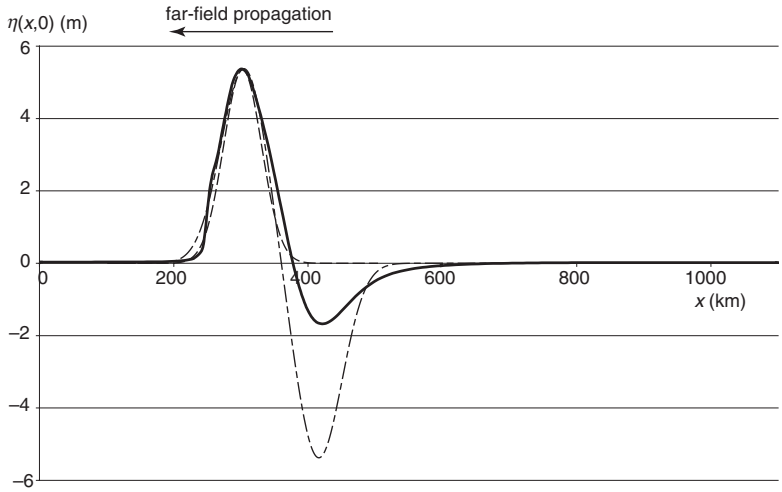

FIG. 21. Monopole (dashed) and dipole (dot-dash) analytic functions of vertical surface displacement used to specify the initial conditions for tsunami propagation. Shown for comparison is vertical displacement computed surface displacement for the 2004 Sumatra-Andaman earthquake at the latitude of Great Nicobar Island, using Chlieh *et al.*'s (2007) slip model (heavy solid line).

disturbance (Fig. 22a) and Kajiura (1963) provided expressions for other prescribed initial disturbance functions. In each case, the amplitude of the leading wave decays as a function of $t^{-1/3}$. For a dipole disturbance (Fig. 21) involving tilting of the seafloor and zero excess mass, the corresponding wave equation is (Wu, 1981; Mei, 1989)

$$\eta(x,t) = \frac{l^2}{2h}\,(\gamma t)^{-2/3}\,Ai'\left[\frac{x-ct}{(\gamma t)^{1/3}}\right], \tag{31}$$

where l is the dipole moment and $Ai'(z) \equiv \frac{\mathrm{d}}{\mathrm{d}z}Ai(z)$ (Fig. 22c). In this case, the amplitude of the leading wave decays more rapidly as a function of $t^{-2/3}$ (Fig. 22d).

For 2D propagation in constant water depth, the expressions are more complex. Tsunami radiation is particularly sensitive to fault strike (Gica *et al.*, 2007), with energy primarily focused along azimuths normal to strike. Longer rupture lengths produce a greater beaming effect along these azimuths (Ward, 1982). For a simple elliptic initial displacement in an ocean of constant depth, Kajiura (1970) indicates that the radiation pattern as a function of azimuth (ϕ) is given by

$$R(\phi) = \left[\cos^2\phi + (b/a)^2\sin^2\phi\right]^{-1}, \tag{32}$$

where a and b are the lengths of the major and minor axes. Other studies describe a more complex radiation pattern for continental shelf bathymetry (Kajiura, 1972) and in direct relation to earthquake source parameters (e.g. see Ben-Menahem and Rosenman (1972); Ward (1982); Okal (2003)). In particular, the finiteness factor of an earthquake source

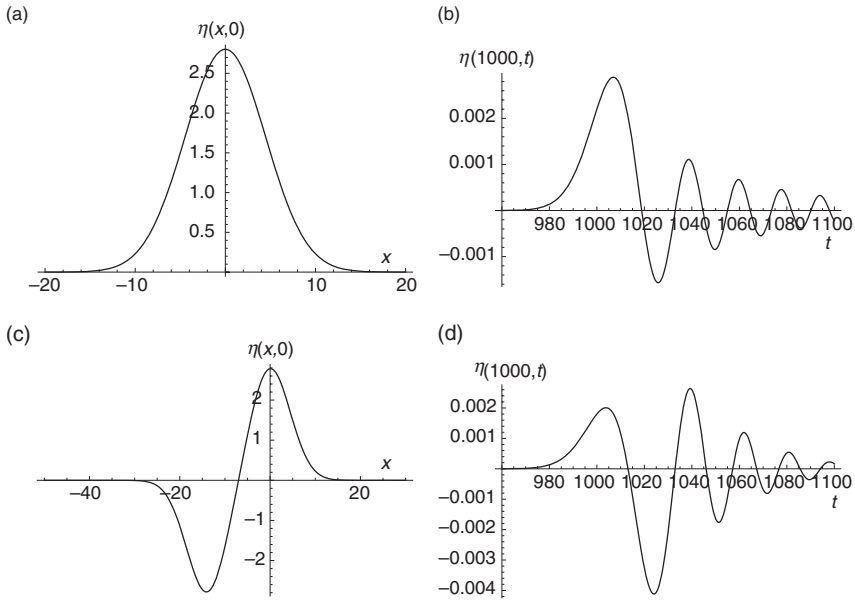

FIG. 22. For the monopole source shown in (a), the far-field time series is shown in (b). For comparison, a dipole source (c) is used to generate the far-field time series shown in (d) at the same distance (Carrier, 1971). Non-dimensional units are used.

takes the form

$$\frac{\sin X}{X}, \quad \text{where } X = \frac{1}{2}kL\left(\frac{c}{v_r} - \cos\phi\right), \tag{33}$$

which includes directivity caused by rupture propagation with speed v_r (Ben-Menahem and Rosenman, 1972; Okal, 1988). Because for tsunamis, $c \ll v_r$, the latter effect is typically small, but can be noticeable for long ruptures such as the 2004 Sumatra-Andaman earthquake (e.g. see Geist *et al.* (2007)). Figure 23 shows the radiation pattern including these effects. For elongated ruptures (Fig. 23b), note the rotation of the radiation pattern in the direction of rupture propagation and the presence of multiple, smaller lobes.

In place of the Airy wave function for the 1D case, the following function is defined by Kajiura (1963) that dictates the shape of the waveform in two horizontal dimensions:

$$T(p) = \mathrm{Re}\left[(1+i)\int_0^\infty \mathrm{e}^{\mathrm{i}(u^2 p + u^6)}\mathrm{d}u\right], \tag{34}$$

where

$$u^6 = \frac{(kh)^3}{g}\left(\frac{g}{h}\right)^{1/2} t \tag{35}$$

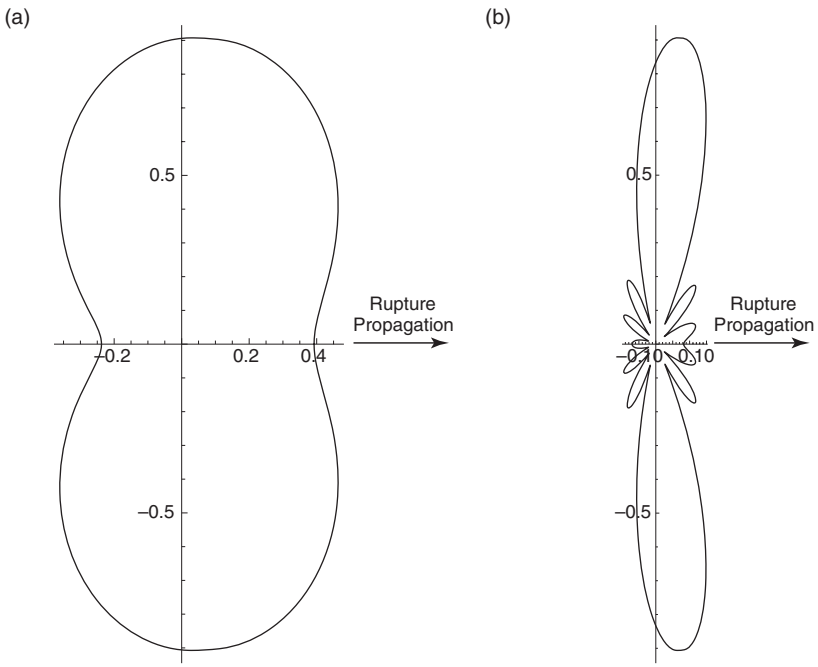

FIG. 23. Tsunami radiation pattern for a kinematic model of earthquake rupture in a constant depth ocean (Ben-Menahem and Rosenman, 1972). (a) 3:1 aspect ratio of source dimensions for typical tsunamigenic, inter-plate thrust earthquakes; (b) 12:1 aspect ratio for an elongated rupture.

and

$$p = \frac{r/h - (g/h)^{1/2}\, t}{\left[(g/h)^{1/2}\, t/6\right]^{1/3}}. \tag{36}$$

For a 2D monopole displacement, $\eta \sim -T_p$, where $T_p \equiv \frac{\mathrm{d}}{\mathrm{d}p} T(p)$. Mei (1989) examines a specific case for a 2D dipole (antisymmetric) displacement where

$$\eta(r, \theta, t = 0) = \frac{A}{a}\left(a^2 - r^2\right)^{1/2} \cos(\theta). \tag{37}$$

Using the stationary-phase approximation, Mei (1989) derived the following expression for the leading wave emanating from this displacement pattern:

$$\eta(r, \theta, t) = \cos\theta \frac{Aa^3}{16\,(2r)^{1/2}} \frac{T_{pp}}{h^{5/2}\left[(gh)^{1/2}\, t/6\right]^{5/6}}. \tag{38}$$

The amplitude for the 2D dipole case decays as a function of $t^{-4/3}$.

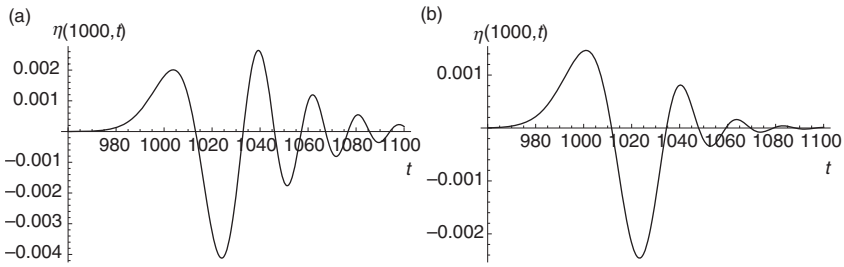

FIG. 24. Effect of source width on far-field dispersion using the Carrier (1971) dipole source (Fig. 22c). (a) $\alpha = 10$, (b) $\alpha = 30$.

To examine the effect that dispersion has on the coda, Carrier (1971) used the following Gaussian function of width α

$$\eta(x, y, t = 0) = \frac{1}{2} \frac{e^{-x^2/4\alpha}}{(\pi\alpha)^{1/2}}. \tag{39}$$

The corresponding far-field tsunami waveform near the leading part of the wavetrain is given in the non-dimensional form as

$$\eta(x, y, t) = \frac{1}{2} (2/t)^{1/3} Ai\left[x - t + \left(2\alpha^2/t\right)\right] e^{\left[\left(8\alpha^3/3t^2\right) - 2\alpha(t-x)/t\right]} \tag{40}$$

(cf. Eq. (34) above). Carrier (1971) demonstrated that dispersion increases with a decrease in the width parameter α, corresponding to a decrease in the down-dip width of the rupture zone ($\alpha \sim W \cos(\delta)$) (Fig. 24). Moreover, Carrier (1971) approximated a dipole wave with the function (Fig. 21)

$$\eta_{\text{dipole}}(x, y, t) = \eta(x, y, t) - \eta(x + b, y, t). \tag{41}$$

For a narrow source, the leading far-field waveform is characterized by a trailing peak amplitude greater than the leading peak amplitude (cf. Fig. 22).

The coda for the transoceanic tsunami wave, taken as a whole, is not only developed from the dispersion as described above, but also the effects of reflection, particularly for continental subduction zone sources (Abe, 2000), scattering, and wave trapping. The foregoing analysis demonstrates that for constant water depth, the shape of the leading wave persists in the far field. Even for irregular water depth, observations indicate that the first cycle or so of the leading wave largely remains intact from the source region, such that the far-field wave has not "forgotten" its initial conditions (Carrier, 1970, 1971). Both circular (e.g. seamounts) and linear (e.g. escarpments) irregularities can cause scattering, depending on the water depth of the scattering feature relative to the basin water depth and the wavelength of the tsunami, thus leading to an increase in the duration of the tsunami coda as demonstrated analytically by Mofjeld *et al.* (2000b, 2001) and for the 2006 Kuril tsunami in particular by Koshimura *et al.* (2008) and Kowalik *et al.* (2008). In addition

to scattering, wave trapping can occur along ridges and deflection along trenches, for the appropriate incidence angle (Chao, 1971; Mei, 1989), and focusing associated with spherically shaped irregularities may occur (Berry, 2007; Janssen *et al.*, 2008), all of which can influence the coda of the tsunami.

Analytic expressions of tsunami scattering have taken both deterministic and statistical forms. A deterministic scattering index (S) is described by Mofjeld *et al.* (2000b, 2001) that is based on the minimum transmissivity for a ridge-like topographic feature:

$$S = 1 - \frac{2\varepsilon}{1+\varepsilon^2}, \quad \text{where } \varepsilon = \left(\frac{h_1}{h_0}\right)^{1/2}. \tag{42}$$

The advantage of this type of index is that it only depends on the depth to the top of the ridge h_1 relative to the depth of the ocean floor surrounding the ridge h_0. Therefore, a scattering index map can be developed based on the known bathymetry of an ocean (Mofjeld *et al.*, 2001, 2004).

A statistical approach to tsunami scattering has been recently developed by Saito and Furumura (2009a). In this case, they treated bathymetric variations that cause scattering as a random medium (cf. Carrier (1970); Mysak (1978)), namely, that of a von Kármán autocorrelation function. The power spectral density of the bathymetry with radial wavenumber $\tilde{k}$ is given by

$$P\left(\tilde{k}\right) = \frac{4\pi\kappa\varepsilon^2 a^2}{\left(1+a^2\tilde{k}^2\right)^{\kappa+1}}, \tag{43}$$

where in this case ε is the rms value of the bathymetric variation and κ and a are the spectral decay exponent and the correlation distance, respectively. Note that this statistical model has also been used for the coseismic slip distribution on faults as described in Section 3.1. The corresponding scattering coefficient (g) derived by Saito and Furumura (2009a) as a function of azimuth about the scatterer (ϕ) and tsunami wavenumber (k) is

$$g(\phi, k) = \cos^2\phi \frac{\pi\kappa\varepsilon^2}{a} \frac{(ak)^3}{\left[1+a^2k^2\cos^2(\phi/2)\right]^{\kappa+1}}. \tag{44}$$

They indicate two end-member regimes for scattering, in terms of coda energy and attenuation coefficient: $ak \ll 1$ and $ak \gg 1$. For the first, more common, case in which the tsunami wavelength is much greater than the correlation distance, there is a symmetric radiation pattern (i.e. both back- and forward scattering given by the $\cos^2\phi$ term; see Fig. 25a) and the attenuation coefficient is independent of the power-law exponent measure of seafloor roughness (κ). For $ak = 1$, forward scattering dominates (Fig. 25b) and the attenuation coefficient is dependent on κ. Janssen *et al.* (2008) discussed spatially coherent wave interference patterns associated with forward scattering and the effect on wave statistics.

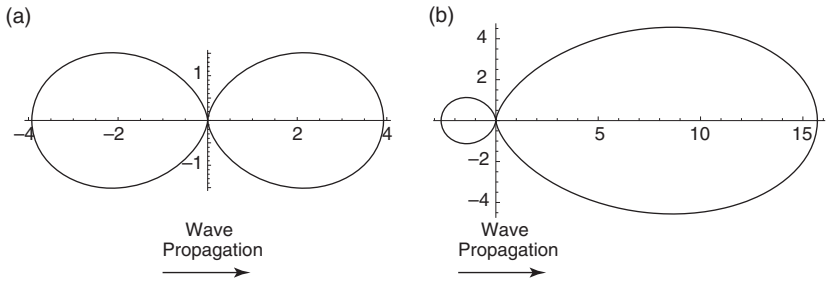

FIG. 25. Comparison of tsunami scattering radiation patterns derived by Saito and Furumura (2009a) for two cases: (a) $ak \ll 1$; (b) $ak = 1$.

4.2. Far-field Coastal Interaction

HYPOTHESIS 7. *Maximum amplitude and runup at the coast from a far-field tsunami are derived from the complex interaction of the long tsunami coda and the excitation and resonance of trapped edge waves and shelf modes.*

After the first arrival of the tsunami onshore, the shelf and coastal response greatly modifies the waveform characteristics from that observed in deep water. Coastal observations of far-field tsunamis are the result of a complex interaction between the coda developed during propagation, oblique propagation across the continental shelf, and the excitation of edge waves caused by coastline irregularities and the subsequent scattering and resonance. The result is a long coastal tsunami coda, with an e-folding time much greater than that for deep-ocean observations. I compare single-station records from tsunamis in the near-field oblique and far-field regimes and describe the observed effects based on analytic theory described in past studies.

A comparison of near-field oblique and far-field tsunami records at the Crescent City tide gage station yields information with which to evaluate Hypothesis 7. For this, I compare a near-field oblique record (1992 Cape Mendocino earthquake) (González *et al.*, 1995) with far-field records (the 2006 Kuril and 1960 Chile earthquakes) (Fig. 26). The far-field records (Fig. 26b, c) are generally more resonant (i.e. less irregular than the near-field record), possibly due to prolonged edge wave excitation and resonance from the coda arriving at the coast. For the near-field oblique case, edge waves principally emanate from the Cape Mendocino earthquake to the south, whereas edge waves excited by the far-field tsunami possibly emanate to both the north and the south from secondary sources (i.e. coastline irregularities) (cf. Munk *et al.* (1964); Guza and Davis (1974); Fuller and Mysak (1977)). However, local resonance of trapped waves is particularly strong to the south of Crescent City (Horrillo *et al.*, 2008), suggesting that the difference between the near-field oblique and far-field records is primarily caused by the longer open-ocean coda of the far-field tsunami.

Because of the oblique propagation path for the 1960 Chile tsunami, the record shown in Fig. 26c may have a large component of leaky (non-trapped) shelf modes, similar to what was observed for this tsunami in southern California (Miller *et al.*, 1962; Snodgrass *et al.*, 1962). The 2005 Crescent City tide gage record of a small tsunami generated by

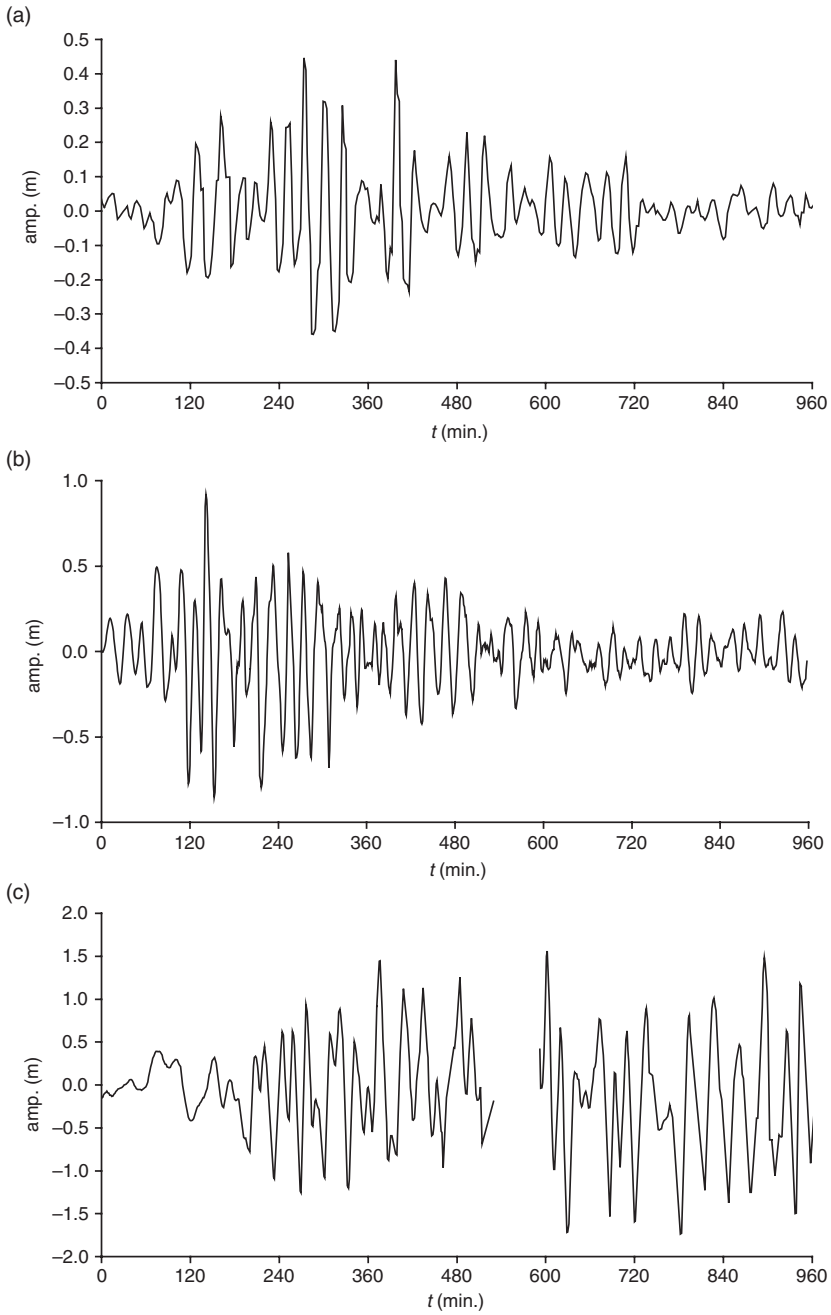

FIG. 26. Tide gage records at Crescent City for tsunamis generated by (a) a near-field oblique source, the 1992 Cape Mendocino earthquake and two far-field sources; (b) the 2006 Kuril earthquake and (c) the 1960 Chile earthquake.

a $M_w = 7.2$ strike-slip earthquake in the Gorda plate (approx. 3000 m water depth) is also explained by a larger component of leaky shelf waves compared to edge waves by Rabinovich *et al.* (2006). The strike of the 2005 Gorda plate earthquake is at a high angle to both the strike of the Cascadia inter-plate thrust (i.e. the source fault for the 1992 Cape Mendocino earthquake) and the trend of the shelf edge, suggesting predominantly oblique propagation. However the quadrupole tsunami radiation pattern for strike-slip earthquakes (González *et al.*, 1991) complicates the analysis of trapped and shelf modes for this event.

As with the deep-ocean tsunami, a test can be performed to determine whether the coastal tsunami coda can be described as a time-varying Gaussian distribution (cf. Takahara and Yomogida (1992)). As before, I examine data from the 2006 Kuril Islands tsunami for both an island station (Midway Island) and a continental station (Crescent City) (Fig. 27). Estimation of the coda envelope indicates that the *e*-folding time for Midway Island is 22 hr, consistent with the general decay law with an *e*-folding time of 22.0 ± 0.7 hr measured by van Dorn (1984) for 28 tsunami sources and various station locations in the Pacific. The empirical density distribution of water-level elevations is shown in Fig. 28. According to the Shapiro-Wilk test, the Gaussian null hypothesis cannot be rejected for either the Crescent City or the Midway Island data. However, the empirical wave heights at Midway Island conform to a Rayleigh distribution better than wave heights at Crescent City (Fig. 29), suggesting that the narrow-band assumption used in the Longuet-Higgins (1952) derivation of the Rayleigh distribution may not hold for Crescent City.

The spectra for coastal stations (Fig. 30) show a strong site response that is also apparent in the spectra of tide gage records in response to background (non-tsunami) long waves (dashed lines). Rabinovich (1997) analyzed the spectra of three events along the Hokkaido-Kuril subduction zone and determined that the local hydrodynamic response is strongly controlled by the bathymetry near the station and is the dominant signal in the spectra (see also van Dorn (1984)). Rabinovich (1997) also separated the source and site response components by calculating the spectral ratios between background and tsunami spectra and found that the dominant period of the tsunami source is consistent with the earthquake dimensions and water depth above the source (i.e. taking into account Green's law discussed in Section 3.3). Rabinovich and Thomson (2007) analyzed 45 coastal records from the 2004 Indian Ocean tsunami and found that the site response for island stations is much less apparent than that for continental stations, owing to the absence of trapped shelf waves (see also Watanabe (1972); van Dorn (1987)). Moreover Rabinovich and Thomson (2007) noted that the first arrival is typically largest for broadside stations at regional distances (cf. Fig. 9), whereas the largest arrival occurs in the tsunami coda for all other stations, which is consistent with Hypotheses 1 and 4, respectively. They noted that the deep-ocean tsunami coda "pumps" energy into the local site response controlled by the nearby bathymetry, which is consistent with Hypothesis 7.

van Dorn (1984, 1987) suggested that the coastal response is related to normal-mode forcing across the continental shelf from the open-ocean tsunami coda (with an isotropic spectra, presumably caused by mid-ocean scattering), rather than the excitation of resonant edge waves as suggested above. However, in a detailed analysis of the coastal eigenmodes near Crescent City, Horrillo *et al.* (2008) indicated that both impedance matching of the gravest shelf mode and transient edge wave modes (cf. Fuller and Mysak

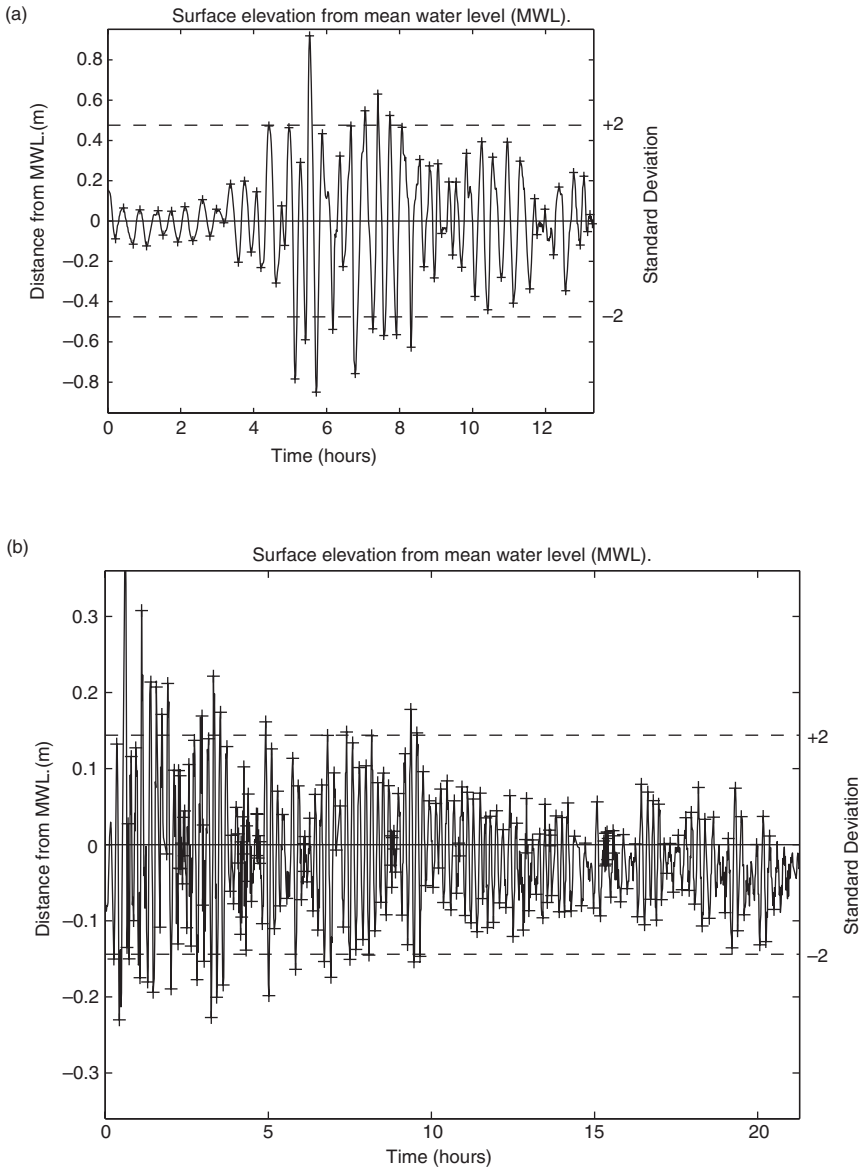

FIG. 27. Time series of tide gage measurements of the 15 November 2006 Kuril tsunami from locations indicated in Fig. 16: (a) Crescent City; (b) Midway Island. Location of crest and trough amplitudes indicated by +'s.

(1977)) contribute to the complex tide gage record. Horrillo *et al.* (2008) indicated that resonance within the Crescent City harbor does not appear to be a major factor, owing to the fact that the observed dominant periods are greater than the natural period of the

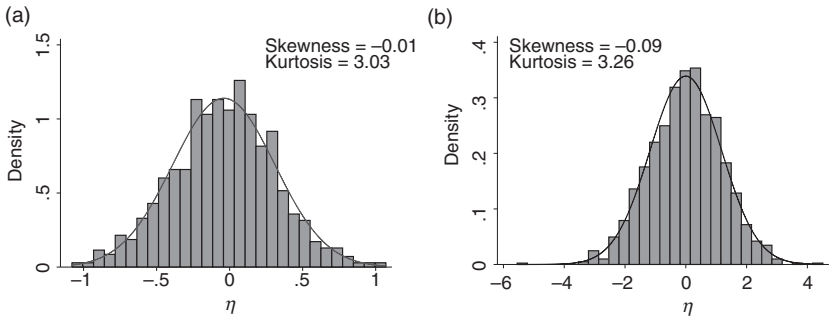

FIG. 28. Empirical density distribution of tsunami coda waves from data plotted in Fig. 27: (a) Crescent City; (b) Midway Island. Line indicates the Gaussian distribution model.

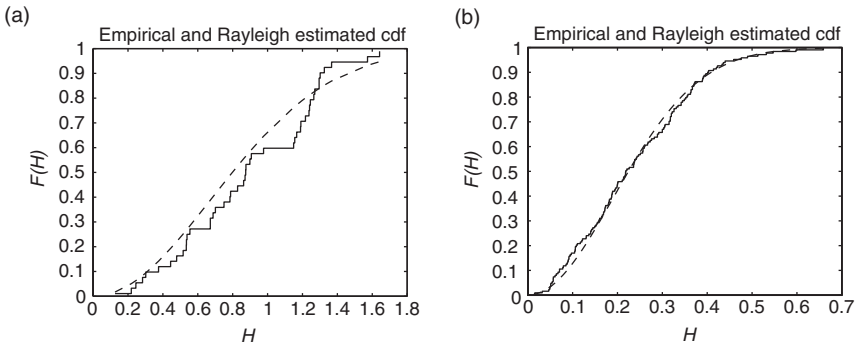

FIG. 29. Empirical cumulative distribution (solid line) of wave height (H) from the data shown in Fig. 27: (a) Crescent City; (b) Midway Island. Line indicates the Rayleigh distribution model.

harbor. (It should be noted that harbor resonance is an important component of the local site response for many other tide gage locations.) Shelf resonance has also been used to explain the persistent signal (over 2 days) in Brazil from the 2004 tsunami generated by the Sumatra-Andaman earthquake (França and de Mesquita, 2007).

Whereas the origin of edge wave development from a near-field source at the coast can be analyzed from theoretical studies (Kajiura, 1972; Ishii and Abe, 1980; Fujima *et al.*, 2000), it is less clear how edge waves are developed for far-field tsunamis. For a uniform coast line, distant tsunami waves will specularly reflect without the excitation of edge waves (i.e. Case 3 of Fujima *et al.* (2000)). For an irregular coastline, however, it has been proposed that edge waves can be excited by different mechanisms. Guza and Davis (1974) showed that nonlinear coupling of a triad composed of the incident wave and two oppositely propagating edge waves can result in an exponential growth rate of edge waves at specific frequencies. Fuller and Mysak (1977) suggested that resonant interaction of the incident wave with the wavenumber spectrum of coastal irregularities can also excite edge waves. As with edge waves developed in the near-field oblique regime, it is difficult

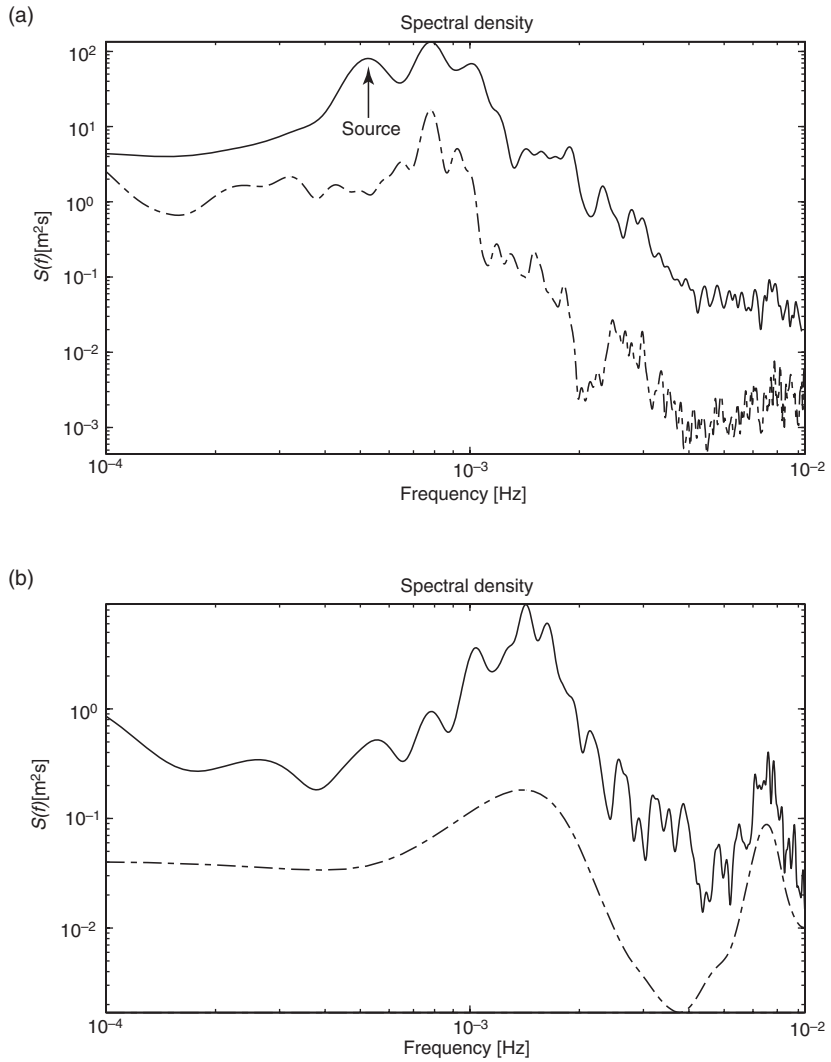

FIG. 30. Spectra of tsunami coda waves from the data plotted in Fig. 27: (a) Crescent City; (b) Midway Island. Background wave spectra are shown by a dashed line.

to trace the origin of individual phases observed on tide gage records, particularly when the incident wave has a long coda.

Far-field maximum amplitudes at the coast are particularly difficult to predict because of the interaction of the tsunami coda with the coastal response. As a notable example, Watanabe (1972) examined the maximum far-field amplitude associated with four major trans-Pacific tsunamis: those generated by 1952 Kamchatka, 1957 Aleutian, 1960 Chile, and 1964 Gulf of Alaska earthquakes. Contrary to a fundamental understanding of

attenuation during tsunami propagation (let alone the exact decay exponent provided by Eqs (31) and (38)), Watanabe (1972) indicated that the *maximum* far-field amplitude observed at coastal stations *increases* with the travel time to those stations for the 1952, 1960, and 1964 tsunamis. While one could argue that the scatter in the data does not present statistically significant results, the point remains that a simple understanding of tsunami physics in the deep ocean, such as attenuation with travel time, does not translate to similar predictions for maximum tsunami amplitudes at the coast that are associated with late arrivals from, for example, multiple trapped waves and are related to a site-specific response.

5. Summary and Discussion

5.1. Observations and Hypotheses

In this paper, past observations of tsunami events have been described according to a broad understanding of tsunami physics. For tsunami generation, the focus has been on earthquakes, owing to the frequency of occurrence of seismogenic tsunami sources and to a lack of data on tsunami generation from other sources, such as submarine landslides. The primary observation related to tsunami generation from earthquakes is spatially heterogeneous coseismic slip that is determined from the inversion of seismic waveforms. Observations relating to tsunami propagation and runup, are divided among three coastal regimes: near-field broadside, near-field oblique, and far field (Fig. 1). This division is based on the distinctly different tsunami physics that control the amplitude and timing of the maximum observed wave (Carrier, 1995).

Several working hypotheses have been presented in this paper to describe the observations, primarily relating to the amplitude (or runup) and timing of the largest tsunami wave, which are of primary interest in developing tsunami hazard assessments (e.g. see González *et al.* (in press)). In the near-field broadside regime and for a nominally regular coast, the maximum amplitude of a tsunami is most often associated with the direct arrival from the source. Accordingly, spatial heterogeneity of the source appears to have a significant effect on the spatial distribution of broadside runup. Moreover, the severity of the tsunami is dependent on the water depth overlying regions of high slip on the fault. For high slip beneath deep water, more shoaling amplification and higher tsunami runups result, as indicated, for example, by a comparison of the tsunamis generated by the 1952 and 2003 Tokachi-Oki earthquakes (Fig. 12).

In the near-field oblique regime, the maximum amplitude of a tsunami is most often associated with excited edge waves that propagate at significantly slower phase and group speeds than non-trapped modes. The details of how near-field edge waves are excited depend on the proximity of the initial wavefield to the shoreline and the orientation of initial wave crest/trough relative to the shoreline (Fujima *et al.*, 2000). Typically, the orientation of the waves for seismogenic tsunamis is subparallel to the shoreline, exciting predominantly fundamental mode edge waves, whereas for landslide tsunamis, the orientation is subnormal to the shoreline, exciting higher edge wave modes.

Finally, a tsunami coda gradually develops in the far field as a result of dispersion and scattering from bathymetric features. As the tsunami arrives at transoceanic coasts, energy from the coda is pumped into the nearshore response that includes the excitation

of edge waves, scattering from coastline irregularities, and resonance of trapped modes (e.g. see Rabinovich and Thomson (2007)). In this case, the tsunami is very persistent in time and the maximum amplitude can occur much later than the first arrival.

5.2. Statistical Descriptions

Rather than treating the evolution of tsunamis from a strictly deterministic approach, I have reviewed different statistical models that have been developed from generation through runup. Unexpected behavior of tsunamis is understood better from a statistical perspective, compared to simple deterministic models of tsunami physics (e.g. see Fig. 2). For coseismic slip, a 2D stochastic model initially developed by Andrews (1980) has been extensively used in describing slip distributions derived from seismic waveform inversions. Although in theory, statistical descriptions of runup observations can be linked to the stochastic slip model, the sparse and non-uniform nature of runup observations from post-tsunami surveys, as well as the complex nature of nearshore wave dynamics, presently preclude such a link. The log-normal model proposed by Choi *et al.* (2002, 2006) is currently the best constrained statistical description of runup distribution. The log-normal distribution (and the power-law distribution in select cases) indicates a higher likelihood of extreme runup over what would be expected from a Gaussian distribution of runup tied to the potency of the source (e.g. seismic moment).

In the far field, the observed tsunami coda can be described by an exponentially decaying Gaussian distribution of wave elevations, similar to seismic coda statistical models (e.g. see Takahara and Yomogida (1992)). For narrow-banded waves, the distribution of wave amplitudes therefore corresponds to a Rayleigh distribution. Such a model encompasses frequent observations of a delay in the arrival of the maximum amplitude phase after the first (direct) arrival. The exponential decay time is greater for nearshore observations compared to deep-ocean measurements, owing to the excitation, scattering, and resonance of edge waves and leaky shelf modes as part of the overall nearshore site response.

The statistical models used to describe tsunamis are intended to encompass possible outcomes that result from either highly complex physics (i.e. aleatory uncertainty) or for linear aspects of tsunami physics where insufficient data exist for accurately developing deterministic solutions (i.e. epistemic uncertainty). For the former, the rate- and state-friction law for fault rupture is sufficiently complex for generating multiple slip realizations for only slight differences in initial conditions, even for simple fault geometries. Real fault systems are likely to be geometrically complex (e.g. see Power and Tullis (1991)), with spatially heterogeneous pre-stress conditions and pore pressure distributions. Earthquakes with the same hypocenter and the same overall seismic moment are likely to have different slip distributions, as exemplified by the 1952 and 2003 Tokachi-Oki earthquakes (Fig. 12). Therefore, the stochastic coseismic slip model is intended to provide an ensemble of realizations representing aleatory uncertainty in understanding earthquake rupture dynamics from a probabilistic perspective. In contrast, the difficulty in accurately simulating the tsunami coda may be somewhat surprising, given that the physics of long-wave propagation is fairly well understood. It is likely that much of the coda arises from scattering in the open ocean and edge wave excitation along coasts, for which detailed bathymetry is needed. In this case, statistical models

of the far-field waveform encompass epistemic uncertainty related to the data needed to accurately simulate nearshore wave physics.

5.3. Knowledge Gaps

Our understanding of tsunami physics is far from complete, owing in part to obvious gaps in observing certain phases of tsunami evolution. With regard to tsunami generation, there are very few direct measurements of submarine landslide movement. This information is critical for estimating the constitutive parameters for landslide dynamics and the efficiency at which landslides generate tsunamis. For seismogenic tsunamis, there are also few direct measurements of coseismic vertical displacement of the seafloor, although the unique measurements stemming from the 2003 Tokachi-Oki earthquake (Mikada *et al.*, 2006), as well as many onshore case studies, suggest that elastic displacement models driven by heterogeneous coseismic slip on the fault plane are adequate. With regard to tsunami propagation, we do not have a dense spatial observation network of deep-ocean tsunami wave heights, although the network of BPR stations throughout the world's oceans is greatly expanding (Mofjeld, 2009). In addition, space-borne technology including satellite altimetry and detection of "tsunami shadows" can greatly help fill this gap (Godin, 2004; Godin *et al.*, 2009). When the tsunami arrives at the coast, we also have very little information regarding the time evolution of the runup process, although we are gaining a better understanding of this process in the field through observations of tsunami deposits combined with advanced sediment transport models (Apotsos *et al.*, 2009). There are also gaps related to a theoretical understanding of tsunami generation physics. In solid-earth physics, the outstanding question relates to the fault mechanics of tsunami earthquakes and splay fault ruptures, particularly with regard to what conditions (friction parameters, pore pressure, pre-stress conditions, etc.) are needed for these types of earthquakes to occur at very shallow depths (cf. Taylor (1998); Kame *et al.* (2003)). As data from new tsunami observation technologies are obtained and as we gain a better theoretical understanding of tsunami generation and hydrodynamic processes, scientists will have a broader perspective of what to expect when a tsunami occurs.

ACKNOWLEDGMENTS

The author gratefully acknowledges careful reading of this paper and constructive reviews by Frank González, Alex Apotsos, and the Advances in Geophysics editor, Renata Dmowska. This study could not have been performed without access to databases of tsunami observations, including the NOAA event archive of DART bottom pressure recorder data, digital tide gage records at the West Coast/Alaska Tsunami Warning Center, and analog tide gage records from the Earthquake Research Institute at the University of Tokyo. Analysis of tsunami records was performed in part using the Wave Analysis for Fatigue and Oceanography (WAFO) package developed at Lund University, Sweden (The WAFO Group, 2000). Map figures were created using Generic Mapping Tools (GMT) (Wessel and Smith, 1995).

REFERENCES

Abe, K., Ishii, H. (1987). Distribution of maximum water levels due to the Japan Sea tsunami on 26 May 1983. *J. Oceanogr. Soc. Japan* **43**, 169–182.

Abe, K., Abe, K., Tsuji, Y., Imamura, F., Katao, H., Iio, Y., Satake, K., Bourgeois, J., Noguera, E., Estrada, F. (1993). Field survey of the Nicaragua earthquake and tsunami of September 2, 1992. *Bull. Earthquake Res. Inst.* **68**, 23–70.

Abe, K. (2000). Predominance of long periods in large Pacific tsunamis. *Sci. Tsunami Hazards* **18**, 15–34.

Abercrombie, R.E., Antolik, M., Flezer, K., Ektröm, G. (2001). The 1994 Java tsunami earthquake: Slip over a subducting seamount. *J. Geophys. Res.* **106**, 6595–6607.

Aki, K., Chouet, B. (1975). Origin of coda waves: Source, attenuation, and scattering effects. *J. Geophys. Res.* **80**, 3322–3342.

Aki, K., Richards, P.G. (1980). Quantitative Seismology: Theory and Methods. W. H. Freeman and Company, San Francisco, 557 pp.

Ammon, C.J., Ji, C., Thio, H.K., Robinson, D., Ni, S., Hjorleifsdottir, V., Kanamori, H., Lay, T., Das, S., Helmberger, D., Ichinose, G., Polet, J., Wald, D. (2005). Rupture process of the 2004 Sumatra–Andaman earthquake. *Science* **308**, 1133–1139.

Ammon, C.J., Kanamori, H., Lay, T., Velasco, A.A. (2006). The 17 July 2006 Java tsunami earthquake. *Geophys. Res. Lett.* **33**, doi:10.1029/2006GL028005.

Andrews, D.J. (1980). A stochastic fault model 1. Static case. *J. Geophys. Res.* **85**, 3867–3877.

Apotsos, A., Jaffe, B., Gelfenbaum, G., Elias, E. (2009). Modeling time-varying tsunami sediment deposition, paper presented at Coastal Dynamics 2009: Impacts of Human Activities on Dynamic Coastal Processes, Tokyo, Japan, doi:10.1142/9789814282475_0037.

Archuleta, R.J. (1984). A faulting model for the 1979 Imperial Valley earthquake. *J. Geophys. Res.* **89**, 4559–4585.

Baba, T., Cummins, P.R., Hori, T. (2005). Compound fault rupture during the 2004 off the Kii Peninsula earthquake (M 7.4) inferred from highly resolved coseismic sea-surface deformation. *Earth Planets Space* **57**, 167–172.

Baba, T., Cummins, P.R., Hori, T., Kaneda, Y. (2006a). High precision slip distribution of the 1944 Tonankai earthquake inferred from tsunami waveforms: Possible slip on a splay fault. *Tectonophys.* **426**, 119–134.

Baba, T., Hirata, K., Hori, T., Sakaguchi, H. (2006b). Offshore geodetic data conducive to the estimation of the afterslip distribution following the 2003 Tokachi–Oki earthquake. *Earth Planet. Sci. Lett.* **241**, 281–292.

Banerjee, P., Pollitz, F.F., Nagarajan, B., Bürgmann, R. (2007). Coseismic slip distributions of the 26 December 2004 Sumatra–Andaman and 28 March 2005 Nias earthquake from GPS static offsets. *Bull. Seismol. Soc. Am.* **97(1A)**, S86–S102.

Baptista, A.M., Priest, G.R., Murty, T.S. (1993). Field survey of the 1992 Nicaragua tsunami. *Marine Geodesy* **16**, 169–203.

Beeler, N.M., Tullis, T.E., Weeks, J.D. (1994). The roles of time and displacement in the evolution effect in rock friction. *Geophys. Res. Lett.* **21**, 1987–1990.

Ben-Menahem, A., Rosenman, M. (1972). Amplitude patterns of tsunami waves from submarine earthquakes. *J. Geophys. Res.* **77**, 3097–3128.

Ben-Zion, Y., Rice, J.R. (1997). Dynamic simulations of slip on a smooth fault in an elastic solid. *J. Geophys. Res.* **102**, 17,771–717,784.

Bent, A.L. (1995). A complex double-couple source mechanism for the Ms 7.2 1929 Grand Banks earthquake. *Bull. Seismol. Soc. Am.* **85**, 1003–1020.

Beresnev, I.A. (2003). Uncertainties in finite-fault slip inversions: To what extent to believe? (A critical review). *Bull. Seismol. Soc. Am.* **93**, 2445–2458.

Berge, C., Gariel, J.C., Bernard, P. (1998). A very broad-band stochastic source model used for near source strong motion prediction. *Geophys. Res. Lett.* **25**, 1063–1066.

Berry, M.V. (2007). Focused tsunami waves. *Proc. R. Soc. Lond. A* **463**, 3055–3071.

Bhat, H.S., Olives, M., Dmowska, R., Rice, J.R. (2007). Role of fault branches in earthquake rupture dynamics. *J. Geophys. Res.* **112**, doi:10.1029/2007JB005027.

Bilek, S.L., Lay, T. (1999). Rigidity variations with depth along interplate megathrust faults in subduction zones. *Nature* **400**, 443–446.

Bilek, S.L., Lay, T. (2000). Depth dependent rupture properties in circum-Pacific subduction zones. In: Rundle, J.B., et al. (Eds.), GeoComplexity and the Physics of Earthquakes. American Geophysical Union, Washington, D.C, pp. 165–186.

Bilek, S.L., Lay, T. (2002). Tsunami earthquakes possibly widespread manifestations of frictional conditional stability. *Geophys. Res. Lett.* **29**, doi:10.1029/2002GL015215.

Bilek, S.L. (2007). Using earthquake rupture variations along the Sumatra–Andaman subduction system to examine fault zone variations. *Bull. Seismol. Soc. Am.* **97**, S62–S70.

Bird, P., Kagan, Y.Y. (2004). Plate-tectonic analysis of shallow seismicity: Apparent boundary width, beta-value, corner magnitude, coupled lithosphere thickness, and coupling in 7 tectonic settings. *Bull. Seismol. Soc. Am.* **94**, 2380–2399.

Borrero, J.C. (2001). Changing field data gives better model results: An example from Papua New Guinea, paper presented at International Tsunami Symposium 2001, Seattle, Washington, pp. 397–405.

Brodsky, E.E., Gordeev, E., Kanamori, H. (2003). Landslide basal friction as measured by seismic waves. *Geophys. Res. Lett.* **30**, doi:10.1029/2003GL018485.

Carrier, G.F., Greenspan, H.P. (1958). Water waves of finite amplitude on a sloping beach. *J. Fluid Mech.* **4**, 97–109.

Carrier, G.F. (1970). Stochastically driven dynamical systems. *J. Fluid Mech.* **44**, 249–264.

Carrier, G.F. (1971). The dynamics of tsunamis. In: Reid, W.H. (Ed.), Mathematical Problems in the Geophysical Sciences. American Mathematical Society, Providence, Rhode Island, pp. 157–187.

Carrier, G.F. (1995). On-shelf tsunami generation and coastal propagation. In: Tsuchiya, Y., Shuto, N. (Eds.), Tsunami: Progress in Prediction, Disaster Prevention and Warning. Kluwer, Dordrecht, The Netherlands, pp. 1–20.

Carrier, G.F., Wu, T.T., Yeh, H. (2003). Tsunami run-up and draw-down on a plane beach. *J. Fluid Mech.* **475**, 79–99.

Cattin, R., Briole, P., Lyon-Caen, H., Bernard, P., Pinettes, P. (1999). Effects of superficial layers on coseismic displacements for a dip-slip fault and geophysical implications. *Geophys. J. Int.* **137**, 149–158.

Chao, Y.Y. (1971). An asymptotic evaluation of the wave field near a smooth caustic. *J. Geophys. Res.* **76**, 7401–7408.

Chen, Q., Kirby, J.T., Dalrymple, R.A., Kennedy, A.B., Chawla, A. (2000). Boussinesq modeling of wave transformation, breaking, and runup: II. 2D. *Journal of Waterway, Port, Coastal, and Ocean Engineering* **126**, 48–56.

Chlieh, M., Avouac, J.P., Hjorleifsdottir, V., Song, T.A., Ji, C., Sieh, K., Sladen, A., Hebert, H., Prawirodirdjo, L., Bock, Y., Galetzka, J. (2007). Coseismic slip and afterslip of the great (Mw 9.15) Sumatra–Andaman earthquake of 2004. *Bull. Seismol. Soc. Am.* **97(1A)**, S152–S173.

Choi, B.H., Pelinovsky, E., Ryabov, I., Hong, S.J. (2002). Distribution functions of tsunami wave heights. *Nat. Haz.* **25**, 1–21.

Choi, B.H., Hong, S.J., Pelinovsky, E. (2006). Distribution of runup heights of the December 26, 2004 tsunami in the Indian Ocean. *Geophys. Res. Lett.* **33**, doi:10.1029/2006GL025867.

Coussot, P., Meunier, M. (1996). Recognition, classification and mechanical description of debris flows. *Earth-Sci. Rev.* **40**, 209–227.

Coussot, P. (1997). Mudflow Rheology and Dynamics. A. A. Balkema, Rotterdam, 255 pp.

Coussot, P., Laigle, D., Arattano, M., Deganutti, A., Marchi, L. (1998). Direct determination of rheological characteristics of debris flow. *J. Hydraulic Eng.* **124**, 865–868.

Cummins, P.R., Kaneda, Y. (2000). Possible splay fault slip during the 1946 Nankai earthquake. *Geophys. Res. Lett.* **27** (17), 2725–2728.

Dahlen, F.A. (1993). Single-force representation of shallow landslide sources. *Bull. Seismol. Soc. Am.* **83**, 130–143.

Dahlen, F.A., Tromp, J. (1998). Theoretical Global Seismology. Princeton University Press, Princeton, New Jersey, 1025 pp.

Dengler, L., Uslu, B., Barberopoulou, A., Yim, S.C., Kelly, A. (2009). The November 15, 2006 Kuril Islands-generated tsunami in Crescent City, California. *Pure Appl. Geophys.* **166**, 37–53.

Dieterich, J.H. (1979). Modeling of rock friction. Part 1. Experimental results and constitutive equations. *J. Geophys. Res.* **84**, 2161–2168.

Dieterich, J.H. (1995). Earthquake simulations with time-dependent nucleation and long-range interactions. *Nonlinear Process. Geophys.* **2**, 109–120.

Dieterich, J.H. (2007). Applications of rate- and state-dependent friction to models of fault slip and earthquake occurrence. In: Kanamori, H. (Ed.), Treatise on Geophysics. Elsevier, pp. 107–129.

Dmowska, R., Kostrov, B.V. (1973). A shearing crack in a semi-space under plane strain conditions. *Arch. Mech.* **25**, 421–440.

Dmowska, R., Rice, J.R. (1986). Fracture theory and its seismological applications. In: Teisseyre, R. (Ed.), Continuum Theories in Solid Earth Physics. PWN-Polish Scientific Publishers, Warsaw, pp. 187–255.

Dmowska, R., Rice, J.R., Lovison, L.C., Josell, D. (1988). Stress transfer and seismic phenomena in coupled subduction zones during the earthquake cycle. *J. Geophys. Res.* **93**, 7869–7884.

Elverhøi, A., Issler, D., De Blasio, F.V., Ilstad, T., Harbitz, C.B., Gauer, P. (2005). Emerging insights into the dynamics of submarine debris flows. *Natural Hazards and Earth System Sciences* **5**, 633–648.

Engdahl, E.R., Dewey, J.W., Fujita, K. (1982). Earthquake location in island arcs. *Phys. Earth Planet. Int.* **30**, 145–156.

Farreras, S.F. (2000). Post-tsunami field survey procedures: An outline. *Nat. Haz.* **21**, 207–214.

Fernández-Nieto, E.D., Bouchut, F., Bresch, D., Castro, M.J., Diaz, A., Mangeney (2008). A new Savage-Hutter type model for submarine avalanches and generated tsunami. *J. Comput. Phys.* **227**, 7720–7754.

Fine, I.V., Rabinovich, A.B., Bornhold, B.D., Thomson, R., Kulikov, E.A. (2005). The Grand Banks landslide-generated tsunami of November 18, 1929: preliminary analysis and numerical modeling. *Mar. Geol.* **215**, 45–57.

Flück, P., Hyndman, R.D., Wang, K. (1997). Three-dimensional dislocation model for great earthquakes of the Cascadia subduction zone. *J. Geophys. Res.* **102**, 20,539–20,550.

França, C.A.S., de Mesquita, A.R. (2007). The December 26th 2004 tsunami recorded along the southeastern coast of Brazil. *Nat. Haz.* **40**, 209–222.

Frankel, A.D. (1991). High-frequency spectral falloff of earthquakes, fractal dimension of complex rupture, b value, and the scaling of strength on faults. *J. Geophys. Res.* **96**, 6291–6302.

Freund, L.B., Barnett, D.M. (1976). A two-dimensional analysis of surface deformation due to dip-slip faulting. *Bull. Seismol. Soc. Am.* **66**, 667–675.

Fujii, Y., Satake, K. (2007). Tsunami source of the 2004 Sumatra–Andaman earthquake inferred from tide gauge and satellite data. *Bull. Seismol. Soc. Am.* **97**, S192–S207.

Fujii, Y., Satake, K. (2008). Tsunami sources of the November 2006 and January 2007 Great Kuril earthquakes. *Bull. Seismol. Soc. Am.* **98**, 1559–1571.

Fujima, K., Dozono, R., Shigemura, T. (2000). Generation and propagation of tsunami accompanying edge waves on a uniform shelf. *Coastal Eng. J.* **42**, 211–236.

Fukao, Y. (1979). Tsunami earthquakes and subduction processes near deep-sea trenches. *J. Geophys. Res.* **84**, 2303–2314.

Fukuyama, E. (2009). Fault-zone Properties and Earthquake Rupture Dynamics. Elsevier, Inc, London, 336 pp.

Fuller, J.D., Mysak, L.A. (1977). Edge waves in the presence of an irregular coastline. *J. Phys. Oceanogr.* **7**, 846–855.

Geist, E.L. (1999). Local tsunamis and earthquake source parameters. *Adv. Geophys.* **39**, 117–209.

Geist, E.L., Dmowska, R. (1999). Local tsunamis and distributed slip at the source. *Pure Appl. Geophys.* **154**, 485–512.

Geist, E.L., Bilek, S.L. (2001). Effect of depth-dependent shear modulus on tsunami generation along subduction zones. *Geophys. Res. Lett.* **28** (7), 1315–1318.

Geist, E.L. (2002). Complex earthquake rupture and local tsunamis. *J. Geophys. Res.* **107**, doi:10.1029/2000JB000139.

Geist, E.L., Yoshioka, S. (2004). Effect of structural heterogeneity and slip distribution on coseismic vertical displacement from rupture on the seattle fault. Open-File Report 2004-1010, U.S. Geological Survey.

Geist, E.L., Bilek, S.L., Arcas, D., Titov, V.V. (2006). Differences in tsunami generation between the December 26, 2004 and March 28, 2005 Sumatra earthquakes. *Earth Planets Space* **58**, 185–193.

Geist, E.L., Titov, V.V., Arcas, D., Pollitz, F.F., Bilek, S.L. (2007). Implications of the December 26, 2004 Sumatra–Andaman earthquake on tsunami forecast and assessment models for great subduction zone earthquakes. *Bull. Seismol. Soc. Am.* **97**, S249–S270.

Geist, E.L., Lynett, P.J., Xu, J.P. (2009a). Re-examination of the Monterey Bay tsunami triggered by the 1989 Loma Prieta earthquake [abs.]. *Seismol. Res. Lett.* **80**, 334.

Geist, E.L., Parsons, T., ten Brink, U.S., Lee, H.J. (2009b). Tsunami Probability. In: Bernard, E.N., Robinson, A.R. (Eds.), In: The Sea, Vol. 15, Harvard University Press, Cambridge, Massachusetts, pp. 93–135.

Geller, R.J. (1976). Scaling relations for earthquake source parameters and magnitudes. *Bull. Seismol. Soc. Am.* **66**, 1501–1523.

Gica, E., Teng, M.H., Liu, P.L.-F., Titov, V.V., Zhou, H. (2007). Sensitivity analysis of source parameters for earthquake-generated distant tsunamis. *Journal of the Waterways and Harbors Division, A.S.C.E.* **133**, 429–441.

Godin, O.A. (2004). Air-sea interaction and feasibility of tsunami detection in the open ocean. *J. Geophys. Res.* **109**, doi:10.1029/2003JC002030.

Godin, O.A., Irisov, V.G., Leben, R.R., Hamlington, B.D., Wick, G.A. (2009). Variations in sea surface roughness induced by the 2004 Sumatra–Andaman tsunami. *Natural Hazards and Earth System Sciences* **9**, 1135–1147.

Golovachev, E.V., Kochergin, I.E., Pelinovsky, E.N. (1992). The effect of the Airy phase during propagation of edge waves. *Soviet J. Phys. Oceanogr.* **3**, 1–7.

González, F.I., Mader, C.L., Eble, M.C., Bernard, E.N. (1991). The 1987–88 Alaskan Bight tsunamis: Deep ocean data and model comparisons. *Nat. Haz.* **4**, 119–139.

González, F.I., Kulikov, Y.A. (1993). Tsunami dispersion observed in the deep ocean. In: Tinti, S. (Ed.), Tsunamis in the World. Kluwer Academic Publishers, Dordrecht, The Netherlands, pp. 7–16.

González, F.I., Satake, K., Boss, E.F., Mofjeld, H.O. (1995). Edge wave and non-trapped modes of the 25 April 1992 Cape Mendocino tsunami. *Pure Appl. Geophys.* **144**, 409–426.

González, F.I., Geist, E.L., Jaffe, B.E., Kânoglu, U., Mofjeld, H.O., Synolakis, C.E., Titov, V.V., Arcas, D., Bellomo, D., Carlton, D., Horning, T.S., Johnson, J., Newman, J.C., Parsons, T., Peters, R., Peterson, C., Priest, G.R., Venturato, A.J., Weber, J., Wong, F., Yalciner, A.C. Probabilistic tsunami hazard assessment at Seaside, Oregon for near- and far-field seismic sources, *J. Geophys. Res.* (in press).

Greenberg, D.A., Dupont, D., Lyard, F.H., Lynch, D.R., Werner, F.E. (2007). Resolution issues in numerical models of ocean and coastal circulation. *Cont. Shelf Res.* **27**, 1317–1343.

Guatteri, M., Mai, P.M., Beroza, G.C. (2004). A pseudo-dynamic approximation to dynamic rupture models for strong ground motion prediction. *Bull. Seismol. Soc. Am.* **94**, 2051–2063.

Guza, R.T., Davis, R.E. (1974). Excitation of edge waves by waves incident on a beach. *J. Geophys. Res.* **79**, 1285–1129.

Hammack, J.L. (1973). A note on tsunamis: Their generation and propagation in an ocean of uniform depth. *J. Fluid Mech.* **60**, 769–799.

Hanks, T.C. (1979). b values and $\omega^{-\gamma}$ seismic source models: Implications for tectonic stress variations along active crustal fault zones and the estimation of high-frequency strong ground motion. *J. Geophys. Res.* **84**, 2235–2242.

Hartzell, S.H., Heaton, T.H. (1985). Teleseismic time functions for large, shallow, subduction zone earthquakes. *Bull. Seismol. Soc. Am.* **75**, 965–1004.

Hashimoto, M., Choosakul, N., Hashizume, M., Takemoto, S., Takiguchi, H., Fukuda, Y., Fujimore, K. (2006). Crustal deformations associated with the great Sumatra–Andaman earthquake deduced from continuous GPS observation. *Earth Planets Space* **58**, 127–139.

Haskell, N.A. (1964). Total energy and energy spectral density of elastic wave radiation from propagating faults. *Bull. Seismol. Soc. Am.* **54**, 1811–1841.

Heki, K., Tamura, Y. (1997). Short term afterslip in the 1994 Sanriku–Haruka–Oki earthquake. *Geophys. Res. Lett.* **24**, 3285–3288.

Herrero, A., Bernard, P. (1994). A kinematic self-similar rupture process for earthquakes. *Bull. Seismol. Soc. Am.* **84**, 1216–1228.

Hirata, K., Aoyagi, M., Mikada, H., Kawaguchi, K., Kaiho, Y., Iwase, R., Morita, S., Fujisawa, I., Sugioka, H., Mitsuzawa, K., Suyehiro, K., Kinoshita, H. (2002). Real-time geophysical measurements on the deep seafloor using submarine cable in the southern Kuril subduction zone. *IEEE J. Ocean. Eng.* **27**, 170–181.

Hirata, K., Geist, E.L., Satake, K., Tanioka, Y., Yamaki, S. (2003). Slip distribution of the 1952 Tokachi–Oki earthquake (M 8.1) along the Kuril Trench deduced from tsunami waveform inversion. *J. Geophys. Res.* **108**, doi:10.1029/2002JB001976.

Hirata, K., Tanioka, Y., Satake, K., Yamaki, S., Geist, E.L. (2004). The tsunami source area of the 2003 Tokachi–Oki earthquake estimated from tsunami travel times and its relationship to the 1952 Tokachi–Oki earthquake. *Earth Planets Space* **56**, 367–372.

Hirata, K., Satake, K., Tanioka, Y., Kuragano, T., Hasegawa, Y., Hayashi, Y., Hamada, M. (2006). The 2004 Indian Ocean tsunami: Tsunami source model from satellite altimetry. *Earth Planets Space* **58**, 195–201.

Hisada, Y. (2000). A theoretical omega-square model considering the spatial variation in slip and rupture velocity. *Bull. Seismol. Soc. Am.* **90**, 387–400.

Hisada, Y. (2001). A theoretical omega-square model considering the spatial variation in slip and rupture velocity. Part 2: Case for a two-dimensional source model. *Bull. Seismol. Soc. Am.* **91**, 651–666.

Hogben, N. (1990). Long term wave statistics. In: Le Méhauté, B., Hanes, D.M. (Eds.), Ocean Engineering Science. John Wiley & Sons, New York, pp. 293–333.

Horrillo, J., Knight, W., Kowalik, Z. (2008). Kuril Islands tsunami of November 2006: 2. Impact at Crescent City by local enhancement. *J. Geophys. Res.* **113**, doi:10.1029/2007JC004404.

Huang, N.E., Tung, C.C., Long, S.R. (1990). The probability structure of the ocean surface. In: Le Méhauté, B., Hanes, D.M. (Eds.), Ocean Engineering Science. John Wiley & Sons, New York, pp. 335–366.

Hughes Clarke, J.E. (1990). Late stage slope failure in the wake of the 1929 Grand Banks earthquake. *Geo-Marine Letters* **10**, 69–79.

Hungr, O., Evans, S.G., Bovis, M.J., Hutchinson, J.F. (2001). A review of the classification of landslides of the flow type. *Environ. Eng. Geosci.* **7**, 221–238.

Ichinose, G., Somerville, P., Thio, H.K., Graves, R., O'Connell, D. (2007). Rupture process of the 1964 Prince William Sound, Alaska, earthquake from the combined inversion of seismic, tsunami, and geodetic data. *J. Geophys. Res.* **112**, doi:10.1029/2006JB004728.

Ihmlé, P.F. (1996a). Monte Carlo slip inversion in the frequency domain: Application to the 1992 Nicaragua slow earthquakes. *Geophys. Res. Lett.* **23**, 913–916.

Ihmlé, P.F. (1996b). Frequency-dependent relocation of the 1992 Nicaragua slow earthquake: An empirical Green's function approach. *Geophys. J. Int.* **127**, 75–85.

Imran, J., Parker, G., Locat, J., Lee, H. (2001). A 1-D numerical model of muddy subaqueous and subaerial debris flows. *J. Hydraulic Eng.* **127**, 959–958.

Ishii, H., Abe, K. (1980). Propagation of tsunami on a linear slope between two flat regions. Part I edge wave. *J. Phys. Earth* **28**, 531–541.

Ishii, M., Shearer, P.M., Houston, H., Vidale, J.E. (2005). Extent, duration and speed of the 2004 Sumatra–Andaman earthquake imaged by the Hi-Net array. *Nature* **435**, 933–936.

Iverson, R.M., Denlinger, R.P. (2001). Flow of variably fluidized granular masses across three-dimensional terrain 1. Coulomb mixture theory. *J. Geophys. Res.* **106**, 537–552.

Janssen, T.T., Herbers, T.H.C., Battjes, J.A. (2008). Evolution of ocean wave statistics in shallow water: Refraction and diffraction over seafloor topography. *J. Geophys. Res.* **113**, doi:10.1029/2007JC004410.

Jeffreys, H., Jeffreys, B.S. (1956). Methods of Mathematical Physics. Third Edition, Cambridge University Press, Cambridge, England, 714 pp.

Jha, A.K., Winterstein, S.R. (2000). Nonlinear random ocean waves: Prediction and comparison with data, paper presented at Proceedings of the ETCE/OMAE2000 Joint Conference: Energy for the New Millennium, ASME, New Orleans, Louisiana, pp. 1–12.

Ji, C., Wald, D.J., Helmberger, D.V. (2002). Source description of the 1999 Hector Mine, California, earthquake, Part I: Wavelet domain inversion theory and resolution analysis. *Bull. Seismol. Soc. Am.* **92**, 1192–1207.

Jiang, L., Leblond, P.H. (1993). Numerical modeling of an underwater Bingham plastic mudslide and the waves which it generates. *J. Geophys. Res.* **98**, 10,303–310,317.

Johnson, J.M., Satake, K., Holdahl, S.R., Sauber, J. (1996). The 1964 Prince William Sound earthquake: Joint inversion of tsunami and geodetic data. *J. Geophys. Res.* **101**, 523–532.

Kajiura, K. (1963). The leading wave of a tsunami. *Bull. Earthquake Res. Inst.* **41**, 535–571.

Kajiura, K. (1970). Tsunami source, energy and the directivity of wave radiation. *Bull. Earthquake Res. Inst.* **48**, 835–869.

Kajiura, K. (1972). The directivity of energy radiation of the tsunami generated in the vicinity of a continental shelf. *J. Oceanogr. Soc. Japan* **28**, 260–277.

Kame, N., Rice, J.R., Dmowska, R. (2003). Effects of prestress state and rupture velocity on dynamic fault branching. *J. Geophys. Res.* **108(B5)**, ESE 13-11 - 13-21.

Kanamori, H. (1972). Mechanism of tsunami earthquakes. *Phys. Earth Planet. Int.* **6**, 346–359.

Kanamori, H., Given, J.W., Lay, T. (1984). Analysis of seismic body waves excited by the Mount St. Helens eruption of May 18, 1980. *J. Geophys. Res.* **89**, 1856–1866.

Kanamori, H., Kikuchi, M. (1993). The 1992 Nicaragua earthquake: A slow earthquake associated with subducted sediments. *Nature* **361**, 714–716.

Kanamori, H., Brodsky, E.E. (2004). The physics of earthquakes. *Rep. Prog. Phys.* **67**, 1429–1496.

Kanoglu, U., Synolakis, C.E. (1998). Long wave runup on piecewise linear topographies. *J. Fluid Mech.* **374**, 1–28.

Kennedy, A.B., Chen, Q., Kirby, J.T., Dalrymple, R.A. (2000). Boussinesq modeling of wave transformation, breaking and runup: I. one dimension. *Journal of Waterway, Port, Coastal, and Ocean Engineering* **126**, 39–47.

Kikuchi, M., Kanamori, H. (1991). Inversion of complex body waves–III. *Bull. Seismol. Soc. Am.* **81**, 2335–2350.

Kisslinger, C. (1993). Seismicity in subduction zones from local and regional network observations. *Pure Appl. Geophys.* **140**, 257–285.

Koshimura, S., Hayashi, Y., Munemoto, K., Imamura, F. (2008). Effect of the Emperor seamounts on trans-oceanic propagation of the 2006 Kuril Island earthquake tsunami. *Geophys. Res. Lett.* **35**, doi:10.1029/2007GL032129.

Kowalik, Z., Horrillo, J., Knight, W., Logan, T. (2008). Kuril Islands tsunami of November 2006: 1. Impact at Crescent City by distant scattering. *J. Geophys. Res.* **113**, doi:10.1029/2007JC004402.

Kreemer, C., Holt, W.E., Haines, A.J. (2002). The global moment rate distribution within plate boundary zones. In: Stein, S., Freymueller, J.T. (Eds.), Plate Boundary Zones. American Geophysical Union, Geodynamic Series, Washington, D.C, pp. 173–202.

La Rocca, M., Galluzzo, D., Saccorotti, G., Tinti, S., Cimini, G.B., Del Pezzo, E. (2004). Seismic signals associated with landslides and with a tsunami at Stromboli volcano, Italy. *Bull. Seismol. Soc. Am.* **94**, 1850–1867.

Lander, J.F. (1996). Tsunamis affecting Alaska 1737-1996, NGDC Key to Geophysical Records Documentation, 195 pp, U.S. Department of Commerce, National Oceanic and Atmospheric Administration, Boulder, Colorado.

Lavallée, D., Archuleta, R.J. (2003). Stochastic modeling of slip spatial complexities for the 1979 Imperial Valley, California, earthquake. *Geophys. Res. Lett.* **30**, doi:10.1029/2002GL015839.

Lavallée, D., Liu, P., Archuleta, R.J. (2006). Stochastic model of heterogeneity in earthquake slip spatial distributions. *Geophys. J. Int.* **165**, 622–640.

Lay, T., Wallace, T.C. (1995). Modern Global Seismology. Academic Press, San Diego, 517 pp.

Leblond, P.H., Mysak, L.A. (1978). Waves in the Ocean. Elsevier, Amsterdam, 602 pp.

Linker, M.F., Dieterich, J.H. (1992). Effects of variable normal stress on rock friction: Observations and constitutive equations. *J. Geophys. Res.* **97**, 4923–4940.

Liu, P.L.-F., Synolakis, C.E., Yeh, H. (1991). Report on the international workshop on long-wave run-up. *J. Fluid Mech.* **229**, 675–688.

Liu, P.L.-F. (2008). Tsunami modeling — propagation. In: Robinson, A.R., Bernard, E.N. (Eds.), The Sea. Harvard University Press, Cambridge, Massachusetts.

Liu, P.L.F., Yeh, H., Lin, P., Chang, K.T., Cho, Y.S. (1998). Generation and evolution of edge-wave packets. *Phys. Fluids* **10**, 1635–1657.

Liu-Zeng, J., Heaton, T.H., DiCaprio, C. (2005). The effect of slip variability on earthquake slip-length scaling. *Geophys. J. Int.* **162**, 841–849.

Locat, J. (1997). Normalized rheological behavior of fine mud and their flow properties in a pseudoplastic regime, in Debirs-Flow Hazards, mitigation, Mechanics, prediction, and Assessment, edited, pp. 260-269, Water Resources Engineering Division, American Society of Civil Engineers, New York.

Locat, J., Lee, H.J. (2002). Submarine landslides: Advances and challenges. *Canad. Geotech. J.* **39**, 193–212.

Longuet-Higgins, M.S. (1952). On the statistical distribution of the heights of sea waves. *J. Marine Res.* **11**, 245–266.

Lynett, P., Liu, P.L.F. (2002). A numerical study of submarine-landslide-generated waves and run-up. *Proc. R. Soc. Lond. A* **458**, 2885–2910.

Lynett, P. (2008). Modeling of tsunami inundation. In: Lee, W.H.K. (Ed.), Encyclopedia of Complexity and System Science. Springer-Verlag.

Lynett, P.J., Wu, T.-R., Liu, P.L.-F. (2002). Modeling wave runup with depth-integrated equations. *Coastal Eng.* **46**, 89–107.

Lynett, P.J., Liu, P.L.-F. (2005). A numerical study of run-up generated by three-dimensional landslides. *J. Geophys. Res.* **10**, doi:10.1029/2004JC002443.

Ma, K.-F., Satake, K., Kanamori, H. (1991). The origin of the tsunami excited by the 1989 Loma Prieta earthquake-faulting or slumping. *Geophys. Res. Lett.* **18**, 637–640.

Ma, X.Q., Kusznir, N.J. (1994). Effects of rigidity layering, gravity and stress relaxation on 2-D subsurface fault displacement fields. *Geophys. J. Int.* **118**, 201–220.

Madsen, P.A., Schäffer, H.A. (1998). Higher-order Boussinesq-type equations for surface gravity waves: Derivation and analysis. *Phil. Trans. R. Soc. London, A* **356**, 3123–3184.

Madsen, P.A., Fuhrman, D.R., Schäffer, H.A. (2008). On the solitary wave paradigm for tsunamis. *J. Geophys. Res.* **113**, doi:10.1029/2008JC004932.

Mai, P.M., Beroza, G.C. (2002). A spatial random field model to characterize complexity in earthquake slip. *J. Geophys. Res.* **107**, doi:10.1029/2001JB000588.

Martel, S.J. (2004). Mechanics of landslide initiation as a shear fracture phenomenon. *Mar. Geol.* **203**, 319–339.

Massel, S.R. (1996). Ocean Surface Waves: Their Physics and Prediction. World Scientific, Singapore, 508 pp.

Masterlark, T., DeMets, C., Wang, H.F., Sánchez, O., Stock, J. (2001). Homogeneous vs heterogeneous subduction zone models: Coseismic and postseismic deformation. *Geophys. Res. Lett.* **28**, 4047–4050.

Masterlark, T. (2003). Finite element model predictions of static deformation from dislocation sources in a subduction zone: Sensitivities to homogeneous, isotropic, Poisson-solid, and half-space assumptions. *J. Geophys. Res.* **103**, doi:10.1029/2002JB002296.

McCaffrey, R. (1994). Dependence of earthquake size distributions on convergence rates at subduction zones. *Geophys. Res. Lett.* **21**, 2327–2330.

Mei, C.C. (1989). The Applied Dynamics of Ocean Surface Waves. World Scientific, Singapore, 740 pp.

Meltzner, A., Sieh, K., Abrams, M., Agnew, D.C., Hudnut, K.W., Avouac, J.P., Natawidjaja, D. (2006). Uplift and subsidence associated with the Great Aceh-Andaman earthquake of 2004. *J. Geophys. Res.* **111**, doi:10.1029/2005JB003891.

Mendoza, C., Fukuyama, E. (1996). The July 12, 1993, Hokkaido-Nansei-Oki, Japan, earthquake: Coseismic slip pattern from strong-motion and teleseismic recordings. *J. Geophys. Res.* **101**, 791–801.

Michael, A.J., Geller, R.J. (1984). Linear moment tensor inversion for shallow thrust earthquakes combining first-motion and surface wave data. *J. Geophys. Res.* **89**, 1889–1897.

Mikada, H., Mitsuzawa, K., Matsumoto, H., Watanabe, K., Morita, S., Otsuka, R., Sugioka, H., Baba, T., Araki, E., Suyehiro, K. (2006). New discoveries in dynamics of an M8 earthquake-phenomena and their implications from the 2003 Tokachi–Oki earthquake using a long term monitoring cabled observatory. *Tectonophys.* **426**, 95–105.

Miller, G.R., Munk, W.H., Snodgrass, F.E. (1962). Long-period waves over California's continental borderland Part II. Tsunamis. *J. Marine Res.* **20**, 31–41.

Miyazaki, S., Larson, K.M., Choi, K., Hikima, K., Koketsu, K., Bodin, P., Haase, J., Emore, G., Yamagiwa, A. (2004). Modeling the rupture process of the 2003 September 25 Tokachi–Oki (Hokkaido) earthquake using 1-Hz GPS data. *Geophys. Res. Lett.* **31**, doi:10.1029/2004GL021457.

Mofjeld, H.O., González, F.I., Bernard, E.N., Newman, J.C. (2000a). Forecasting the heights of later waves in Pacific-wide tsunamis. *Nat. Haz.* **22**, 71–89.

Mofjeld, H.O., Titov, V.V., González, F.I., Newman, J.C. (2000b). Analytic theory of tsunami wave scattering in the open ocean with application to the North Pacific Ocean, NOAA Technical Memorandum OAR PMEL-116, 38 pp.

Mofjeld, H.O., Titov, V.V., González, F.I., Newman, J.C. (2001). Tsunami scattering provinces in the Pacific Ocean. *Geophys. Res. Lett.* **28**, 335–337.

Mofjeld, H.O., Symons, C.M., Lonsdale, P., González, F.I., Titov, V.V. (2004). Tsunami scattering and earthquake faults in the deep Pacific Ocean. *Oceanography* **17**, 38–46.

Mofjeld, H.O. (2009). Tsunami measurements. In: Bernard, E.N., Robinson, A.R. (Eds.), The Sea. Harvard University Press, Cambridge, MA, pp. 201–235.

Moore, G.F., Bangs, N.L., Taira, A., Kuramoto, S., Pangborn, E., Tobin, H.J. (2007). Three-dimensional splay fault geometry and implications for tsunami generation. *Science* **318**, 1128–1131.

Munk, W., Snodgrass, F.E., Gilbert, F. (1964). Long waves on the continental shelf: An experiment to separate trapped and leaky modes. *J. Fluid Mech.* **20**, 529–554.

Muraleedharan, G., Rao, A.D., Kurup, P.G., Nair, N.U., Sinha, M. (2007). Modified Weibull distribution for maximum and significant wave height simulation and prediction. *Coastal Eng.* **54**, 630–638.

Mysak, L.A. (1978). Wave propagation in random media, with oceanic applications. *Rev. Geophys. Space Phys.* **16**, 233–261.

Nettles, M. (2007). Analysis of the 10 February 2006: Gulf of Mexico earthquake from global and regional seismic data, paper presented at 2007 Offshore Technology Conference, Houston, Texas, p. 2.

Nielsen, S.B., Carlson, J.M. (2000). Rupture pulse characterization: Self-healing, self-similar, expanding solutions in a continuum model of fault dynamics. *Bull. Seismol. Soc. Am.* **90**, 1480–1497.

Nishigami, K. (1991). A new inversion method of coda waveforms to determine spatial distribution of coda scatterers in the crust and uppermost mantle. *Geophys. Res. Lett.* **18**, 2225–22228.

Nishigami, K., Matsumoto, S. (2008). Imaging inhomogeneous structures in the earth by coda envelope inversion and seismic array observation. *Adv. Geophys.* **50**, 301–318.

Nosov, M.A., Kolesov, S.V. (2007). Elastic oscillations of water column in the 2003 Tokachi–Oki tsunami source: In-situ measurements and 3-D numerical modeling. *Natural Hazards and Earth System Sciences* **7**, 243–249.

Novikova, T., Wen, K.-L., Huang, B.-S. (2002). Analytical model for gravity and Rayleigh -Wave investigation in the layered ocean-Earth structure. *Bull. Seismol. Soc. Am.* **92**, 723–738.

Oglesby, D.D., Day, S.M. (2002). Stochastic fault stress: Implications for fault dynamics and ground motion. *Bull. Seismol. Soc. Am.* **92**, 3006–3021.

Ohmachi, T., Tsukiyama, H., Matsumoto, H. (2001). Simulation of tsunami induced by dynamic displacement of seabed due to seismic faulting. *Bull. Seismol. Soc. Am.* **91**, 1898–1909.

Okal, E.A. (1988). Seismic parameters controlling far-field tsunami amplitudes: A review. *Nat. Haz.* **1**, 67–96.

Okal, E.A. (2003). Normal mode energetics for far-field tsunamis generated by dislocations and landslides. *Pure Appl. Geophys.* **160**, 2189–2221.

Okal, E.A., Synolakis, C.E. (2004). Source discriminants for near-field tsunamis. *Geophys. J. Int.* **158**, 899–912.

Park, J.-O., Tsuru, T., Kodiara, S., Cummins, P.R., Kaneda, Y. (2002). Splay fault branching along the Nankai subduction zone. *Science* **297**, 1157–1160.

Pelinovsky, E.N., Mazova, R.K. (1992). Exact analytical solutions of nonlinear problems of tsunami wave run-up on slopes with different profiles. *Nat. Haz.* **6**, 227–249.

Petley, D.N., Higuchi, T., Petley, D.J., Bulmer, M.H., Carey, J. (2005). Development of progressive landslide failure in cohesive materials. *Geology* **33**, 201–204.

Piatanesi, A., Lorito, S. (2007). Rupture process of the 2004 Sumatra–Andaman earthquake from tsunami waveform inversion. *Bull. Seismol. Soc. Am.* **97**, S223–S231.

Piper, D.J.W., Cochonat, P., Morrison, M.L. (1999). The sequence of events around the epicentre of the 1929 Grand Banks earthquake: Initiation of debris flows and turbidity current inferred from sidescan sonar. *Sedimentology* **46**, 79–97.

Polet, J., Kanamori, H. (2000). Shallow subduction zone earthquakes and their tsunamigenic potential. *Geophys. J. Int.* **142**, 684–702.

Polet, J., Thio, H.K. (2003). The 1994 Java tsunami earthquake and its "normal" aftershocks. *Geophys. Res. Lett.* **30**, doi:10.1029/2002GL016806.

Poliakov, A.N.B., Dmowska, R., Rice, J.R. (2002). Dynamic shear rupture interactions with fault bends and off-axis secondary faulting. *J. Geophys. Res.* **107**, doi:10.1029/2001JB000572.

Pollitz, F.F., Banerjee, P., Grijalva, K., Nagarajan, B., Bürgmann, R. (2008). Effect of 3-D viscoelastic structure on post-seismic relaxation from the 2004 M = 9.2 Sumatra earthquake. *Geophys. J. Int.* **173**, 189–204.

Power, W.L., Tullis, T.E. (1991). Euclidean and fractal models for the description of rock surface roughness. *J. Geophys. Res.* **96**, 415–424.

Prevosto, M., Kogstad, H.E., Robin, A. (2000). Probability distributions for maximum wave and crest heights. *Coastal Eng.* **40**, 329–360.

Rabinovich, A.B. (1997). Spectral analysis of tsunami waves: Separation of source and topography effects. *J. Geophys. Res.* **102**, 12,663–612,676.

Rabinovich, A.B., Stephenson, F.E., Thomson, R.E. (2006). The California tsunami of 15 June 2005 along the coast of North America. *Atmosphere-Ocean* **44**, 415–427.

Rabinovich, A.B., Thomson, R.E. (2007). The 26 December 2004 Sumatra tsunami: Analysis of tide gauge data from the world ocean Part 1. Indian Ocean and South Africa. *Pure Appl. Geophys.* **164**, 261–308.

Rayleigh, J.W.S. (1880). On the resultant of a large number of vibrations of the same pitch and of arbitrary phase. *Phil. Mag.* **10**, 73–78.

Rhie, J., Dreger, D.S., Bürgmann, R., Romanowicz, B. (2007). Slip of the 2004 Sumatra–Andaman earthquake from joint inversion of long-period global seismic waveforms and GPS static offsets. *Bull. Seismol. Soc. Am.* **97**, S115–S127.

Rice, J.R. (1983). Constitutive relations for fault slip and earthquake instabilities. *Pure Appl. Geophys.* **121**, 443–475.

Rice, J.R., Cocco, M. (2007). Seismic fault rheology and earthquake dynamics. In: Handy, M.R., et al. (Eds.), Tectonic Faults: Agents of Change on a Dynamic Earth. MIT Press, Cambridge, MA, pp. 99–137.

Rudnicki, J.W., Wu, M. (1995). Mechanics of dip-slip faulting in an elastic half-space. *J. Geophys. Res.* **22**, 173–22186.

Ruff, L., Kanamori, H. (1983). Seismic coupling and uncoupling at subduction zones. *Tectonophys.* **99**, 99–117.

Ruina, A.L. (1983). Slip instability and state variable friction laws. *J. Geophys. Res.* **88**, 10,359–310,370.

Rybicki, R. (1986). Dislocations and their geophysical application. In: Teisseyre, R. (Ed.), Continuum Theories in Solid Earth Physics. Elsevier, Amsterdam, pp. 18–186.

Rychlik, I., Johannesson, P., Leadbetter, M.R. (1997). Modelling and statistical analysis of ocean-wave data using transformed Gaussian processes. *Marine Struct.* **10**, 13–47.

Rychlik, I., Leadbetter, M.R. (1997). Analysis of ocean waves by crossing and oscillation intensities, paper presented at Proceedings of the Seventh International Offshore and Polar Engineering Conference (ISOPE), Golden, Colorado, pp. 206–213.

Sagiya, T., Thatcher, W. (1999). Coseismic slip resolution along a plate boundary megathrust: the Nankai Trough, southwest Japan. *J. Geophys. Res.* **104**, 1111–1129.

Saito, T., Furumura, T. (2009a). Scattering of linear long-wave tsunamis due to randomly fluctuating sea-bottom topography: Coda excitation and scattering attenuation. *Geophys. J. Int.* **177**, 958–965.

Saito, T., Furumura, T. (2009b). Three-dimensional tsunami generation simulation due to sea-bottom deformation and its interpretation based on linear theory. *Geophys. J. Int.* **178**, 877–888.

Saito, T., Furumura, T. (2009c). Three-dimensional simulation of tsunami generation and propagation: Application to intraplate events. *J. Geophys. Res.* **114**, doi:10.1029/2007JB005523.

Samorodnitsky, G., Taqqu, M.S. (1994). Stable Non-Gaussian Random Processes: Stochastic Models with Infinite Variance. Chapman & Hall/CRC Press, Boca Raton, Florida, 632 pp.

Satake, K., Tanioka, Y. (1999). Sources of tsunami and tsunamigenic earthquakes in subduction zones. *Pure Appl. Geophys.* **154**, 467–483.

Sato, K., Minagawa, N., Hyodo, M., Baba, T., Hori, T., Kaneda, Y. (2007). Effect of elastic inhomogeneity on the surface displacements in the northeastern Japan: Based on three-dimensional numerical modeling. *Earth Planets Space* **59**, 1083–1093.

Savage, J.C. (1998). Displacement field for an edge dislocation in a layered half-space. *J. Geophys. Res.* **103**, 2439–2446.

Scholz, C.H. (1998). Earthquakes and friction laws. *Nature* **391**, 37–42.

Seno, T. (2002). Tsunami earthquakes as transient phenomena. *Geophys. Res. Lett.* **29**, doi:10.1029/2002GL014868.

Seno, T., Hirata, K. (2007). Is the 2004 Sumatra–Andaman earthquake a tsunami earthquake? *Bull. Seismol. Soc. Am.* **97**, S296–S306.

Shapiro, S.S., Wilk, M.B. (1965). An analysis of variance test for normality (complete samples). *Biometrika* **52**, 591–611.

Shuto, N., Chida, K., Imamura, F. (1995). Generation mechanism of the first wave of the 1983 Nihonkai–Chubu earthquake tsunamis. In: Tsuchiya, Y., Shuto, N. (Eds.), Tsunami: Progress in Prediction, Disaster Prevention and Warning. Kluwer Academic Publishers, Dordrecht, pp. 37–53.

Shuto, N., Matsutomi, H. (1995). Field survey of the 1993 Hokkaido Nansei-Oki earthquake tsunami. *Pure Appl. Geophys.* **144**, 649–663.

Sibuet, J.-C., Rangin, C., Le Pichon, X., Singh, S., Cattaneo, A., Graindorge, D., Klingelhoefer, F., Lin, J.-Y., Malod, J., Maury, T., Schneider, J.-L., Sultan, N., Umber, M., Yamaguchi, H., Sumatra Aftershocks Team (2007). 26th December 2004 great Sumatra–Andaman earthquake: Co-seismic and post-seismic motions in northern Sumatra. *Earth Planet. Sci. Lett.* **263**, 88–103.

Singh, S.J., Punia, M., Rani, S. (1994). Crustal deformation due to non-uniform slip along a long fault. *Geophys. J. Int.* **118**, 411–427.

Snodgrass, F.E., Munk, W.H., Miller, G.R. (1962). Long-period waves over California's continental borderland Part I. Background spectra. *J. Marine Res.* **20**, 3–30.

Somerville, P., Irikura, K., Graves, R., Sawada, S., Wald, D., Abrahamson, N.A., Iwasaki, Y., Kagawa, T., Smith, N., Kowada, A. (1999). Characterizing crustal earthquake slip models for the prediction of strong ground motion. *Seismol. Res. Lett.* **70**, 59–80.

Stephens, M.A. (1974). EDF statistics for goodness of fit and some comparisons. *J. Amer. Statist. Assoc.* **69**, 730–737.

Stoker, J.J. (1957). Water Waves: The Mathematical Theory with Applications. Interscience Publishers, Inc., New York, 567 pp.

Subarya, C., Chlieh, M., Prawirodirdjo, L., Avouac, J.P., Bock, Y., Sieh, K., Meltzner, A., Natawidjaja, D., McCaffrey, R. (2006). Plate-boundary deformation associated with the great Sumatra–Andaman earthquake. *Nature* **440**, 46–51.

Synolakis, C.E. (1987). The runup of solitary waves. *J. Fluid Mech.* **185**, 523–545.

Tadepalli, S., Synolakis, C.E. (1994). The run-up of N-waves on sloping beaches. *Proc. R. Soc. Lond. A* **445**, 99–112.

Takahara, M., Yomogida, K. (1992). Estimation of Coda Q using the maximum likelihood method. *Pure Appl. Geophys.* **139**, 255–268.

Tanioka, Y., Ruff, L., Satake, K. (1995). The great Kuril earthquake of October 4, 1994 tore the slab. *Geophys. Res. Lett.* **22**, 1661–1664.

Tanioka, Y., Ruff, L.J., Satake, K. (1997). What controls the lateral variation of large earthquake occurrence along the Japan trench? *The Island Arc* **6**, 261–266.

Tanioka, Y., Nishimura, Y., Hirakawa, K., Imamura, F., Abe, I., Abe, Y., Shindou, K., Matsutomi, H., Takahashi, T., Imai, K., Harada, K., Namegawa, Y., Hasegawa, Y., Hayashi, Y., Nanayama, F., Kamataki, T., Kawata, Y., Fukasawa, Y., Koshimura, S., Hada, Y., Azumai, Y., Hirata, K., Kamikawa, A., Yoshikawa, A., Shiga, T., Kobayashi, M., Masakam, S. (2004). Tsunami run-up heights of the 2003 Tokachi–Oki earthquake. *Earth Planets Space* **56**, 359–365.

Taylor, M.A.J. (1998). Chapter VI, Friction, dilatancy, and pore fluids in controlling subduction earthquake rupture. PhD Thesis. Harvard University Cambridge, MA, 41 pp.

Taylor, M.A.J., Dmowska, R., Rice, J.R. (1998). Upper plate stressing and seismicity in the subduction earthquake cycle. *J. Geophys. Res.* **103**, 24,523–524,542.

Templeton, E.L., Baudet, A., Bhat, H.S., Dmowska, R., Rice, J.R., Rosakis, A.J., Rousseau, C.-E. (2009). Finite element simulations of dynamic shear rupture experiments and dynamic path selection along kinked and branched faults. *J. Geophys. Res.* **114**, doi:10.1029/2008JB006174.

The WAFO Group, (2000). WAFO: A Matlab Toolbox for Analysis of Random Waves and Loads, Tutorial Version 2.0.02. Lund Institute of Technology, Lund University, Lund, Sweden. 124 pp.

Thio, H.K., Graves, R.W., Somerville, P.G., Sato, T., Ishii, T. (2004). A multiple time window rupture model for the 1999 Chi–Chi earthquake from a combined inversion of teleseismic, surface wave, strong motion, and GPS data. *J. Geophys. Res.* **109**, doi:10.1029/2002JB002381.

Tinti, S., Tonini, R. (2005). Analytical evolution of tsunamis induced by near-shore earthquakes on a constant-slope ocean. *J. Fluid Mech.* **535**, 33–64.

Trifunac, M.D., Hayir, A., Todorovska, M.I. (2002). Was Grand Banks event of 1929 a slump spreading in two directions? *Soil Dynam. Earthquake Eng.* **22**, 349–360.

Tsai, C.P. (1997a). Slip, stress drop and ground motion of earthquakes: A view from the perspective of fractional Brownian motion. *Pure Appl. Geophys.* **149**, 689–706.

Tsai, C.P. (1997b). Ground motion modeling for seismic hazard analysis in the near-source regime: An asperity model. *Pure Appl. Geophys.* **149**, 265–297.

Tsai, V.C., Nettles, M., Ekström, G., Dziewonski, A.M. (2005). Multiple CMT source analysis of the 2004 Sumatra earthquake. *Geophys. Res. Lett.* **32**, doi:10.1029/2005GL023813.

Ursell, F. (1952). Edge waves on a sloping beach. *Proc. R. Soc. Lond. A* **214**, 79–97.

van Dorn, W.G. (1984). Some tsunami characteristic deducible from tide records. *J. Phys. Oceanogr.* **14**, 353–363.

van Dorn, W.G. (1987). Tide gage response to tsunamis. Part II: Other oceans and smaller seas. *J. Phys. Oceanogr.* **17**, 1507–1517.

Varnes, D.J. (1978). Slope movement types and processes. In: Schuster, R.L., Krizek, R.J. (Eds.), Landslides: Analysis and Control. National Academy of Sciences, Washington, D.C, pp. 11–33.

Ward, S.N. (1982). On tsunami nucleation II. An instantaneous modulated line source. *Phys. Earth Planet. Int.* **27**, 273–285.

Watanabe, H. (1972). Statistical studies on the wave-form and maximum height of large tsunamis. *J. Oceanogr. Soc. Japan* **28**, 229–241.

Wells, D.L., Coppersmith, K.J. (1994). New empirical relationships among magnitude, rupture length, rupture width, rupture area, and surface displacement. *Bull. Seismol. Soc. Am.* **84**, 974–1002.

Wendt, J., Oglesby, D.D., Geist, E.L. (2009). Tsunamis and splay fault dynamics. *Geophys. Res. Lett.*, doi:10.1029/2009GL038295.

Wessel, P., Smith, W.H.F. (1995). New version of the Generic Mapping Tools released. *Eos, Trans. Am. Geophys. U.* **76**, F329.

Wu, T.Y. (1981). Long waves in ocean and coastal waters. *J. Eng. Mech. Division, ASCE* **107**, 501–522.

Yagi, Y. (2004). Source rupture process of the 2003 Tokachi–Oki earthquake determined by joint inversion of teleseismic body wave and strong ground motion data. *Earth Planets Space* **56**, 311–316.

Yamanaka, Y., Kikuchi, M. (2003). Source process of the recurrent Tokachi–Oki earthquake on September 26, 2003 inferred from teleseismic body waves. *Earth Planets Space* **55**, e21–e24.

Yeh, H. (2008). Tsunami impacts on coastlines. In: Robinson, A.R., Bernard, E.N. (Eds.), The Sea. Harvard University Press, Cambridge, Massachusetts, pp. 333–369.

Yeh, H.H. (1991). Tsunami bore runup. *Nat. Haz.* **4**, 209–220.

Yoshioka, S., Hashimoto, M., Hirahara, K. (1989). Displacement fields due to the 1946 Nankaido earthquake in a laterally inhomogeneous structure with the subducting Philippine Sea plate–a three-dimensional finite element approach. *Tectonophys.* **159**, 121–136.

Zhao, S., Müller, R.D., Takahashi, Y., Kaneda, Y. (2004). 3-D finite-element modeling of deformation and stress associated with faulting: Effect of inhomogeneous crustal structures. *Geophys. J. Int.* **157**, 629–644.

Zheng, G., Rice, J.R. (1998). Conditions under which velocity-weakening friction allows a self-healing versus a cracklike mode of rupture. *Bull. Seismol. Soc. Am.* **88**, 1466–1483.